universität wien

DISSERTATION | DOCTORAL THESIS

Titel | Title

Low-energy ion irradiation on 2D materials – from single defects to few-atom noble gas clusters

verfasst von | submitted by

Manuel Längle BSc MSc

angestrebter akademischer Grad | in partial fulfilment of the requirements for the degree of

Doktor der Naturwissenschaften (Dr.rer.nat.)

Wien | Vienna, 2024

Studienkennzahl lt. Studienblatt | Degree programme code as it appears on the student record sheet:	UA 796 605 411
Dissertationsgebiet lt. Studienblatt | Field of study as it appears on the student record sheet:	Physik
Betreut von | Supervisor:	Univ.-Prof. Dr. Jani Kotakoski

Abstract

Two-dimensional (2D) materials, and especially their two prominent members graphene and monolayer hexagonal boron nitride (hBN), have generated significant research interest over the better part of the last two decades. Graphene is an extraordinary electrical conductor while it is also extremely strong, impermeable to gases and, as a monolayer, it can be used as a substrate for cluster growth or single implanted atoms, while, as a multilayer, it can be used to encapsulate different trapped atoms or molecules. hBN on the other hand is a wide gap insulator which is often used as a dielectric. However, point defects in hBN were discovered to be very promising quantum emitters.

Here, graphene and hBN are exposed to low-energy single-charged ion irradiation in order to create defects and trap the impinging ions. The irradiation effects are studied using atomic resolution scanning transmission electron microscopy (STEM) and electron energy loss spectroscopy (EELS). It is found that the irradiation leads to the creation of point defects in hBN. Similarly created and characterized defects in graphene were used as anchoring points for individual atoms and clusters of iron, which was introduced via physical vapour deposition. For multi-layered samples ion irradiation was used for introducing noble gas atoms between the layers resulting in room-temperature stable 2D van der Waals crystals. The trapped atoms arrange as expected from non-directional van der Waals bonding for small clusters. We observe movement and structural changes in the clusters as well as phase transitions during imaging.

Studying defect creation in hBN and correlating these with emission spectra opens the path towards tailoring hBN for quantum applications. The ability to anchor individual atoms covalently in the graphene membrane provides the possibility to create single atom catalysts. The so far unexplored frontier of encapsulated two-dimensional van der Waals solids is opened up by the possibility of noble gas trapping. This makes it now, decades after van der Waals atomic solids of noble gases on cold metal surfaces were the first experimental examples of 2D systems, possible to study the atomic arrangement of this simple condensed matter system.

Overall, it was shown that 2D materials can be tailored at the atomic scale which brings us one step closer to 2D material quantum emitters and single atom catalysts. At the same time the 2D van der Waals noble gas crystals provide a simple condensed matter system for fundamental studies of statistical physics.

Zusammenfassung

Zweidimensionale (2D) Materialien, insbesondere Graphen und einlagiges hexagonales Bornitrid (hBN), wurden in den letzten zwei Jahrzehnten intensiv untersucht. Graphen ist ein hervorragender elektrischer Leiter und undurchlässig für Gase. Als Monolage kann es als Substrat für das Wachstum von Clustern oder einzelnen implantierten Atomen verwendet werden, während es mit mehreren Lagen zum Einfangen verschiedener Atome oder Moleküle dienen kann. hBN ist ein Isolator mit großer Bandlücke, der häufig als Dielektrikum verwendet wird. Punktdefekte in hBN sind jedoch auch vielversprechende Quantenemitter.

In dieser Arbeit werden Graphen und hBN niederenergetischer Bestrahlung aus einfach geladenen Ionen ausgesetzt, um Defekte zu erzeugen und die Ionen einzufangen. Die Auswirkungen der Bestrahlung werden mit Hilfe von atomar auflösender Rastertransmissionselektronenmikroskopie und Elektronenenergieverlustspektroskopie untersucht. In hBN führt die Bestrahlung zur Bildung von Punktdefekten. Ähnlich erzeugte und charakterisierte Defekte in Graphen werden verwendet, um extra aufgebrachtes Eisen entweder als einzelne Atome oder als Cluster zu verankern. Bei mehrschichtigen Proben werden durch Ionenbestrahlung Edelgasatome zwischen die Schichten eingebracht, was zu stabilen zweidimensionalen van der Waals Kristallen bei Raumtemperatur führt. Die eingefangenen Atome ordnen sich so an, wie man es aufgrund der ungerichteten van der Waals Bindung erwarten würde. Die Cluster ändern ihre Struktur, bewegen sich und Phasenübergänge sind während der Messungen sichtbar.

Die Untersuchung der Entstehung von Defekten in hBN und deren Korrelation mit Emissionsspektren öffnet den Weg zur gezielten Manipulation von hBN für Quantenanwendungen. Die Fähigkeit, einzelne Atome kovalent in der Graphenmembran zu verankern, bietet die Möglichkeit, Einzelatomkatalysatoren zu schaffen. Die Möglichkeit Edelgase einzufangen, eröffnet das bisher unerforschte Gebiet der eingeschlossenen zweidimensionalen van der Waals Festkörper. Die ersten experimentellen Beispiele für 2D-Systeme waren van der Waals Festkörper aus Edelgasen auf kalten Metalloberflächen. Jahrzehnte später ist es nun möglich, die atomare Anordnung dieses einfachen Systems direkt zu untersuchen.

Insgesamt konnte gezeigt werden, dass 2D-Materialien atomar manipuliert werden können, was uns einen Schritt näher an Quantenemitter und Einzelatomkatalysatoren in 2D-Materialien bringt. Zugleich bieten die zweidimensionalen van der Waals Feskörper bestehend aus Edelgas Atomen ein einfaches System für grundlegende Untersuchungen der statistischen Physik.

Contents

Acknowledgements

None of this work would have been possible without continuous support from various people, so I would like to take some time to thank them.

First of all I would like to thank my supervisor, Jani. I started working with him in 2016 for my Bachelor thesis and seven years later I am finishing my Dissertation. I am truly grateful for the opportunities he provided for me throughout my studies. On top of being able to work on an exciting project with excellent instrumentation I was able to teach various subject, go on secondments in different groups, present at numerous conferences and always had the support I needed. He guided me trough the entire journey such that I did not loose track of what is important while still being able to choose my own path. I am truly grateful.

Clemens is always an immense help when conducting experiemnts. Whether it is microscopy or developing different instrumentation, he always offers a helping hand and is eager to teach everyone around him. Without him many of the here presented results would not have been possible and the time at Sternwarte would not have been as enjoyable as it was.

I had the pleasure of working with Harriet, Kimmo and Jacob on various projects. They taught me a lot and it was inspiring to work with them. Also thanks to Toma, Alexander, Viera and Vladimir for the valuable and thought provoking scientific discussions. All of them are truly great scientists and I hope I can keep working with them in the future.

We are all trained by the people before us and thus I want to thank people who were PhD students at the time I joined the group. Thanks to Heena, Alexandru, Andreas and especially to Georg, Gregor and Alberto for all of their practical knowledge but also for being friends and companions along the way.

I had the pleasure of sharing my office with a lot of colleagues in the last years, however, I really have to thank Clara, Carsten, Wael, David and Barbara for the nice time and emotional support throughout the process. Thanks to you the office was always a very nice place to work at where we could be concentrated or relaxed, depending on what was necessary. We supported each other, we learned from each other and we made fun of each other when appropriate. It is great to have all of you as my colleagues and friends.

I had the pleasure of (co)mentoring Barbara, Vinzent, Fabian, Nika, Daniel, Luis and Gilda. In the process I gained valuable experiences and learned from all of them. I am sorry that at the time

I did not know what I know now or else all of your projects would have probably gone much smoother.

Of course I also want to thank Umair, Somar, Nandhini, Diana, Marius, Morris, Thuy An, Eugen and all the other group members I might have forgotten to mention explicitly here. You all were part of my journey and made it very enjoyable.

For my stays in Helsinki and Berlin I want to thank Kenza and Benedikt who both took care of me and contributed to making these experiences as valuable as they were. I wish both of them all the best and look forward to learning from them in the future.

Special thanks goes to Helena and Kathrin as well as to Christiane and Julia for their continuous support with all the organisational issues that arose along the way and for all the nice chats we had in the last years.

I had the honour of teaching various courses at the University of Vienna. Thanks to all the students who actively participated and challenged my knowledge in these courses. I enjoyed it very much and I feel like at least some of them did too.

In the last 3.5 years I had the great honour of serving as a vice student speaker for the Vienna Doctorate School of Physics and vice speaker of the Student Union of all PhD students in Natural Sciences. During that time I worked together with Clara, Margaret, Clara and many more. Thank you for your clever thoughts and energy for all the projects that we realized.

Also I want to explicitly thank all those devices that worked reliably during the last years for doing exactly that.

Lastly, but very importantly I would like to thank my family, my friends, my flatmates, my Jugger club, people from Roter Vektor and especially Romana for keeping me (mostly) sane during the last years. You made sure I took the breaks I needed and that they were as enjoyable as they were.

And last I want to thank myself for pulling through and actually finishing this thesis.

Presented publications

1. **Manuel Längle**, Kenichiro Mizohata, Clemens Mangler, Alberto Trentino, Kimmo Mustonen, E. Harriet Åhlgren, Jani Kotakoski
   Two-dimensional few-atom noble gas clusters in a graphene sandwich. Nature Materials (2024) [1].

   Contributed by designing the experiments, preparing the samples, carrying out ion irradiation, carrying out microscopy, analysing the data, plotting the figures and writing the first draft of the manuscript.

2. **Manuel Längle**, Barbara Maria Mayer, Jacob Madsen, Arixin Bo, Clara Kofler, Vinzent Hana, Clemens Mangler, Toma Susi, and Jani Kotakoski
   Defect-engineering of hexagonal boron nitride via low-energy plasma irradiation. In preparation [2].

   Contributed by designing the experiments, characterizing the plasma source, carrying out plasma irradiation, carrying out microscopy, analysing the data, plotting the figures and writing the first draft of the manuscript.

3. Alberto Trentino, Georg Zagler, **Manuel Längle**, Jacob Madsen, Toma Susi, Clemens Mangler, E. Harriet Åhlgren, Kimmo Mustonen, Jani Kotakoski
   Single atoms and metal nanoclusters anchored to graphene via vacancies. Submitted for publication [3].

   Contributed by characterizing the plasma source, carrying out plasma irradiation, microscopy and physical vapour deposition for Fe. Participated in writing the manuscript.

List of acronyms

2D two-dimensional

3D three-dimensional

ADF annular dark field

AFM atomic force microscopy

BF bright field

CANVAS system for controlled alteration of nanomaterials in vacuum down to the atomic scale

CCD charge-coupled device

CFEG cold field emission gun

CVD chemical vapour deposition

DFT density functional theory

EBID electron-beam-induced deposition

ECR electron cyclotron resonance

EDX energy dispersive x-ray spectroscopy

EEL electron energy loss

EELS electron energy loss spectroscopy

FFT fast Fourier transformation

FLG few-layer graphene

FOV field of view

FWHM full width half maximum

HAADF high-angle annular dark field

HOPG highly-ordered pyrolytic graphite

IPA isopropyl alcohol

MAADF medium-angle annular dark field

MD molecular dynamics

MLE monolayer equivalent

MPS microwave plasma source

PMMA polymethylmethacrylat

PVD physical vapour deposition

SE secondary electron

STEM scanning transmission electron microscopy

STM scanning tunneling microscopy

TEM transmission electron microscopy

UHV ultra-high vacuum

vdW van der Waals

VTE vacuum thermal evaporation

ZLP zero-loss peak

Chapter 1

Introduction

Our lives and societies are influenced by the materials we use to a degree that whole eras are named after them. Even though the field of two-dimensional (2D) materials is still quite young (it was triggered with the discovery of the electric field effect in graphene in 2004 [4]) it already shows promise for new technological applications [5, 6]. Due to their reduced dimensionality, 2D materials exhibit fundamentally different properties than their bulk counterparts giving rise to interesting new physical phenomena. In our research group we focus on altering the properties of known 2D materials as well as on creating and characterizing completely new ones. In this work ion irradiation is used to change the structure of graphene and hBN as well as to create trapped 2D van der Waals (vdW) noble gas structures.

Ion beams are an efficient tool to change the morphology of a material in a controllable manner. They can be used to modify electronic, mechanical, magnetic and optical properties to specific applications [7, 8]. Ion irradiation is a versatile technique as there are many controllable parameters, such as the species, the mass, the charge state, the energy (kinetic and potential) of the ion as well as its incident angle. This is especially true for conventional three-dimensional (3D) materials, where it is a powerful and well established technique. The most prominent example for the technical applicability of ion irradiation is probably the semiconductor industry, where the electronic properties of materials can be engineered to a degree that nm-sized transistors and light emitting diodes or quantum well lasers are made possible [9].

However, the effect of ion irradiation on 2D materials differs from the bulk case: In 3D the surfaces can be neglected, but 2D materials are in contrast nothing but surface. There are three key changes for 2D materials. Firstly the energy needs to be much lower, something that most existing

ion irradiation set-ups were not built for. Secondly, atomically clean and high quality suspended samples are necessary, something where existing production and cleaning protocols still need to be improved. And thirdly, experiments should be carried out under ultra-high vacuum (UHV) so that methods for defect creation and detection are combined within the same set-up to prevent recontamination of the sample surface [7]. For this purpose, the system for controlled alteration of nanomaterials in vacuum down to the atomic scale (CANVAS) [10], an interconnected UHV system, was developed by our group. It connects various methods for sample manipulation, such as low-energy ion irradiation using a plasma source, physical vapour deposition (PVD) devices and different lasers with the Nion UltraSTEM 100 microscope, an instrument used for aberration corrected scanning transmission electron microscopy (STEM) as well as electron energy loss spectroscopy (EELS), which are the main methods employed in this work.

The two main materials used in this work are graphene, a highly conductive material [4], and monolayer hBN, a material with a wide band gap [11], which are the two thinnest known materials. Defect creation in graphene through low-energy ion irradiation has previously been studied by our group [12]. We have shown that the created vacancies can be filled with different elements employing a two-step process [13, 14]. In this thesis we use Fe atoms, introduced onto the sample via PVD which highlights the general applicability of this method for different elements [3] The density of embedded atoms or clusters can be controlled through irradiation dose, and the size of the clusters through evaporation time. This is interesting as individual atoms embedded in 2D materials have been used in various fundamental studies ranging from single-defect vibrational spectroscopy [15] to mapping of electric and magnetic fields [16]. Within our group (and others), also atom manipulation using the Ångström-sized electron beam in STEM [17, 18, 19, 20] has been a major undertaking. We believe this method for creating small clusters and individual atoms can also be used for catalysis. However, not only ions can be used for creating defects. Employing an altered version of an automatic image acquisition algorithm [21], also high-energy electrons can be used to create defect patterns, similar to Refs. [22, 23]. The feasibility of this idea is illustrated using electron-beam-induced deposition (EBID).

Defect creation in hBN, in contrast to graphene, is an open but interesting topic. Defects in hBN have recently received increasing attention as a solid state host for quantum emitters [24] and other applications [25]. Lasers [26], ions [27], neutrons [28] and electrons [29, 30] have been used to create quantum emitters in hBN, however so far only in the case of electrons [31] the direct correlation between irradiation and the exact atomic structure has been established. Analytical potential molecular dynamics simulations [32, 33] have suggested that low-energy

noble gas ions should lead to the formation of point defects and that there should be similar probabilities for creating single boron and nitrogen vacancies. However, this prediction is not in line with our experimental results where we expose hBN to low-energy Ar^+ ions and use automated imaging [21] in combination with machine learning to quantify irradiation results [2], as will be discussed.

Instead of irradiating monolayers and introducing defects into graphene and hBN also few layers can be irradiated. Due to the impermeability of these materials to gases [34], Ar, Kr or Xe ions can be trapped using an energy high enough to penetrate the first layer, but low enough not to pass through the second. They neutralize and form room temperature stable vdW system of condensed noble gases. Neutral physical systems, such as inert atoms or graphene layers, behave according to the vdW interaction. Although they do not form covalent or ionic bonds, the temporal fluctuations in the distribution of their charge turns them into fluctuating dipoles, which leads to attraction between them. The energy of the resulting bond is usually in the order of 0.1 eV/atom [35, 36], which is normally too low for the bond to be stable at room temperature. Thus what drives the formation of crystallites is the encapsulation, resulting in one of the simplest conceivable solids, a 2D vdW atomic crystal. Similar structures formed by noble gas atoms on surfaces at cryogenic temperatures [37] have been experimentally studied since the 1960's and were probably the first 2D systems ever studied. However, encapsulation of similar structures within graphene covered surfaces has also made it possible to image Xe clusters at room temperature using scanning tunneling microscopy (STM) [38, 39]. The graphene encapsulation, however, complicates imaging the atomic structure of the crystallites with this method, which even lead to misidentification of such structures in the past [40, 41]. In contrast, here we have trapped Ar, Kr and Xe between two free-standing layers of graphene allowing the direct observation of the atomic structure using STEM.

Chapter 2

Materials

2.1 Graphene and hBN

Graphene and monolayer hBN are materials with similar structural, mechanical and thermal properties, but show great differences from an electronic point of view. In 2004, a monolayer of graphene was isolated and electronically characterized for the first time [4]. It is a material with outstanding properties [42], which started the entire field of 2D materials [43, 44]. Monolayer hBN, so-called "white graphene", another important member of the 2D family, was also exfoliated by the same group one year after graphene [45] and has attracted a lot of attention in recent years due to its possible application as a host for quantum emitters [25]. Both materials are thermally and mechanically robust, chemically stable and host interesting physical phenomena.

2.1.1 Structure

Graphene consists of C atoms, with the atomic number $Z = 6$, hBN consists of B and N atoms, the neighbours of C in the periodic table with atomic numbers $Z = 5$ and $Z = 7$, respectively. In covalently bound materials, such as graphene and also to a degree hBN, the hybridisation of the valence orbitals determines their structure. The electronic ground state configuration of B, C and N is given by $1s^2 2s^2 2p^x$ with $x = 1, 2, 3$, respectively. The $2s$ and $2p$ orbitals can hybridize into sp^x plus p orbitals forming covalent bonds. sp^3 carbon bonds result in the diamond structure, whereas boron and nitrogen form cubic BN [48]. sp^2 bonds form layered hexagonal structures such as graphite for C and and bulk hBN for B and N. The atomically thin sheets are held together by vdW forces, making it feasible to exfoliate them. Separated individual layers of these bulk

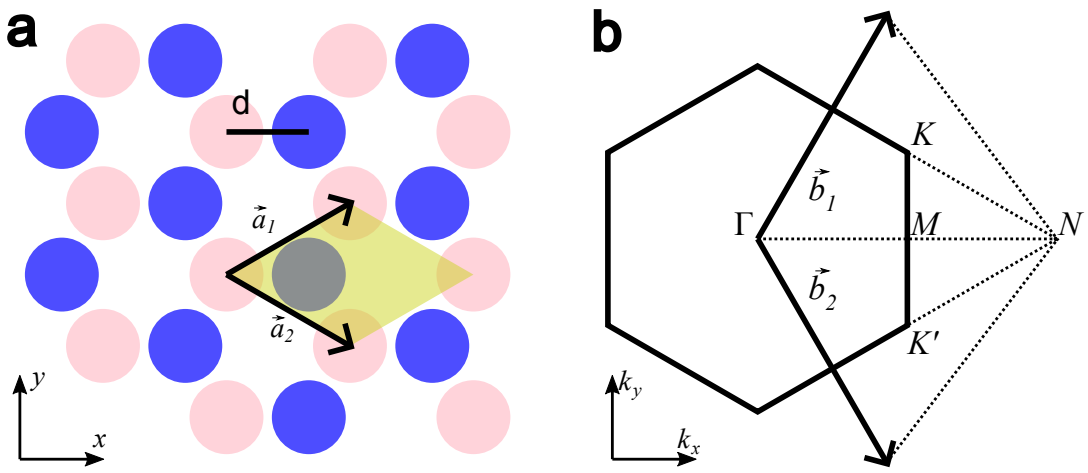

Figure 2.1: **Honeycomb lattice structure and its corresponding first Brillouin zone with high symmetry points marked.** (a) In-plane lattice structure of graphene and monolayer hBN. $\vec{a}_1$ and $\vec{a}_2$ are the lattice vectors and the unit cell is highlighted in yellow. The lattice constant $a = |\vec{a}_1| = |\vec{a}_2|$ is 2.46 Å for graphene and 2.5 Å for hBN . The bond lengths d are 1.42 Å and 1.44 Å, respectively. (b) Corresponding first Brillouin zone with the high symmetry points Γ, K, K' and M and reciprocal lattice vectors $\vec{b}_1$ and $\vec{b}_2$. Values taken from Ref. [46]. Figure reproduced from [47].

materials are called graphene and monolayer hBN. Where for graphene the bonding is almost purely covalent hBN has significant ionic contributions. Fig. 2.1 shows the 2D structure resulting from sp^2 hybridization. Every atom has three nearest neighbours with equal spacing between them, forming a honeycomb structure. The real space lattice vectors can be defined as

$$\vec{a}_1 = \sqrt{3}d\begin{pmatrix}\frac{\sqrt{3}}{2}\\ \frac{1}{2}\end{pmatrix},\ \vec{a}_2 = \sqrt{3}d\begin{pmatrix}\frac{\sqrt{3}}{2}\\ -\frac{1}{2}\end{pmatrix}, \tag{2.1}$$

which results in the reciprocal lattice vectors

$$\vec{b}_1 = \frac{2\pi}{3d}\begin{pmatrix}1\\ \sqrt{3}\end{pmatrix},\ \vec{b}_2 = \frac{2\pi}{3d}\begin{pmatrix}1\\ -\sqrt{3}\end{pmatrix}. \tag{2.2}$$

The lattice vectors are the same for hBN and graphene, however, for graphene both atoms in the base are C whereas in hBN they are B and N. The interatomic distance differs, it is

$$d_{graphene} = 1.42 \text{ Å}$$

for graphene and

$$d_{hBN} = 1.44 \text{ Å}$$

for hBN [46]. The first Brillouin zone, the Wigner-Seitz cell of the reciprocal lattice [35], is a hexagon with the four symmetry points Γ, K, K' and M shown in Fig. 2.1 b. In graphene, K and

K' are called Dirac points and play an important role in the electronic structure. Their coordinates in reciprocal space are given by

$$\vec{K} = \frac{2\pi}{3d}\begin{pmatrix} 1 \\ \frac{1}{\sqrt{3}} \end{pmatrix}, \ \vec{K'} = \frac{2\pi}{3d}\begin{pmatrix} 1 \\ -\frac{1}{\sqrt{3}} \end{pmatrix}. \tag{2.3}$$

Graphene and monolayer hBN are the thinnest possible crystals, both being only one atom thick. As in hBN the binding is slightly ionic, this results in a difference in stacking for multi layer structures. While few-layer graphene (FLG) exfoliated from graphite is usually AB stacked, in hBN boron and nitrogen atoms are stacked on top of each other resulting in AA' stacking [46]. The vdW interaction governs the distance between the sheets.

2.1.2 Properties

Mechanical properties

The strong in-plane sp^2 bonds in graphene and hBN result in the robust lattice structure responsible for the mechanical properties of graphene and hBN. The Young's modulus, a material property describing its stiffness, of graphene was measured to be 1.0 ± 0.1 TPa using nanoindentation [49] and 2.4 ± 0.4 TPa using Raman spectroscopy [50], which are both high values making graphene the strongest material ever measured. Monolayer hBN has a comparable, but lower, Young's modulus of 0.865 ± 0.073 TPa [51].

Measuring the adhesion of hBN/hBN and Gr/Gr [52] showed that the cohesion energy and the intrinsic cleavage strength of graphene and hBN are practically the same with the normal force being marginally higher for graphene and the shear force marginally higher for hBN. The normal incidence adhesion energy was 0.328 ± 0.028 Jm^{-2} for graphene and 0.326 ± 0.026 Jm^{-2} for hBN.

Thermal properties

Also their other properties, namely their remarkable chemical and thermal stability as well as their thermal conductivity are very similar. Graphene has a thermal conductivity in the range of $4.84 \pm 0.44 \times 10^3$ to $5.30 \pm 0.48 \times 10^3$ W/mK for suspended graphene flakes [53]. The thermal conductivity of monolayer hBN is 7-8 times lower, $\kappa = 751$ Wm^{-1}K^{-1}, however it is still the second largest κ per unit weight among all semiconductors and insulators, and decreases with increasing number of layers [54].

High quality hBN nano sheets (1-4 layers) show stronger oxidation resistance than graphene. It starts oxidizing at 700 °C, compared to graphene, for which it starts at 250 °C. The maximum temperature that hBN can sustain in air was shown to be 850 °C, using atomic force microscopy (AFM) and Raman spectroscopy [55]. For graphene in a protective Ar atmosphere defects are induced at 1000 °C [56].

Impermeability of the layers

For this work one of the most important properties of graphene is its impermeability to gases [34, 57] and the fact that macroscopic amounts of gas can be trapped within graphene encapsulation [58]. It was shown that it exerts a pressure of 1.2 ± 0.3 GPa on trapped molecules between the layers [59]. For Li atoms and fullerenes trapped between two layers very dense stacking [60, 61] and in the case of Li also ultra fast diffusion of the trapped atoms [62] was observed.

As monolayer hBN has a comparable strength and adhesion as graphene, it is to be expected that also hBN can be used to trap different gases and molecules. In Ref. [63], it was used to protect metal clusters from corrosion and it was shown that, due to its electrical insulation, it does not form a galvanic cell with them preventing galvanic corrosion. Thus its protective properties are even higher than for graphene.

2.1.3 Stability under (electron) irradiation

Graphene is very stable under energetic electron irradiation. The displacement cross section for an atom ranges from 10^{-4} barn for electrons with an energy of 80 keV to ca. 0.2 barn for 100 keV electrons [64, 65]. This makes it practically impossible to introduce defects when imaging the sample with 60 keV electrons, which is the standard energy used for microscopy in this thesis. Encapsulating different materials with graphene can also protect them from irradiation damage. It has thus been used as a sample support for microscopy in the past [61, 66, 67, 68]. As we have shown earlier [69], it can also be used for imaging small noble gas clusters.

One key difference when conducting microscopy experiments with these two materials is that hBN does get damaged significantly under electron irradiation already at 60 kV [31] with displacement cross sections around 0.01 barn for both B and N. The simulated displacement knock-on energy thresholds (the minimum energy that needs to be transferred to an atom for it to be

ejected) are given by

$$T_d^B = 19.36 \text{ eV}$$

for B and

$$T_d^N = 23.06 \text{ eV}$$

for N in pristine hBN whereas for graphene the energy threshold is given by

$$T_d^C = 22.03 \text{ eV}.$$

These values were obtained from first principles simulations [70]. As these are fairly close for graphene and hBN, valence ionization resulting from inelastic scattering of probe electrons relating to the insulating properties of hBN is expected to cause the difference in the damaging process [31].

Low-energy ion irradiation effects

While defects in graphene can have various shapes [12], in hBN formation of pentagons and heptagons would involve B-B and N-N bonds, which are unfavourable due to the ionic nature of the material. Thus where in graphene the number of dangling bonds can be reduced by rearranging the atoms in other formations this is not the case for hBN. Therefore, the possible defects should be individual as well as multiple missing atoms. In Section 4.4 defects formed by ion irradiation in hBN will be presented confirming this assumption.

2.1.4 Electronic properties

Similarities with regards to structure, thickness, strength and partly also bonding turn into polar opposites when looking at their electronic properties.

Graphene

The electronic structure of graphene is dominated by the p_z orbitals, which are unaffected from the hybridisation of the orbitals forming the σ bands. They are orthogonal to the structure and form a delocalized π-band, which is half filled since each carbon atom has one electron left after hybridization. The result of this is the extraordinary electronic structure of graphene [71]. The most prominent feature is the linear dispersion of the band structure around the K and K' (Dirac)

points in the Brillouin zone. There the bottom of the conduction and the top of the valence band touch at the Fermi level with the density of states being zero. Suspended graphene has a charge carrier mobility of 200, 000 $cm^2V^{-1}s^{-1}$ [72], resulting in an immense electronic conductivity. The dispersion relation is layer dependent. For a monolayer it is linear at the Dirac points and the charge carriers imitate massless Dirac fermions, however in a bilayer a small band gap opens, and the bands follow a parabolic dispersion, resulting in the mass of the carriers to be non-zero [73]. As a result of its unique electronic structure the adsorbance of graphene is 2.3 % of incident white light despite it being only one atom thick [74].

Monolayer hBN

Where graphene is a material with no band gap, monolayer hBN has a wide gap of ca. 6 eV [11, 75]. hBN is often used as a dielectric substrates in graphene electronic devices. The energy bands and optical properties of hBN in 2D and 3D have been calculated theoretically using the tight-binding model in a semi-empirical approach at the K point in the Brillouin zone already in the 1960s [76]. Point defects in 2D hBN have attreacted especially much attention recently [25]. What makes hBN particularly interesting is its good temperature stability of quantum emitters over a wide temperature range [77], their bright emission into the zero-phonon line [78], wide spectral range [79, 80, 81], and the possibility for lifetime-limited emission at room temperature [82, 83]. This makes hBN attractive for a number of different advanced applications [84]. However, although it is well known that quantum emitters are associated with point defects in the material [79, 80, 30, 85, 86], no direct correlation between the defect structures and quantum emission properties has been established. Therefore, being able to selectively create specific types of point defects into hBN would be desirable.

2.2 Sample preparation

For observing the effect of ion or electron irradiation on 2D materials free-standing membranes are necessary. The three relevant parameters for these samples are:

- the material (graphene or hBN), described above,
- how it was produced (chemical vapour deposition (CVD) or exfoliation) and
- the sample support or grid (flexible amorphous carbon, rigid SiN, or a combination).

For most of the experiments combinations of different properties are beneficial. Having amorphous areas for tuning the microscope, multiple thicknesses of the sample and different cleanness levels on one sample is ideal for learning the most from one irradiation experiment.

2.2.1 Production method

For the experiments in this work mono- and few-layer hBN and graphene were used. FLG was fabricated using both mechanical exfoliation as well as stacking single-layer graphene grown via CVD (EasyTransfer graphene produced by Graphenea) on top of each other. For hBN only CVD-grown samples grown on Cu foil were used (Graphene Supermarket). These were mostly monolayer, which also contained few-layer regions as a by-product of the growth.

Exfoliation of few-layer graphene

Micromechanical cleavage, also known as "Scotch tape" method (named after the sticky tape producer), was used for exfoliation [4, 73]. Here a crystal of highly-ordered pyrolytic graphite (HOPG), is put on adhesive tape and thinned down by repeatedly applying the tape to the crystallites (usually 8-12 times). For the final exfoliation step the tape, covered with small crystallites, is attached to a piece of a SiO_2-coated Si wafer. The tape is pulled off and a statistical distribution of graphite/graphene flakes of different thicknesses is left on the wafer. The wafer can be plasma irradiated before and heated after adhesion for a higher yield of larger thin flakes [87]. Using a visible light microscope, the wafer is checked for transferable flakes. The contrast of the flakes in the optical microscope depends on the thickness of the SiO_2 coating. The optical contrast can go up to 12 % for a monolayer when green light is used and the coating has a thickness of 90 nm ± 5 % [88]. Usually flakes have a size of several µm. The advantage of mechanical exfoliation compared to stacked monolayers is the possibility to create flakes of varying, known thicknesses of 1-10 layers at one sample position. This way irradiation effects and implantation efficiency as a function of thickness can be investigated easily. Fig. 2.2 a shows how a flake on a wafer looks like in a light microscope.

CVD-grown graphene double layers

Commercially available monolayers produced by Graphenea were used in this work. They were either bought already transferred onto transmission electron microscopy (TEM) grids or as Easy-

Transfer samples which are CVD-grown graphene on a sacrificial polymethylmethacrylat (PMMA) layer. Cu is mostly used as a substrate to grow graphene monolayers due to its self-limiting growth effect [89]. These grown monolayers are not directly suitable for trapping noble gas atoms between multiple layers, thus for these experiments they were stacked to create artificial double layer or multi layer samples. Where exfoliated samples are AB stacked (referred to as bilayers), stacking CVD-grown monolayers results in random orientations. As CVD-grown graphene is mostly poly crystalline with grain boundaries separating different orientations [89] this results in multiple differing stackings on one sample. Individual CVD-grown flakes are usually smaller than exfoliated flakes, however, they merge and thus can cover areas of several mm. The key differences between exfoliated and stacked samples are summarized in table 2.1.

Table 2.1: **Exfoliated vs. CVD-grown samples**

Exfoliated	**CVD grown**
varying controlled thickness	mostly single layers, some few layers, stackable
oriented stacking	random stacking
cheap, labour-intensive	commercially available
small sample area at specific location	grid entirely covered
holey Quantifoil membrane	both flexible and rigid membrane possible

CVD-grown hBN

Commercial CVD-grown monolayer hBN (Graphene Supermarket) was available on their Cu growth substrate. The growth mechanism is described in Ref. [90].

2.2.2 Transfer to TEM grids

Sample support grids play an essential role for microscopy. For example amorphous areas are needed for tuning the electron beam, as will be described later. The grid also governs which treatment the sample can be exposed to.

Standard grids

Most samples used in this study are obtained on a substrate, be it PMMA, a Si wafer or a Cu foil. Thus they need to be transferred onto a TEM grid for having free standing area. Here gold grids with a flexible amorphous carbon membrane (Quantifoil) and SiN grids with a rigid membrane of different thicknesses (TedPella and Silson) were used. Both grids have thin membranes with holes, the diameters being between 0.5 and 2.5 µm, in a regular pattern on which the samples are free standing. For the transfer the "flat-membrane" side of the grid is put on top of the "sample-covered" side of the substrate. We only conducted transfers where at least one of the two, grid or substrate, is flexible and can adhere to the other. This adhesion is usually enabled using liquids. A drop of isopropyl alcohol (IPA) is put on the substrate-grid-sandwich, the liquid evaporates and the surface tension pulls the flexible membrane towards the rigid one where it sticks. For a successful transfer, uniform adhesion between substrate and TEM grid is beneficial. The process is observed using visible light microscopy.

After adhesion the substrate (Cu foils for CVD grown hBN, SiO for exfoliated graphene or PMMA for EasyTransfer graphene) is etched or dissolved away. This is done with different chemicals, $FeCl_3$ for Cu, KOH for SiO and hot acetone for PMMA. The process for hBN is described in detail in Refs. [31] and [91]. The sample transfer for exfoliated graphene is described in Ref. [92]. EasyTransfer graphene was transferred according to the manufacturer's instructions. After the transfer onto the grids samples were washed in deionised water and IPA. The exact parameters for each sample are given in the results section.

Fig. 2.2 a-c show how a FLG flake with various thicknesses looks like on the substrate in Fig. 2.2 a, the grid on top of the substrate before adhesion in Fig. 2.2 b and the bottom side of the grid in Fig. 2.2 c successfully transferred. Fig. 2.2 d-f show the creation of a double layer graphene sample on a Silson SiN grid where in Fig. 2.2 d one layer of graphene with PMMA (coloured in transparent red) is visible. In Fig. 2.2 e the PMMA from the first layer has been removed using hot acetone (marking still shown) and a second layer of graphene on PMMA has been applied (coloured in transparent green). Fig. 2.2 f shows the grid after removal of the second PMMA layer with the markings for where the two layers are. The control in this process is rather limited but there is always a good chance of creating both monolayer and double layer regions on the same grid.

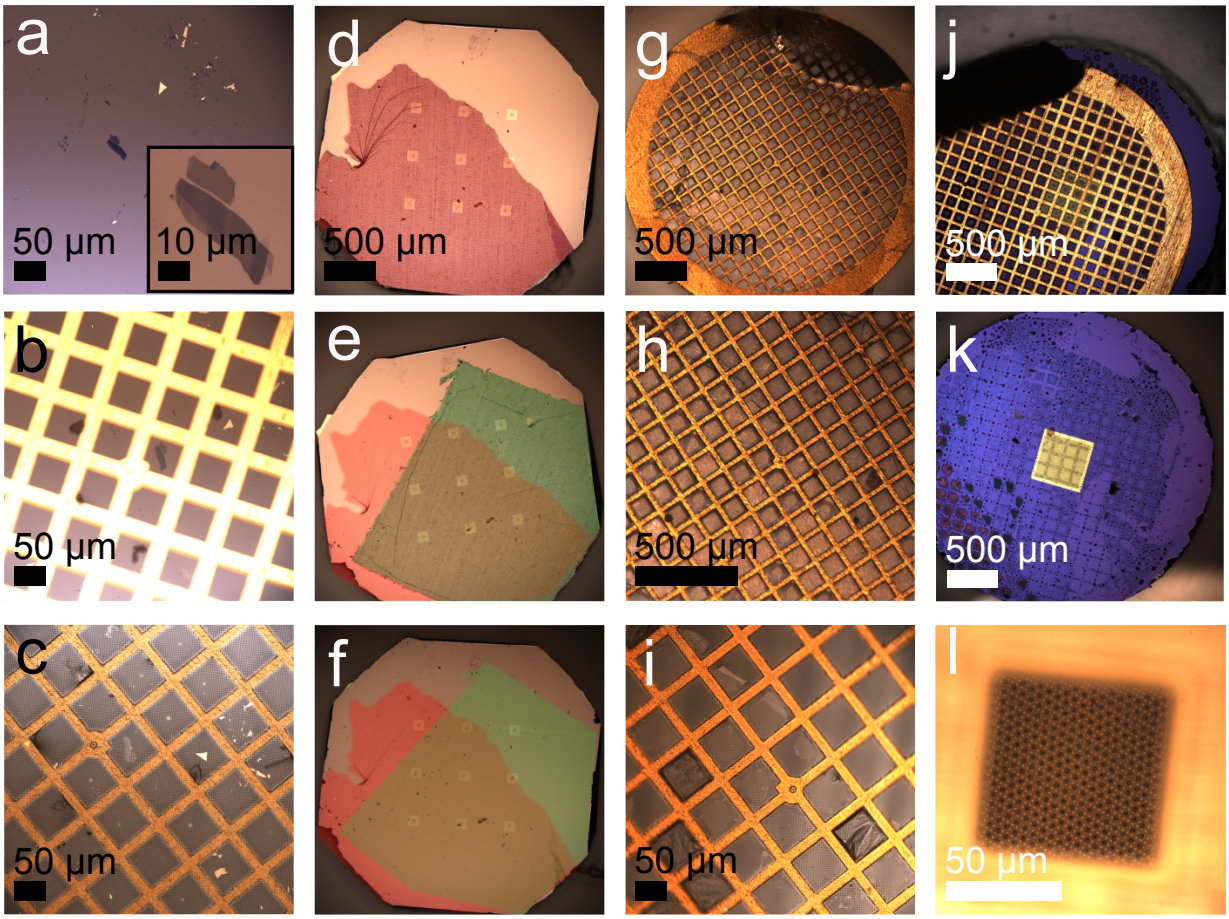

Figure 2.2: **Different kinds of used samples.** (a) Exfoliated graphene sample on a Si-SiO_2 wafer imaged using a visible light microscope. The flake has various thicknesses between one and ≥ 8 layers, based on optical contrast [88]. (b) TEM Quantifoil grid placed on top of the flake with the flake being close to the central marker of the grid. (c) Bottom-view of TEM grid after succesful transfer of the flake onto it. (d) Nine-window SiN grid from Pelco with one layer of EasyTransfer (marked in red). (e) Same grid with another layer of EasyTransfer (marked in green) after removal of the first PMMA sacrificial layer using hot acetone followed by IPA cleaning. (f) Same grid with both layers of PMMA removed, the area where the graphene was placed is marked. g Quantifoil grid after attaching EasyTransfer graphene on PMMA to both sides of the grid. (h) Close up of the same grid. (i) Bottom view of graphene applied to both sides of a Quantifoil grid after PMMA removal. (j) Quantifoil grid attached to SiN grid during evaporation of IPA. (k) Amourphous carbon membrane sticks to the SiN grid after separation of the grids. (l) Overlap of Quantifoil holes (1 μm diameter, 2 μm spacing) and SiN holes (2.5 μm diameter, 5 μm spacing.)

Special grids

For Quantifoil grids two layers of EasyTransfer can be transferred at the same time. Fig. 2.2 g-i shows a double sided EasyTransfer graphene transfer. Here it is fished with both sides of the grid.

This results in the flat side of the grid being covered entirely with graphene and PMMA while on the other side the sample breaks at the gold grid shown in Fig. 2.2 g and Fig. 2.2 h. This results in a combination of monolayer and double layer regions in most of the grid. If relatively clean surfaces are brought into contact, the contamination between the layers is squeezed into pockets due to the pressure between the layers. The second graphene layer is visible in Fig. 2.2 i in some of the areas with slightly brighter contrast.

SiN grids can be beneficial as they are less fragile when exposed to laser irradiation used for cleaning, however, they are also rigid. If a sample on a rigid substrate (Si wafer on Cu foil) is to be transferred onto such a rigid TEM grid, the procedure used in this work is to transfer it onto a flexible substrate, such as Quantifoil, and then transfer the Quantifoil membrane, together with the sample, onto a SiN grid. Fig. 2.2 j-l shows the transfer of hBN on Quantifoil onto a SiN grid. In Fig. 2.2 j the two grids are brought into contact using IPA and subsequent heating (150 °C, 30 min) for stronger adherence. In Fig. 2.2 k the amorphous carbon membrane was mechanically delaminated from the Au grid with a tweezer. Most of the flexible membrane sticks to the Pelco SiN grid. However, the success rate of this method is about one third to half. Fig. 2.2 l shows a high magnification image of the two membranes that are now stuck together. The suspended sample used for the experiments can be found where the holes of the Quantifoil and the SiN overlap. These grids are called hybrid grids in the following. They have the benefit of being very stable while also having amorphous areas which are important for tuning the electron beam for microscopy. However, the amount of free-standing sample is massively reduced.

2.3 Noble gases

Noble gases are members of the main group 8, the last column of the periodic table. The group includes the elements helium, neon, argon, krypton, xenon and radon. As their electron shells are full, they are in the energetically most favourable state and do not form chemical bonds unless special efforts are undergone, thus they are also called inert gases [93]. Due to their lack of chemical bonds their behaviour is governed by the vdW interaction. The atoms show dipolar behaviour at low temperatures that becomes stronger with growing nuclear charge as the electrons furthest away interact with a more strongly screened nucleus. Thus heavier atoms also crystallize at higher temperatures, see table 2.2. All inert gases remain gaseous at room temperatures [35, 36].

Table 2.2: **Summarized properties of noble gases.** The table lists the melting and boiling points of inert gases at atmospheric pressure

	melting point [°C] [93]	boiling point [°C] [93]	crystal structure [94]	lattice constant [Å] [94]	conditions for lattice constant [94]
He	-272.2 *	-268.9	hcp	3.531	**
Ne	-248.6	-245.9	fcc	4.43	4.2 K
Ar	-189.3	-185.8	fcc	5.25	4.2 K
Kr	-157	-152.9	fcc	5.72	58 K
Xe	-112	-107.1	fcc	6.2	58 K
Ra	-71	-61.8			

* Melting point of He at a pressure of 2.6 MPa. Helium can only condensate when pressurized.
** He^4 1.15 K 66 bar, He^3 3.3 K 183 bar

When pressurized, noble gases can also be forced to crystallize at room temperature. The melting curves [95] indicate that a pressure slightly above 1.5 GPa should solidify Ar, a pressure slightly below 1 GPa should solidify Kr and a pressure around 0.5 GPa should be enough to solidify Xe.

2.3.1 Two-dimensional noble gases

Krypton at cryogenic temperatures on graphite surfaces was one of the first ever studied two-dimensional systems. Phase transitions in this system were studied already in the 1970s and 1980s [96, 97, 98, 99, 100]. Heat capacity measurements revealed that a monolayer of Kr on graphite shows different behaviour than bulk [101]. Three layers of Kr appear to be the crossover region where the two-dimensionality of the system is lost [102]. As the van der Waals interaction is isotropic, it only depends on the inter-atomic distance. Thus 2D noble gas crystals assume a close-packed hexagonal structure as was confirmed through ultralow-energy electron diffraction experiments already as early as 1975 [103]. The first real space images of 2D noble gas crystals were recorded via STM in 1998 on a graphite surface [104].

These studies of 2D noble gases were conducted at cryogenic temperatures. The discovery of the impermeability of graphene [34] made it possible to create similar structures at elevated temperatures by trapping noble gases within the van der Waals gap between graphene or hBN and a substrate. This can be done either directly or indirectly.

In Refs. [40, 41] graphene on Ir(111) was irradiated with 100 eV - 5000 eV He, Ne, Ar and Xe. After subsequent annealing, STM topographs showed protrusions that were first misinterpreted as C atoms forming carbon nanoplatelets below the encapsulating layer, and later confirmed as noble

gas aggregates at the interface between Ir and graphene. The implantation process is studied in Ref. [105]. Few hundred to thousand eV ions easily penetrate through the graphene layer and then lose energy in the bulk. At high temperatures the gases leave the bulk and diffuse to the surface where they form pressurized blisters in the vdW gap between the materials. This is most efficient at normal incidence [106]. Using STM, the atomic configuration of 2D Xe clusters trapped between graphene and Ir(111) similarly were even imaged revealing a close packed structure [39]. Crystalline Xe trapped at the interface of hBN and Ir(111) was also imaged at room temperature. The superstructure produced by monolayers and bilayers was imaged to reveal their crystallinity. The blister height was found to be around 2 Å and the average periodicity of the cluster was 4.2 ± 0.1 Å [38]. Interestingly, after annealing to higher temperatures (1500 K) the structures grew larger, which led to substantially lower pressure, thus the Xe superstructure produced by the atoms was not visible anymore. The much clearer visibility of the structure below hBN is appointed to the higher adherence of it on Ir with respect to graphene on Ir.

While these trapping experiments were somewhat indirect, also direct implantation into the vdW gap was done. Individual Ar atoms were trapped below hBN on top of Rh(111) where the noble gases were immobilized at room temperature by the encapsulation which can be difficult to achieve. The implantation energy was 60 eV [107]. Kr^+ at $30 - 120$ eV was implanted below the first layer of graphite at room temperature [108]. Using STM, it was found that thermal diffusion of intercalated Kr was frustrated, similar as for Ar in the aforementioned study. The observed multi-atom nanostructures were explained by already intercalated atoms colliding with incoming Kr. Thermal diffusion was shown to become effective at 873 K, which leads to growth of the Kr nano-structures building up strain in the encapsulating layer, which eventually leads to craters of varying depth after bursting.

In 2021, small noble gas nanobubbles with a radius in the order of 1 nm were studied using STM [109]. Ultralow-energy (25 eV) perpendicular incidence irradiation of He, Ne and Ar was used for implantation into the gap between graphene and Pt(111). The universal scaling for bubbles of trapped materials below 2D membranes found before [110] was shown to break down for the monolayer regime. The pressures inside the bubbles were estimated to reach tens of GPa for radii around 1 nm for He or 1.6 nm for Ar. Bubble formation was only observed for graphene on Pt(111) and not for graphene on Cu(111), explained by lower adhesion between the surface and the encapsulating layer.

2.4 Contamination

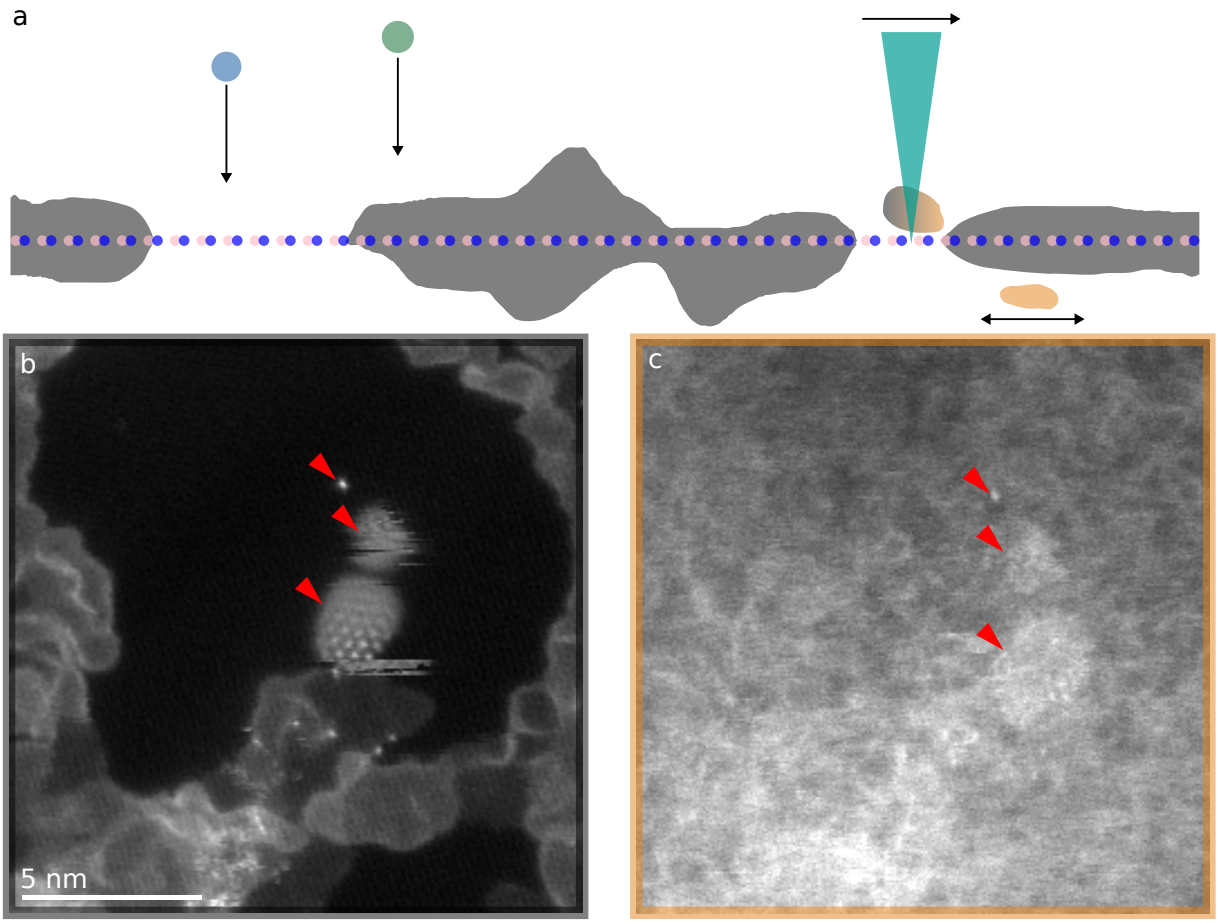

Figure 2.3: **Schematic illustration and images of different kinds of contamination** (a) Illustrative side view of hBN (atoms in pink and dark blue) with static (grey) and mobile (orange) hydrocarbon contamination. An electron beam (shown as a turquoise triangle) is focused onto one part of the hBN while another part is irradiated with different ions (shown as blue and green spheres). (b) STEM-HAADF image of a clean multilayer graphene (dark contrast) with implanted Xe atoms (marked by red triangles) and contamination (bright contrast). (c) STEM-HAADF image of the same position after extended exposure to electron irradiation and subsequent dehydrogenation of diffusing surface molecules leading to pin-down of mobile contamination. The triangles mark the Xe clusters and atom that are still visible through the contamination.

One of the key obstacles when working with 2D materials is surface contamination. Fig. 2.3 a illustrates the side view of hBN (atoms shown in pink and dark blue) with surface contamination (shown in grey), different ions approaching the surface (spheres shown in blue and green) as well as a convergent electron beam (the turquoise triangle) interacting with mobile contamination (shown in orange). It is evident that for observation of thin crystals made of light atoms such as

graphene or hBN an undisturbed line of sight is necessary in STEM. Thus areas that are atomically clean, without amorphous impurities on their surface, are imperative for experiments.

One key goal of this work is to understand the interaction between ions and the material. Contamination is a problem for two reasons. Firstly, the effect of ion irradiation will be changed if they interact also with the contamination. This is an issue as ions with energies that are practical for material manipulation also interact strongly with contamination resulting in a significant impact of ad-atoms and contaminants [7]. Second the effects of irradiation might not be observable as defects and the associated dangling bonds are more reactive than the otherwise inert 2D materials attracting contamination. Additionally, due to their low nuclear charge, Z, C, B and N have a weak scattering potential which leads to low contrast, as will be discussed in the methods.

Thick contamination (more than a few tens of nm) makes samples practically unusable and has to be avoided by optimizing sample production, using well defined protocols and pure chemicals. For the remaining contamination, two classes will be distinguished: Static and mobile contamination. Both probably consist of similar hydrocarbons, however, their interaction with the imaging electron beam differs. While static contamination is present on the sample independent of imaging (exposure to highly energetic electrons), mobile contamination increases with the exposure to the electron irradiation. The longer the area is exposed, the "dirtier" the sample gets within the field of view (FOV), see Fig. 2.3. We believe this to be caused by diffusing hydrocarbon molecules where the electron beam removes hydrogen atoms and breaks bonds. This results in cross linking different molecules and making them stick where they are.

The contamination on the sample was shown to mostly consist of hydrocarbons adsorbed from air [111] as well as PMMA residue, carboxyl and methoxyl [112]. A recent STM study identifies the airborne hydrocarbons to be alkanes with lengths of 20-26 carbon atoms [113]. These are common molecules in the environment and exhibit self-organizing behaviour. They form friction domains that were measured on hBN, graphene and MoS_2. Also silicon is always present on 2D materials [114, 115, 116]. This could be a result of Si or SiO_2 being used in different steps of wet chemistry or CVD, however it is also an element that is very abundant on the earth crust. Occasionally, also Cu [117] or other metals are found on the sample. They could be remnants of the CVD process, especially Cu as our samples are often grown on it. Fe, which can be found often on hBN samples is used for the removal of the Cu foil within $FeCl_3$ acid. These metal clusters typically do not cover the surface on a large scale, and thus play a minor role when creation of a clean surface in the range of some tens to hundreds of nm is desired.

Chapter 3

Methods

3.1 STEM and EELS

Aberration corrected STEM and EELS are the main methods used in this thesis. Here a brief introduction will be given, for deeper insight into the topic Ref. [118] is recommended.

The fundamental properties that make electrons useful for imaging are their short wavelength at high acceleration voltages ($\approx$ 4.8 pm at 60 kV), the fact that they interact strongly with matter, and that they are charged particles and thus interact with electromagnetic fields through the Lorentz force

$$\vec{F} = q(\vec{E} + \vec{v} \times \vec{B}), \tag{3.1}$$

which makes it possible to alter their trajectories using electromagnetic and electrostatic lenses. $\vec{F}$ denotes the force, q the charge $\vec{E}$ and $\vec{B}$ the electric and magnetic field and $\vec{v}$ the velocity of the particle.

3.1.1 Electron scattering

An electron interacts with the sample via elastic or inelastic scattering processes. A process is called elastic when the total kinetic energy of the system is conserved. Here the primary electron interacts with the attractive potential created by the protons in the nuclei screened by the surrounding electron cloud. The interaction changes the trajectories of electrons providing information about the positions of the nuclei in the specimen.

In inelastic scattering the energy of the probing electron is changed due to interactions between

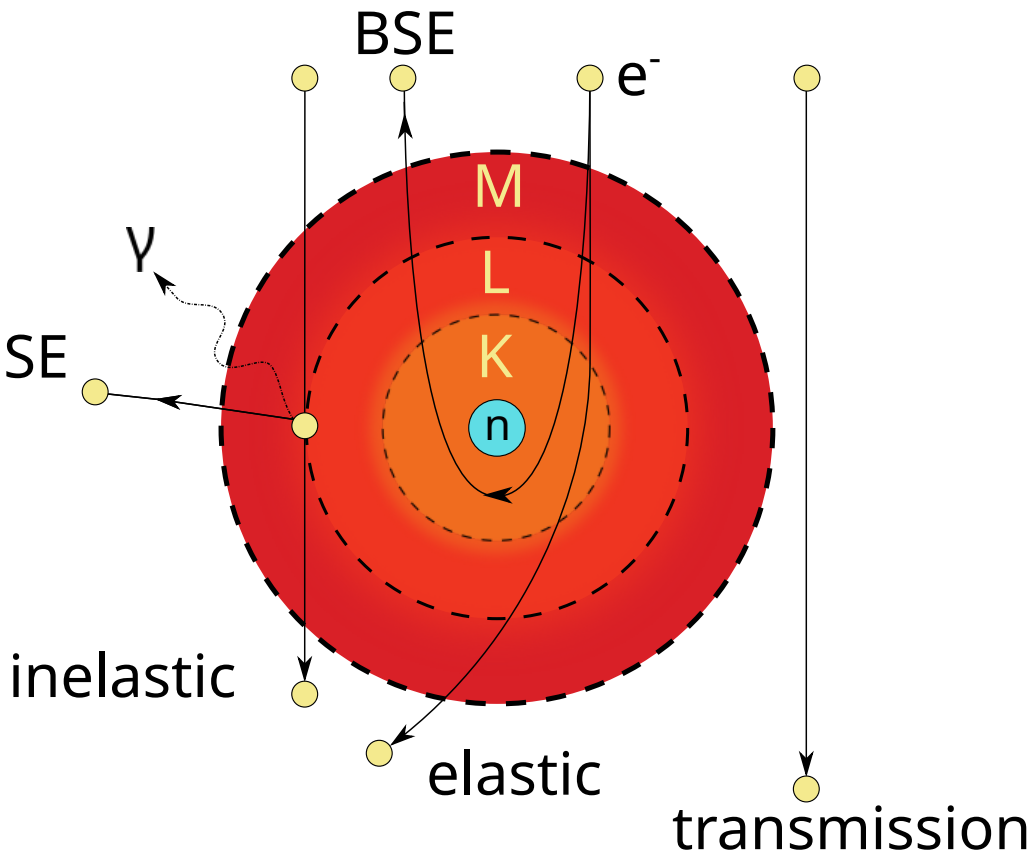

Figure 3.1: **Illustration of possible interactions of a primary electron with an atom.** n refers to the nucleus of the atom, K,L and M indicate the electron shells. The primary electron travels from top to bottom. In elastic scattering, the trajectory is altered from its normal course which can even result in back scattered electrons (BSE). In the shown example for inelastic scattering, the primary electron ejects an electron from the L shell resulting in a significant amount of energy loss. The ejected electron is called SE. The hole is filled by an electron from the Fermi level with the energy difference between the two states being released as an x-ray photon γ which is characteristic for different elements. Reproduced from [119] with kind permission of the author. Copyright ©2020, Bernhard Fickl.

the primary electron and bound electrons or quasiparticles like phonons, plasmons, etc. in the material. Information about the properties of the material, can be collected by measuring the energy loss of the primary electron, the energy of emitted characteristic x-rays with energy dispersive x-ray spectroscopy (EDX) or from the emitted secondary electrons.

3.1.2 Set-up of a STEM

In STEM, a focused electron beam is scanned over the sample. Here annular dark field (ADF) detectors are used to collect elastically scattered electrons to from an image. Inelastically scattered electrons are used in EELS to acquire spectroscopic information about the sample. The magnification is set using scanning coils. The resolution is limited by the size and shape of the probe which is determined by aberrations. The possibility to acquire ADF and EELS signal, and with other microscopes even EDX or SE signal, at the same time, makes this a really powerful technique.

Fig. 3.2 shows a schematic drawing and a photograph of the Nion Ultra STEM 100 in Vienna. Electrons are emitted from a cold field emission gun (CFEG). The emitted electrons are accelerated, travel through the condenser lens system after which they enter the aberration corrector. The corrected beam is then focused using the objective lens creating the atomically sharp probe that is scanned over the sample. It interacts elastically and inelastically with the specimen as described above. Projector lenses are used to spread the beam leaving the specimen and the electrons are collected using detectors. The medium-angle annular dark field (MAADF) and high-angle annular dark field (HAADF) are the detectors used for imaging in this work. A charge-coupled device (CCD) bright field (BF) detector can be used for sample navigation and tuning.

3.1.3 Aberrations and their correction

Already in 1936, Scherzer found that electron lenses have spherical aberration [120]. After the first aberration corrector had been suggested in 1947 [121], it took 50 years for the first working quadrupole/octupole probe corrector to be developed for STEM [122, 123], which made sub-Å resolution imaging possible [124]. For a more in-depth discussion of the history of aberration correction I recommend Ref. [118] or the resources on the website of the Nion company [125]

Tuning (aberration correction) of the beam is done using the Ronchigram method. A Ronchigram is a convergent beam diffraction pattern of a known object (in case of electrons amorphous materials are often used) where the features are comparable to the diffracting wavelength. The aberrations are measured by collecting Ronchigrams with well-defined beam shifts on an amorphous spot of the specimen. A Ronchigram camera (a fluorescent film with a CCD camera) is used for this. From those, the local magnifications and with that the aberration function is calculated. The calculated corrections are then applied and again measured in an iterative process [126]. The

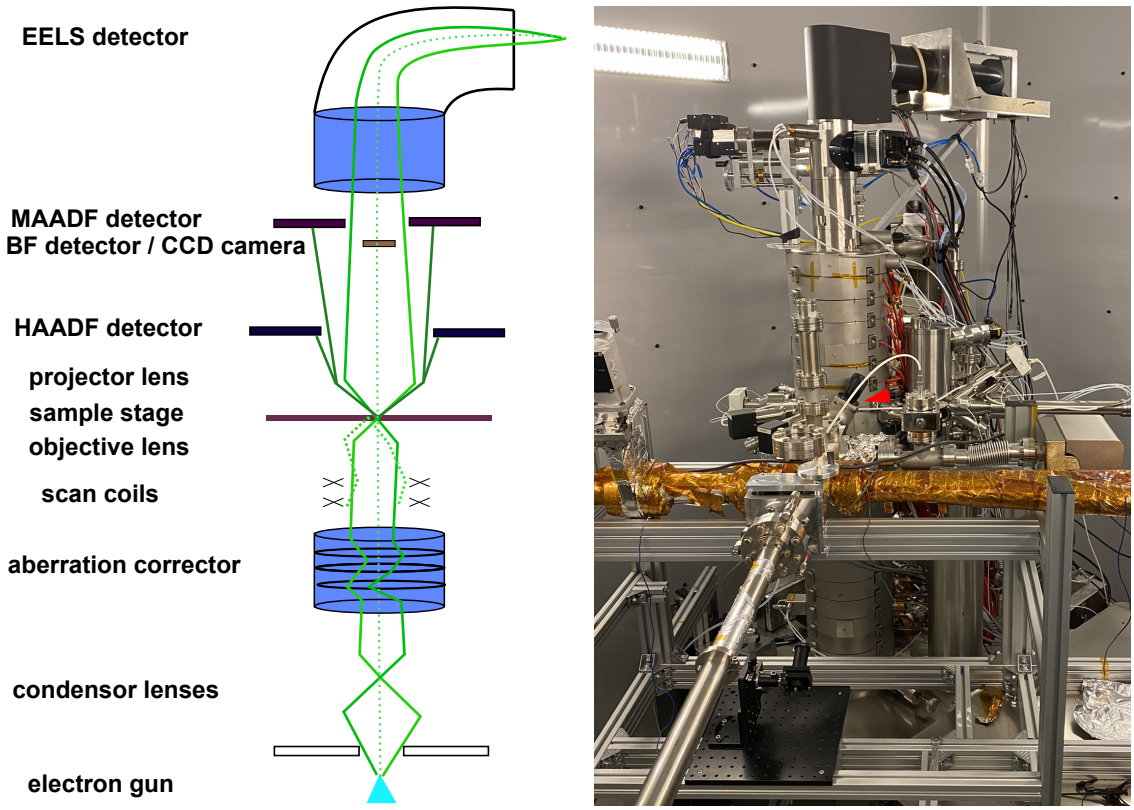

Figure 3.2: **Scanning Transmission Electron Microscope** Left: Schematic set-up of a scanning transmission electron microscope with the electron beam going from bottom to top. Reproduced from [47] with kind permission of the author. Copyright ©2020, Mukesh Tripathi. Right: Photograph of the NION Ultra STEM 100 in Vienna. The red triangle marks the valve connecting it to the CANVAS system.

same camera is also used for taking overview images and for sample navigation.

Annular dark field (ADF) detectors

In ADF imaging [127, 128] a focused electron beam is raster scanned over the sample and electrons scattered to angular ranges $\theta_{min} < \theta < \theta_{max}$ are detected using a ring-like detector. Electronics correlate the recorded position of the beam with the number of electrons hitting the detectors. The more electrons are scattered to the angular range, the brighter that pixel is. Thus, atoms with a high nuclear charge Z and thicker areas appear brighter in the images. The minimum angle, θ_{min}, is chosen such that Bragg reflections are suppressed and thus diffraction contrast is eliminated. This leads to Rutherford scattering of single scattering centres. The intensities detected by ADF detectors are thus integrated scattered intensities by each atom, resulting in the so called Z-contrast (contrast being dependent on the atomic number Z) [129] as Z^{ζ} with ζ in

the range of 1.5 − 1.8, depending on the signal collection geometry and the atomic number of the studied elements [130]. This leads to a straightforward qualitative interpretation of atomic resolution ADF images by providing an easily interpretable contrast between atoms with differing atomic number Z, allowing to probe the local atomic structure and to directly identify defects and heteroatoms.

HAADF imaging is well-suited for resolving structures made of heavy atoms. MAADF provides better contrast for light elements such as boron, carbon and nitrogen, but the accurate Z-contrast is lost as some Bragg scattering is included making the images a bit less straightforward to interpret [118].

3.1.4 Electron energy loss spectroscopy (EELS)

Focused electron beam EELS allows to determine the chemical composition and the nature of chemical bonding at the atomic scale. A magnetic field is applied perpendicular to the direction of motion of the electrons. The relation

$$R = \frac{m \cdot v}{q \cdot B}, \tag{3.2}$$

is gained by combining the Lorentz and the centripetal force. The resulting radius R after travelling through the magnetic field depends on the velocity, v, of the electron which depends on its energy. The charge, q, the magnetic field, B, as well as the mass, m, are the same for all electrons. Electrons that lost (or gained) energy interacting with the sample thus hit the detector at different positions yielding a spectrum. The EELS atlas [131] is usually used as a first reference when analysing spectra. In this work mostly core-loss EELS is used to confirm atomic species. Compositional maps of the specimen can be created by collecting spectra for each pixel of an image. The spatial resolution of STEM EELS is influenced by the probe size and the specific energy loss. The lower the energy loss, the larger is the localisation diameter of the excitation [132].

3.1.5 Technical data

Most samples were imaged at the University of Vienna with the Nion UltraSTEM 100 dedicated STEM instrument at 60 kV with a beam current of 19.4 ± 0.6 pA [133] using either the MAADF or HAADF detector with annular ranges of 60 − 200 mrad and 80 − 300 mrad, respectively. The convergence semi-angle was 30 mrad. Electron energy loss spectroscopy was carried out with

the same instrument using a Gatan PEELS 666 spectrometer retrofitted with an Andor iXon 897 electron-multiplying CCD camera using a collection semi-angle of ca. 35 mrad. The energy resolution of the EELS set-up is around 0.5 eV which is partly due to the electron gun with an energy spread of around 0.25 eV and partly due to the optics and detector. A customized objective and sample stage connects the instrument to an UHV system [134]. In the photograph in Fig. 3.2 (right) the microscope is the vertical metal column in the back, whereas everything that is attached in the front, starting from the valve marked by the red arrow, is the custom built UHV system. The electron source is a 100 kV high-brightness CFEG. The microscope is equipped with a 3^{rd} generation C3/C5 aberration corrector with a minimum probe size of $1-1.3$ Å at $60-100$ kV [135]. The base pressure at the sample is in the order of 10^{-10} mbar, which is around three orders of magnitude lower than that of most commercially available (S)TEMs. The Z-contrast of the instrument in MAADF mode is given by $\zeta = 1.64$ [136].

3.1.6 Automated imaging algorithm

Automated image acquisition provides means to acquire large amounts of data much faster than with manual acquisition. This is made possible by separating the focusing and sample-tracking from the actual recording of the data. The automated imaging algorithm that is used in this work was developed for low-dose imaging by Andreas Mittelberger [21].

Within the algorithm the user defines an area of interest where images should be acquired in a regular pattern at atomic resolution. Four focus references are set manually which form the corners of a quadrangle within which the imaging will be done (illustrated in Fig. 3.3 b by the black crosses). The largest-possible rectangle that is aligned with the natural stage coordinates (shown as large black arrows at the bottom left) is inscribed into them. There the area is filled with an evenly spaced grid of coordinates (illustrated by black squares), based on the image size and the chosen offset between the images. The focus is calculated using a bilinear interpolation function for each stage position. In a serpentine path (illustrated by the green arrow) the stage drives towards each stage position, acquires an image and saves it on the hard disk. Only one drive is used at a time for stability reasons, it is favourable to avoid large stage movements. This is only possible due to the exceptional stage of the instrument where movement in x and y direction do not lead to detectable random changes in sample height (z). With this method up to to 1000 images per hour at atomic resolution from micron-sized areas of a sample can be acquired while controlling the electron dose the sample is exposed to, as every image is taken of an almost

unexposed part of the sample. EBID was used to show the serpentine path in Fig. 3.3 a.

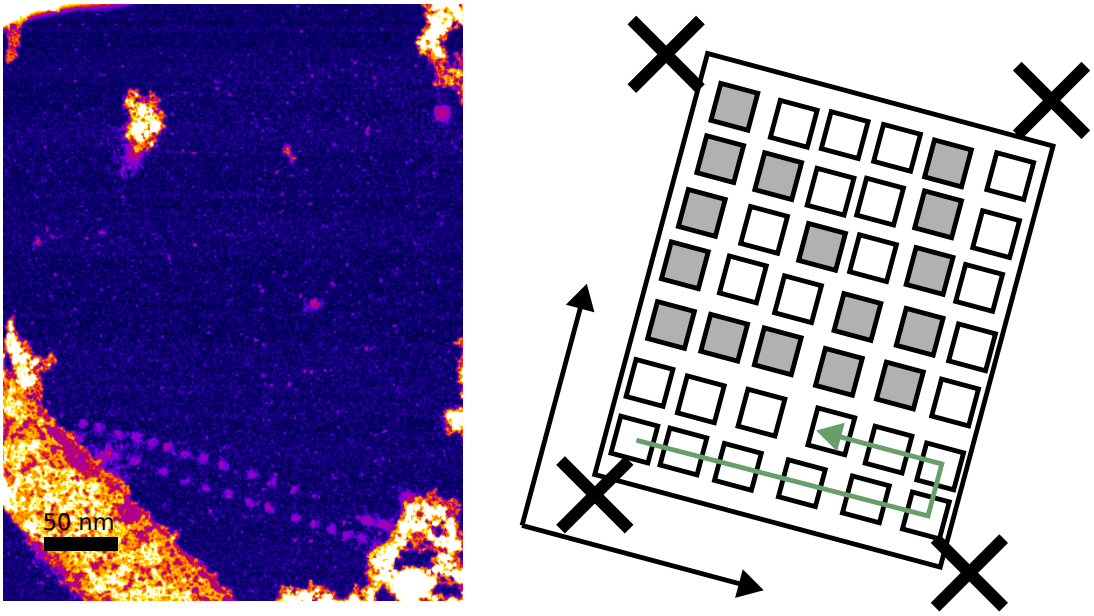

Figure 3.3: **Illustration of Automated Imaging algorithm.** (a) Part of an overview STEM MAADF image (lookup table fire) acquired after an aborted ScanMap (roughly 35 images). The regular pattern of bright dots at the bottom are areas with pinned down mobile contamination with sizes of roughly 5-10 nm in diameter. The parameters used for the ScanMap were FOV 5 nm, 2048 × 2048 pixels, 2.5 µs, offset: 3, sleeptime: 2 s. Image was recorded by Wael Joudi. (b) Illustration of how ScanMap works. The focus is set at four points (black crosses). Within this Four points a rectangle aligned with the natural axis of the microscope (bottom left black arrows) is calculated. Within the rectangle images are recorded in a regular pattern in a serpentine path (green arrow). The images are usually a bit closer at the beginning of a line than at the end due to the hysteresis of the stage. The grey filled rectangles at the top illustrate how patterns can be written by exposing some pixels to electron irradiation while blanking the beam for other pixels.

The parameters that are set in the algorithm are the number of pixels and the dwell time, resulting in the electron dose, the FOV, the sleep time and the offset. The sleep time defines the time between stage movement and image acquisition and is necessary to avoid stage drift while recording an image. It is typically 2 s. The offset is chosen so that the same area isn't imaged twice. Also it is the most practical parameter for determining the number of images that are taken for a given rectangle, FOV and dose necessary for imaging. The e-beam can be blanked during movement and sleep time to increase the control over the dose in the area of interest. The algorithm is supposed to work best when the focus references and all further focus corrections are only set by changing the acceleration voltage, in our case by changing the acceleration voltage,

without adjustment of the mechanical height (z-drive).

3.1.7 Defect pattern writing

Daniel Imrich changed the automatic image acquisition code in a way that chosen frames could be skipped. This gives the possibility to image a specified pattern, which is the same as exposing only this pattern to energetic electron irradiation. This is illustrated by filled grey rectangles in Fig. 3.3 b. As damage can be introduced into graphene and hBN via high energy electron irradiations (described in Section 2.4) this adapted algorithm can be used to create defects within certain areas and thus "write" patterns using high acceleration voltages. These written defects can be filled with atoms similar to Ref. [13] to not only write defects but also trap atoms in them. The electron beam can also be used to pin down mobile contamination to write patterns employing EBID as was done in this work.

3.1.8 Image analysis

This is an adapted version from Ref. [1].

Image filtering can be done by applying a double Gaussian [130] and a Fourier filter. The application of a double Gaussian filter is illustrated in Fig. 3.4. The fast Fourier transformation (FFT) of an image is multiplied with a filter before back transformation. The filter consists of a broad positive Gaussian that cuts out high spatial frequencies and a narrow negative Gaussian that enhances intermediate spatial frequencies at the expense of low frequencies. In the analysis in this work the filter was set automatically such that the parameters of the two Gaussians were dependent on automatically detected FFT spots. Detection of the spots and image calibration was done using the auto scaling algorithm [137] based on the lattice spacing of graphene or hBN.

For the noble gas analysis the radius of the inner Gaussian was set as 0.15 times the distance from the centre to the first set of graphene spots in the FFT and the radius of the outer Gaussian was set as 1.3 times the respective distance to the outer set of FFT spots (or where they should be if resolution is not good enough). The positions of the noble gas atoms were detected with the automatic blob detector [138]. For Fourier filtering, the spots corresponding to graphene were deleted thus removing the lattice after back-transformation.

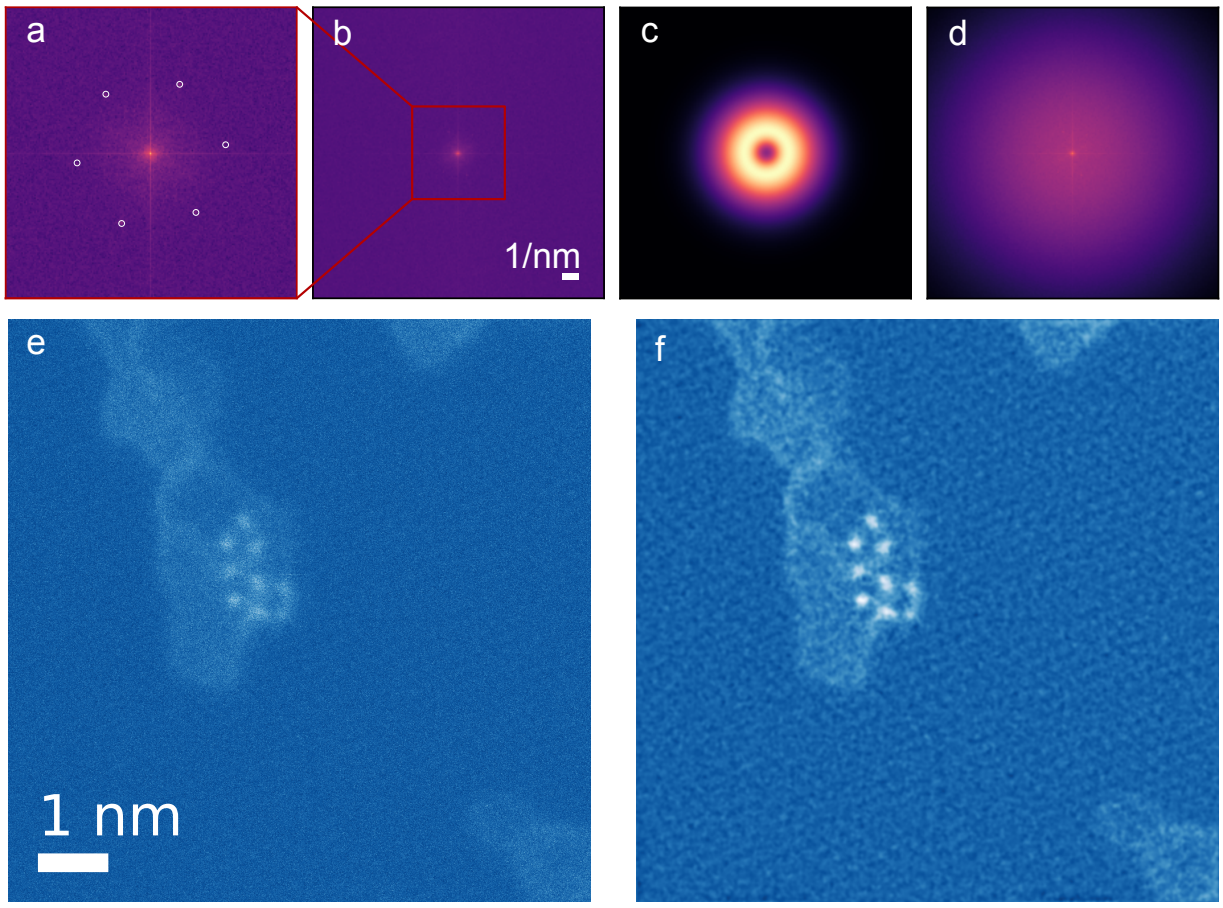

Figure 3.4: **Schematic illustration of a double Gaussian filter.** (a) Zoom in of an FFT of Xe implanted bilayer graphene with poor resolution. The first order FFT spots are marked with white circles. (b) FFT of Xe implanted graphene. (c) Double Gaussian filter that is will be applied to the FFT shown in b. The radii of the two Gaussians can be dependent on the detected FFT spots. (d) Resulting FFT that is obtained by multiplying (b) wit (c). (e) Original image of Xe trapped within a bilayer of graphene. (f) Same image as in e, but double Gaussian filtered. It is obtained by back transforming d.

3.2 Cleaning methods

Even if measures for preventing contamination such as fresh gloves, clean tweezers and high purity chemicals are used, a certain amount of contamination is unavoidable, be it by coming from the air or the chemicals themselves as discussed above. Additional cleaning (removal of surface contamination) steps have to be taken in order to create large clean areas. Especially the regions of interest, such as vacancies or substitutional impurities, attract more contamination due to their greater reactivity. Thus it is especially important to have clean samples for irradiation experiments.

We believe cleaning to be possible via two different processes. In the first, contamination is completely removed or evaporated from the surface. In the second, it is changed such that it gets thicker in some regions, clumping together and piling up, and in the process other regions are left atomically clean.

All samples used in this thesis were baked in vacuum at 150 °C for a minimum of 10 h at insertion into CANVAS. This removes residual water, but is not enough to remove thin hydrocarbon contamination from a surface, which are typically removed only at 500 – 600 °C [139]. Indeed, simply heating graphene in vacuum and under different atmospheres leads to cleaning [140]. In agreement with these studies it was found that while 400 °C is enough to remove PMMA, a contaminant that is often introduced during the transfer that is a typical constituent of contamination, hydrocarbons require a temperature of 500 °C. Washing samples in acetone and then heating them to 500 °C should result in clean samples [112]. Another study suggests baking in activated carbon or different catalytically active materials at moderate temperatures in air to reduce contamination. Active carbon baking at 200 °C for 30 min was found yield 95 % clean samples [141].

Not only chemical and thermal methods can be used to remove contaminants. Scanning graphene in contact mode AFM removes contaminants from the surface [142] which can even be done *in situ* in an electron microscopy where a gold tip is used to wipe a graphene layer clean [143].

However, *in situ* (in the microscopy column) [12, 14] and quasi *in situ* (in the vacuum transfer system) [144, 116] laser cleaning have proved the most practical, reliable and reproducible methods currently available for cleaning

3.2.1 Laser cleaning

There are two parameters we deem relevant for cleaning, the power and the deposited energy. The power at the sample is given by

$$P_{sample} \propto P_{laser} \cdot (1 - L) \cdot \sin(\theta), \tag{3.3}$$

where P_{laser} is the set laser power, L are the losses until the laser reaches the specimen and θ is the angle at which the laser hits the sample. The exact influence of the angle is unknown but approximated to be $\sin(\theta)$ based on simple geometrical assumptions.

The energy deposited at the sample is given by

$$E_{abs} \propto P_{sample} \cdot \tau \cdot \alpha, \tag{3.4}$$

where τ is the time and α is the adsorption coefficient of the substrate and sample. As the adsorption of both hBN and graphene is negligible the substrate is the most important parameter. The optical losses have to be taken into account and additionally the adsorption is reduced by the incident angle of the laser beam. The last relevant parameter is the heat capacity of the grid which is proportional to its mass.

Here we use two laser systems. One laser is integrated on the column of the Nion UltraSTEM 100 which allows localized *in situ* annealing of 2D materials with negligible thermal drift [12, 14] and the second is at the target chamber within the CANVAS that allows quasi *in situ* cleaning [144, 116].

As most of these parameters have not been properly quantified for both of the lasers, the approach for laser cleaning is rather qualitative. The main challenge with laser treatment is, that the grids get damaged in the process. Where the amorphous carbon membrane of Quantifoil grids thins down and becomes unstable, SiN grids can crack, with the thickness of the membrane being the most relevant factor.

3.3 Ion irradiation

Ion irradiation is a very well established method for bulk materials that is widely used in industry to manufacture devices that are used by most of us every day [7, 8]. The strength of ion irradiation is its versatility. The parameters that can be changed are the species and mass of the projectile, the charge state, the kinetic energy, the fluence, the irradiation angle, the temperature and, in the case of thin materials, the substrate. Usually a few different regimes of ion irradiation are distinguished. Swift heavy ions have a "large" mass and a high kinetic energy, whereas for highly charged ions their potential energy is the most important property.

Single charged "slow" ions are the simplest case, because they carry neither much potential nor kinetic energy, but can still alter the properties of 2D materials. Here, low-energy ion irradiation is limited to below 1 keV. Typical irradiation fluences for 2D materials modification are in the range of 10^{12} to 10^{16} cm^{-2} [8].

3.3.1 Nuclear and electronic stopping

Similar to electron irradiation, in ion irradiation the impinging particles can interact elastically and inelastically with the sample. Elastic scattering contributions are summarized under the term nuclear stopping, where the impinging ions mostly scatter with the nuclei of the target. Inelastic scattering contributions are summarized as electronic stopping, as the ions interact mostly with the electrons of the target. Nuclear stopping is dominant at low energy, thus only these processes need to be considered in the experiments presented here.

The (screened) Coulomb potential describing the interaction between the colliding atoms is given by

$$V(r) = \frac{1}{4\pi\epsilon_0}\frac{Z_1 Z_2 e^2}{r} \cdot \phi(r), \tag{3.5}$$

where r denotes the distance between the colliding atoms, Z_1 and Z_2 are the respective atomic numbers of the projectile and target, e is the elementary charge, ϵ_0 the dielectric constant and $\phi(r)$ a screening function that accounts for the electron cloud [145]. Kinetic energy is transferred from the projectile to the target via momentum transfer which can lead to the displacement of one or more target atoms via a ballistic knock-on process. The process is elastic as the kinetic energy of the projectile is transformed into kinetic energy of recoiling collision partners. The maximum transferred energy from a projectile with mass m_1 and velocity v_1 to an atom at rest ($v_2 = 0$) and mass m_2 is

$$E_{T,max} = \frac{4m_1 m_2}{(m_1 + m_2)^2}\frac{m_1 v_1^2}{2}. \tag{3.6}$$

The term stopping originates from implantation where certain implantation depths are the goal and thus stopping powers (energy lost per unit distance) are the relevant factors.

The differential cross section for the energy E_T to be transferred in a scattering event is given by Thomson' formula

$$\sigma(E_T) = \frac{2\pi(Z_1 Z_2 e^2)^2}{m_2 v_1^2}\frac{1}{E_T^2}. \tag{3.7}$$

The probability to transfer a given energy from projectile to target decreases with the velocity squared. Thus by increasing the energy the defect creation efficiency goes down due to a decrease in the nuclear stopping efficiency, however at the energies considered here this does not play a role. Processes, such as collision cascades occurring in thicker samples [146] , also do not play a role in 2D materials.

3.3.2 Ion implantation

Low energy ion implantation has the potential to offer an accurate, controllable and scalable way of introducing dopants into pristine structures without contamination from wet chemistry [7, 8]. While the energy for creating defects with ions just needs to be large enough for the energy transferred to the target to be higher than the knock on energy threshold (discussed in the materials section) [70], for implantation into 2D materials the energy window is quite narrow. Whether the atoms are implanted into the lattice of a monolayer or between two layers, the atom needs to lose enough energy in the impact to be stopped, while it also needs to transfer enough energy to displace an atom to make space for itself.

Into the lattice

Low-energy ion irradiation was predicted to be able to insert impurity atoms directly into graphene [147], which has been demonstrated experimentally for boron and nitrogen [148], phosphorus [149], germanium [150] and manganese [151], which have all been confirmed through atomic-resolution imaging and spectroscopy.

For projectiles with a large mass difference to the target, insufficient stopping becomes an issue. For example, in an elastic collision where momentum is conserved and C is at rest, an Au atom will retain over 88 % of its initial velocity after the impact [13] creating a very narrow (or even non-existent) window for heavy elements to kick out a C atom and be trapped. Ions need to have sufficient energy such that enough of it is transferred for a C atom to be ejected (22 eV [65]), but their energy needs to be reduced enough in the process such that they also bind to the vacancy. Assuming the ion remains bound to graphene when the energy after the collision is $\leq$ 5 eV would limit direct implantation to elements with an atomic mass between 5 and 30 u [3]. Heavier elements than that have experimentally been implanted [149, 150] as in reality the ion impacts are not limited to head-on collisions with carbon atoms. Still, efficient direct implantation is limited to elements that are light enough to be stopped by the one-atom-thick membrane after carbon displacement while they also need to be heavy enough to displace a C atom in the first place.

Implantation experiments are difficult to perform *in situ* with set-ups allowing atomic-scale imaging and spectroscopy, thus contamination is a severe issue in many experiments [148, 149, 150]. As a work around for this introducing impurity atoms via evaporating materials onto graphene and directing their incorporation into the lattice with an energetic electron beam has been demon-

strated at least for chromium, nickel, titanium and iron into monolayer [22] and double layer graphene [23]. A somewhat similar two-step process has been developed within our group where lattice vacancies are created via an knock-on process at higher energy (200 eV) and then the material is deposited on the surface at low energies (25 eV) [13, 14]. This leads to covalently bound substitutional atoms through thermal diffusion and binding with vacancies. This process is also used in this work, where defects are created with energetic noble gas ions produced by a plasma source within CANVAS at well defined energies. The substitutional atoms are then filled by materials introduced subsequently via PVD [3].

Into the vdW gap

Direct implantation into the vdW gap between graphene and a substrate has been discussed already in the materials section. He^+, Ne^+ and Ar^+ were successfully implanted into Gr on Pt(111) using 25 eV [109]. 60 eV Ar^+ has been directly implanted into hBN on Rh(111) [107] and 30–120 eV Kr^+ was implanted below the first layer of graphite [108]. Table 3.1 shows the experimental energy thresholds for implantation and defect creation of all noble gases below the first layer of graphite [152]. These energy thresholds are expected to change for free-standing 2D materials. The irradiation energies that were found to result in noble gas trapping for 2D materials in this thesis are listed in the results section.

Table 3.1: **The experimental energy thresholds for implantation of noble gases below the first layer of graphite.** From Ref. [152]

Rare gas	atomic radius [Å]	penetration threshold [eV]	displacement threshold [eV]	mass transfer factor [eV]	displacement energies [eV]
He	1.40	22.5 ± 2.5	40.0	0.75	30.0 ± 1
Ne	1.54	32.5 ± 2.5	37.0	0.94	34.7 ± 1
Ar	1.88	43.5 ± 1.5	47.3	0.71	33.6 ± 1
Kr	2.02	47.5 ± 2.5	80.8	0.44	35.3 ± 1

3.4 CANVAS system

Both graphene and monolayer hBN are chemically inert, which changes through irradiation-induced defects and the associated dangling bonds. Thus a crucial part for most of the experiments in this thesis is not only to create clean samples and the means to produce defects in a reliable and reproducible way, but also to keep surfaces atomically clean. For this purpose the

CANVAS was developed over the last decade [10]. It is a UHV system that connects various devices used for material alteration with different microscopes. A schematic illustration as well as photographs of the parts are shown in Fig. 3.5. The samples are introduced into the system after they have been transferred onto TEM grids. They are mounted in sample holders, referred to as "pucks" (Fig. 3.5 b), which are transported in sample transportation devices, referred to as "cars" (Fig. 3.5 c) outside (top) and inside (bottom) the vacuum system. Up to three pucks, and thus samples, can be inserted into a car at the loadlock of the CANVAS system (Fig. 3.5 d) where they are baked in vacuum at ca. 170°C for at least 10 h to remove water on the surface and contamination. The pucks (Fig. 3.5 b) are made from titanium to be non-magnetic and are custom designed by our group to work with a unique double-entry stage of the Nion UltraSTEM100 [134, 136]. Cars are moved by hand moving magnets outside the stainless steel vacuum pipes. Within the system, pucks can be loaded and unloaded using linear transfer arms. The base pressure in most areas including the storage units called "garages" (Fig. 3.5 e) of the system is between low 10^{-8} and high 10^{-10} mbar.

While STEM is here crucial for sample characterization, for most experiments the combination of it with other material alteration capabilities is also necessary. This is possible due to the, in principle, arbitrary length of the UHV transfer system that allows direct connection of different devices, even located on different floors of the laboratory. This allows adding and removing devices easily [10]. The stations within the system that are used for the experiments presented here are the laser at the microscope column (Fig. 3.5 f), the target chamber where the plasma source and Faraday cup, a laser and e-beam evaporators are located (Fig. 3.5 h). Other stations that are included but not used in the work presented here, and thus not shown, are the an argon glove box and an AFM. Details about the specific instruments installed are listed in Ref. [10].

3.4.1 Laser at the microscope column

This laser (Cobolt Blues™ 25, Cobolt AB) (Fig. 3.5 g), is a continuous wave solid state laser with a wavelength of 473 nm with a tunable power from 5 – 80 mW. It is equipped with a shutter capable of pulses down to 50 µs and focusing optics coupling it inside the Nion Ultra STEM 100 such that the spot can be aligned concentrically with the electron beam on the sample and can be used during operation. This is done by shooting the light through a CF65 port that was fitted with a Kodial glass window with ca. 93 % transmittance at 473 nm wavelength that corresponds to the emission line of the solid state laser used here. The losses in the optical system including

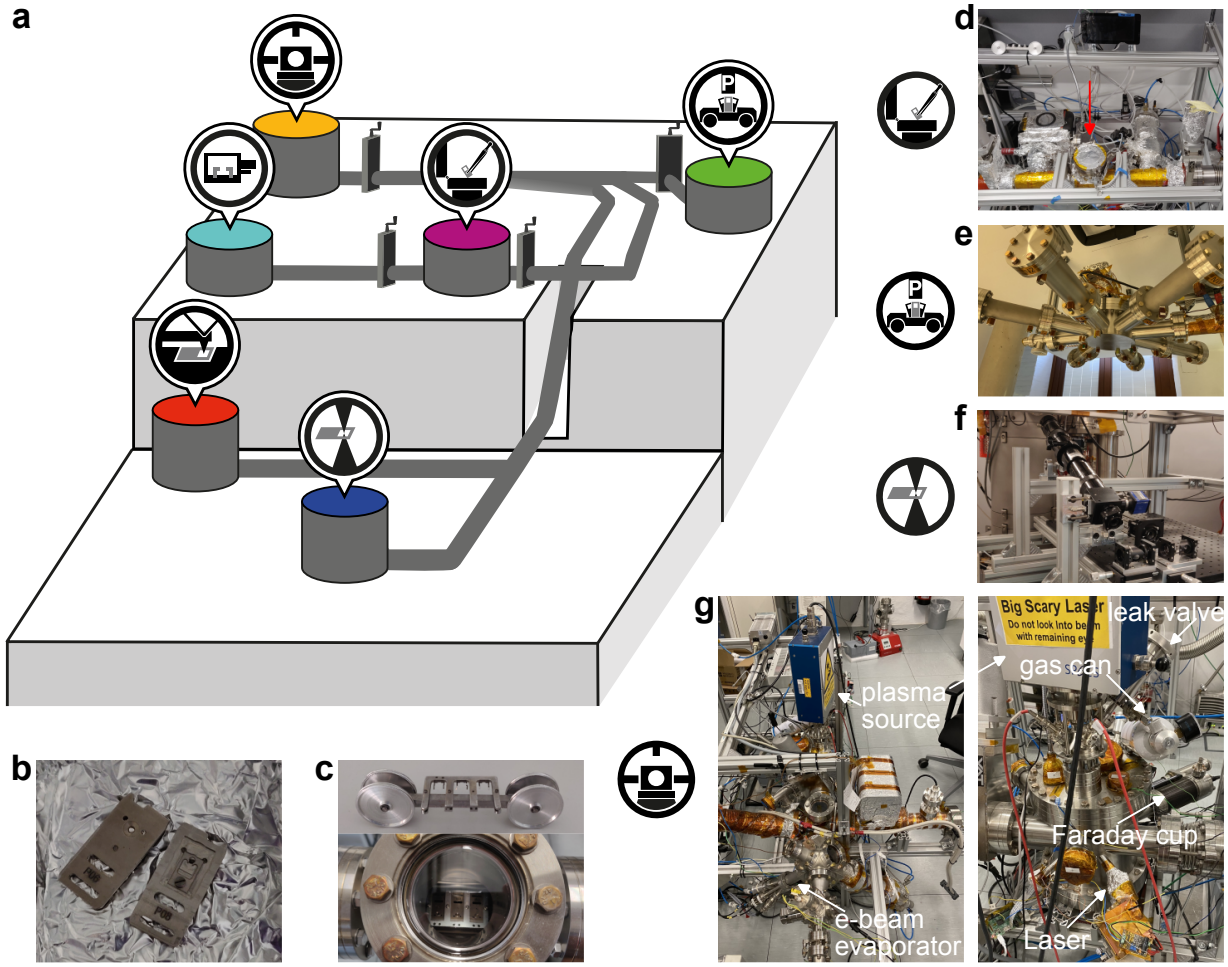

Figure 3.5: **Schematic illustration of CANVAS with photographs of the equipment.** (a) A schematic illustration of CANVAS. (b) Photograph of two pucks that are used as sample holders. (c) Photographs of a car outside and inside of the UHV system. (d) Photograph of the loadlock. The entry port is marked by an arrow. (e) Photograph of one garage. At the bottom of the steel pipes are magnets that are used for moving the cars. (f) Photograph of the laser set-up that is installed at the column of the microscope. (g) Photographs ot the targetchamber from top and side. The plasma source, e-beam evaporator, leak valve, gas can, Faraday cup and laser are marked.

the Kodial glass window are assumed to be 66 %. The laser intensity profile is a 2D Gaussian, and the laser energy is therefore unevenly distributed on the sample. Nevertheless, we know that ca. 68% of the intensity (and hence, absorbed power) by definition lies within the area enclosed by the FWHM ellipse. Due to an incidence angle of 25°, the laser spot has the shape of an ellipse with a main axis of 28.7 ± 0.7 µm and a minor axis of 35.1 ± 0.7 µm. It provides a very precise tool for removing contaminants in a localized area as the incident angle, laser spot size and position where the sample hits are highly reproducible and the energy and time can be set precisely. The

power density within the full width half maximum (FWHM) (ca. 3000 μm^2) of the beam at 35 mW, taking the losses (66 %) and the incidence angle (25 °) into account, is $(1.08 \pm 0.04) \cdot 10^6$ Wm^{-2}.

3.4.2 Target chamber

Material alteration is done in the target chamber and the connected volume. A rotatable linear drive is used to pick up pucks from cars and handle them during the various possible experiments. There are three fundamental and two additional capabilities. The fundamental ones are:

- samples can be heated via laser illumination,
- atoms can be deposited via PVD using either a vacuum thermal evaporation (VTE) source or one of four e-beam evaporators and
- samples can be irradiated with ions using a plasma source.

Additionally a bias can be applied to

- a Faraday cup to measure the current at different biases, or to
- a deceleration set-up to reduce the energy of ions impinging the sample

The sample can be positioned via a linear drive such that it can be illuminated by laser, ion irradiated and exposed to PVD one after another. For some treatments, in particular laser and plasma, they can be used even at the same time.

Target chamber laser

The target chamber laser is a 6 W 445 nm wavelength continuous wave diode laser (LASERTACK) with tuneable power and a spot size of ca. 0.3×1.5 mm^2. The power is set by changing the duty cycle. The illumination time is usually in the order of seconds to minutes and can be set via the controller or manually by moving the sample into and out of the beam. The laser is difficult to focus and the angle of incidence can not be set precisely, however, it is roughly 30 ° when the puck is held straight by the linear drive. Laser cleaning results will be discussed in the next chapter.

The power density at a 30 % duty cycle, taking losses (ca. 20 % based on beam divergence and transparency of the of the glass window) and homogenous energy distribution within the area into account, results in a power density of $(1.1 \pm 0.4) \cdot 10^6$ Wm^{-2} for a puck held in a horizontal position.

PVD capabilities

There is a single and a triple e-beam evaporator as well as a Knudsen cell VTE installed [10]. E-beam evaporator as well as PVD will be introduced later.

Plasma source

The device used here is a microwave plasma source (MPS) using electron cyclotron resonance (ECR) with a reaction chamber built for oxygen and oxidizing gases operated in hybrid mode. The source is described in detail below. It is used in combination with a Faraday cup, an illustration of this is shown in Fig. 3.6.

Faraday cup

The ion beam produced by the plasma source can be analysed using a Faraday cup. It is designed to accurately measure the primary positive ion beam current from an ion source. For calculations in Section 4.4 it is assumed that everything that enters the aperture (placed 25 mm from the source) also is measured by the Faraday cup. The diameter of the aperture is 6.35 mm. A magnet at the entry is used to filter out electrons which could otherwise enter the cup. This is necessary as the plasma source produces a beam of electrons, ions and neutral atoms. The current can be measured at different biases using a remote-controlled power supply. This enables systematic analysis of the energy and fluence of the ions shown in Section 4.2.3.

As the Faraday cup is placed at a 25 mm distance and the sample is at 20 mm, the beam divergence leads to a difference in the measured current and the current at the sample. We estimated that this leads to the expected current at the sample being a factor of 1.4 higher than the measured current.

Deceleration set up

As the ions leaving the plasma source usually have energies above 100 eV additional measures have to be taken for conducting ion irradiation at lower energies. A holder was specifically developed for biasing samples the same way as the Faraday cup. It will be referred to as the deceleration set-up. It consists of a ceramic puck holder that was built such that our samples are electrically isolated from the rest of the system and can thus be biased separately. The same remote controlled power source as for biasing the Faraday cup is used here.

3.5 Plasma creation

Plasma is generated by supplying energy to a neutral gas causing molecules and atoms within the feed gas to be ionized. Here this is done via electron-impact, however, other sources of energy could be photo-ionization, heat or adiabatic compression. At pressures below 10^{-2} mbar microwave-excited and magnetic-field-supported ECR are very effective [153].

Within every volume of neutral gas there are always a few electrons and ions as the result of cosmic rays or radioactive radiation. When an electric field is applied there, free charge carriers are accelerated and collisions create more charged particles. An avalanche of charged particles is created that results in a steady-state plasma, balanced by the charge carriers leaving the plasma reaction chamber [153].

The electric field thus couples its energy into the plasma via collisions with other particles. In elastic collisions with atoms and molecules electrons retain most of their energy due to their small mass. Energy is transferred primarily via inelastic collisions, ionizing atoms and molecules along the way.

The power absorption (P_{abs}) per volume (V) is given by

$$\frac{P_{abs}}{V} = \frac{1}{2} n_e \frac{e^2}{m_e \nu} \frac{\nu^2}{\nu^2 + \omega^2} E_0^2, \tag{3.8}$$

where n_e denotes the electron density, e the electron charge, m_e the electron mass, ν the electron-neutral collision frequency and ω the angular frequency of the electromagnetic field with amplitude E_0.

For low pressures additional magnetic field can be used. The Lorentz force causes a circular

motion of electrons and ions in an magnetic field B with the cyclotron frequency (ω_c) is given by

$$\omega_{ce/i} = \frac{eB}{m_{e/i}}, \tag{3.9}$$

where subscript e and i stand for the electrons and ions, respectively. This is illustrated in Fig. 3.6.

3.5.1 The MPS-ECR-OH source

The MPS uses ECR to create a stable plasma. Microwaves with a frequency of 2.45 GHz, λ = 12.24 cm are generated by a magnetron and then coupled into the plasma reaction chamber. The radiation accelerates electrons which ionize atoms along the way. Due to the low pressure in the chamber the power absorption is low due to low collision frequency ν and n_e (equation 3.8). A magnetic field B of 86 mT is used to trap the electrons in an electron cyclotron motion with a frequency ω that is (almost) in resonance with the microwaves of 2.45 GHz. This enhances the plasma density as electrons undergo ECR motion which enhances the electron path length and thus the probability of collision with other molecules and subsequent ionisation is increased. ECR plasma sources work in the pressure range 10^{-5} to 10^{-2} mbar[153]. Typical values for electron and ion energies hitting the target should be 5 eV and between 10 eV and 25 eV, respectively. The plasmas are usually very clean (few unwanted particles and sharp energy distributions) due to the low collision rates.

3.5.2 Operation of the source

Fig. 3.6 shows the irradiation set-up in the target chamber (left) as well as a schematic drawing of the reaction chamber of the plasma (right). The plasma source produces ions and electrons as well as neutral atoms and molecules that flow towards the sample. The Faraday cup and the sample can be biased and moved into and out of the beam. In the reaction chamber microwave radiation is induced from the top. The gas is let in from the side and is ionized. At the exit there are three apertures, an insulating one, the anode and the extractor. Depending on the apertures that are chosen one can operate the source in atom, ion and hybrid mode.

In atom mode only the insulating plate is used. When using divalent molecules such as N_2, O_2 or H_2 this results in a low kinetic energy beam of reactive atoms. For an aperture with a large hole, as in our set-up, also some plasma will flow out.

In ion mode the two conductive apertures, extractor and anode, are used to extract and accelerate

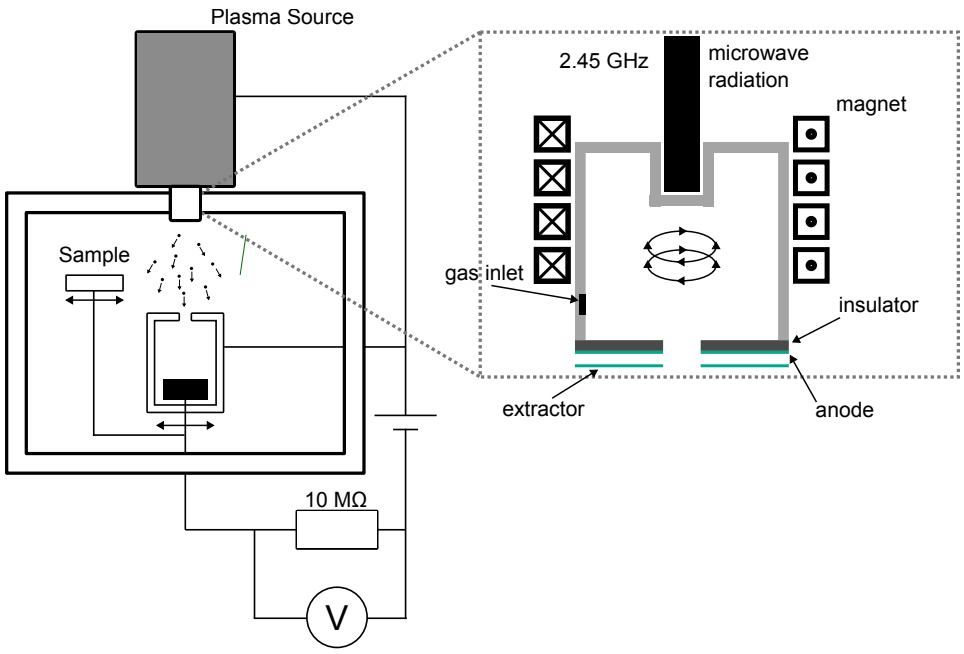

Figure 3.6: **Illustration of the plasma source in the target chamber.** The left side shows an illustration of the side-view of the target chamber. Ions leave the plasma source and travel downwards where either a Faraday cup can be moved into the beam to collect them or the sample can be moved into the beam for irradiation. A voltage can be applied to both enabling biased current measurements and deceleration. An enlargement of the reaction chamber of the plasma source (modified version from Ref. [153]) is shown on the right side. It shows the antenna introducing the microwave radiation, the magnet which induces cyclotron electron movement. Gas is let in from the side. While ions and electrons exhibit cyclotron motion neutral gas just flows out of the reaction chamber. Three apertures are used, an insulating aperture, the anode and the extractor.

the beam. Ions drifting past the anode are accelerated the potential difference between positive anode behind them and the lower potential of the chamber before them. By applying a negative bias at the extraction grid more ions can be extracted resulting in a higher beam current.

The hybrid mode combines the two modes. A pair of conductive grids allows ions to be added and accelerated while the confinement through the insulating aperture makes it possible to operate the source at lower pressures than in pure ion mode. As this source is operated in hybrid mode the resulting beam mostly consists of low energy neutrals and high energy ions.

The operating pressure in the target chamber typically ranges from $< 10^{-7}$ to 10^{-5} mbar. This pressure is significantly lower than the one in the reaction chamber which is required to stay within a certain range, typically around 10^{-3} mbar in order for the plasma to be sustained. The gas flow rate can be adjusted as can the magnetron power.

An Al_2O_3 crucible with a 1×1 Al_2O_3 aperture and NiCr grids as anode and extractor are used. The distance from the source to the sample X_d is about 20 mm. The spot diameter is given by

$$d = 2X_d \tan(\vartheta) + 25 \text{ mm} \tag{3.10}$$

with ϑ being 60° for low energy ions resulting in a beam diameter of $d = 80$ mm which corresponds to an area of roughly $50.6 \cdot 10^{14}$ nm.

The flow of gases is controlled via a leak valve attached to the plasma source (Fig. 3.5 g). The standard operation settings are anode voltage of 0 V and extractor voltage of -60 V with a magnetron current of 16 mA. This should result in a beam consisting of thermalized (energy below 1 eV) atoms and, with the used extraction bias, ions with controllable energy of $50 - 1500$ eV. It is recommended to work slightly above the minimum working pressure.

3.6 KIIA - implantation set-up in Helsinki

This is an adapted version from Ref. [13].

Some samples were irradiated at the University of Helsinki using the 500 kV ion implanter KIIA, a linear accelerator produced by High Voltage Engineering. For details on ion sources and accelerators Ref. [154] is recommended to the reader. To reduce sample contamination during the implantation process, all samples were baked in air for 1 h at 300°C and inserted warm into the irradiation set-up. Some samples were heated during the implantation using radiative heating with halogen lamps.

In the accelerator, the ions are extracted from the plasma at 20 kV and 10 mA. A double-focusing 90° analysing magnet is used for mass filtering resulting in an isotopically pure beam of positive ions which can be accelerated over the main high voltage potential (0–470 kV) in the accelerating tube. It is focused by electrostatic quadrupole triplet lenses, and a switching magnet is used to steer it through the implantation beam line. Neutral particles are filtered via a neutral trap consisting of horizontal deflection plates connected to a DC voltage bending the beamline a few degrees. While charged particles will follow the bend in the beamline neutral particles continue in straight line and do not reach the target chamber. Here the final deceleration takes place in a multielectrode deceleration lens. The lens consists of three cylindrical elements and is connected to the samples creating a decelerating electric field for the charged ions. It was designed to allow implantation at ultra-low energies with the highest decelerations being 20 kV at the time. The

exact energy of the beam was set by biasing a grid in front of a Faraday cup and measuring the current reaching the cup. When the current was 0 all ions were stopped/deflected and thus we knew the exact energy of the beam. The energy distribution at the very low energy range is centered at the chosen energy with a tail extending to higher energies. Therefore ions with slightly higher energy than the intended one also hit the sample. The beam is swept over the area of 1 cm^2 ensuring irradiation of the entire sample surface. This allows monitoring the fluence by scanning over four off-axis Faraday cups located outside of the target area.

3.7 Physical vapour deposition (PVD)

In PVD a target material gets sublimed or evaporated and transported to the specimen in gaseous phase and condensates there. It is an umbrella term for different vacuum deposition methods such as thermal evaporation, e-beam evaporation, arc evaporation, pulsed laser deposition and sputtering. After transportation the evaporated atoms, ions or clusters can stick to the sample. While in CVD the precursors are gases that react on the specimen surface, often with catalysts involved. In PVD the process consists of evaporation and sticking.

Here e-beam evaporation is used. A tungsten filament is resistively heated and emits an electron current in the mA range. These electrons are accelerated towards the target material, a rod in our case, that can be moved into and out of the loop-shaped filament. A bias voltage of up to 1 kV can be applied between the filament and the target, which leads to energy being transferred from the electrons to the rod. This is particularly useful for materials with a high melting temperature as locally a very high temperature is reached that leads to evaporation. The evaporates particles form a beam that exits the evaporator through a nozzle.

For evaporation the sample is moved into the line-of-sight of the evaporant with a rotatable linear drive. The evaporation rate is estimated using a flux monitor which measures ions coming from the evaporant, and is determined experimentally using STEM. Particles that come in touch with the sample are either reflected or adsorbed. Adsorbed particles can either stick directly, diffuse and stick later or be desorbed after some time. The adsorption can be either physisorption, where molecules loose enough energy on impact and are unable to overcome the desorption threshold, or chemisorption where the it binds to the target. The average lifetime of an adsorbed atom, τ, depends on the temperature of the surface, T_S (usually room temperature) as

$$\tau = \tau_0 e^{E_{des}/k_B T_S}, \tag{3.11}$$

where E_{des} is the desorption activation energy per atom and k_B is the Boltzmann constant. During evaporation the vapour is supersaturated at the sample, meaning the vapour pressure exceeds the equilibrium vapour pressure which leads to condensation on the surface. This is, however, only true when evaporant and specimen are the same material, otherwise it is less straightforward.

3.8 Molecular Dynamics simulations

This is an adapted version from Ref. [1]. The Simulations were carried out by my colleague Harriet Åhlgren, the parameters are shown for completeness.

The molecular dynamics (MD) simulations were conducted using the Large-scale Atomic/Molecular Massively Parallel Simulator (LAMMPS). The periodic system consisted of two 10×10 nm^2 AB-stacked graphene layers (7872 C atoms) with the interlayer distance of 3.39 Å relaxed to a local energy minimum with the Polak-Ribiere modified conjugate gradient algorithm [155].

The defected graphene sheets with an interlayer bond and a defect with negative curvature were created by introducing the defect to the relaxed AB-stacked graphene and re-relaxing the system. After the initial relaxations, the noble gas atoms were introduced between the graphene layers in the 2D form as observed in the experiments and the system was relaxed again.

Optimised 3D clusters were obtained from these 2D forms by annealing the cluster without graphene at 80 K over 40 ps followed by cooling down to 1 K during 800 ps followed by relaxation. The rapid annealing and slow cooling was introduced to escape possible local energy minima.

For observing the cluster transformation into 2D, two optimised 3D clusters (Kr_6 and Kr_{12}) were individually placed between the relaxed graphene sheets and then relaxed again.

The room temperature dynamics of a single atom, a three-atom cluster and a seven-atom cluster were simulated by first ramping the temperature from 0 K to 300 K over 0.2 ns, after which the simulation was run at 300 K for another 1 ns. The output was printed every 500 steps with a time step of 0.2 fs.

The pressure of the Kr and Xe clusters were calculated from a 4×5 atom semiperiodic cell. The bond lengths were scaled to the selected value and the forces (F_y) between atoms taken from the initial structure along the nonperiodic direction when conjugent gradient energy minimisation

was started. Pressure was calculated with $P_y = F_y/A$, where A is the 2D area given by the distance between two neighboring atoms and the height of the van der Waals gap containing the cluster (3.4 Å for Kr, 3.3 Å for Xe).

Kr and Xe interactions were described via the Lennard-Jones potential, with the Kr-Kr and Xe-Xe parameters $\varepsilon_{\mathrm{Kr}} = 30.7$ meV, $\sigma_{\mathrm{Kr}} = 3.6233$ Å and $\varepsilon_{\mathrm{Xe}} = 44.1$ meV, $\sigma_{\mathrm{Xe}} = 3.9460$ Å) [156] and the Kr-C and Xe-C with parameters ($\varepsilon_{\mathrm{Kr-C}} = 10.7$ meV, $\sigma_{\mathrm{Kr-C}} = 3.5116$ Å and $\varepsilon_{\mathrm{Xe-C}} = 12.8$ eV, $\sigma_{\mathrm{Xe-C}} = 3.673$ Å) calculated using the Lorenz-Berthelot mixing rules [157, 158]. Carbon-carbon interaction was described by AIREBO potential [159], including the van der Waals interaction.

Chapter 4

Results and Discussion

4.1 Laser cleaning

Laser annealing was used to clean samples. The laser at the microscope column [12, 14] as well as the one at the target chamber [144, 116] were used for this. As mentioned in Section 2.2.2, the sample grids play here an important role. The energy power and time for creating hundreds of nm^2 of free-standing clean monolayer sample can range from 7 mW, 7 ms pulses (hBN on standard TEM Quantiofoil grids) to 80 mW, 6 min illuminations (monolayer graphene on μm thick SiN sample grids used for correlated AFM STEM measurements). The deposited energy is proportional to the adsorption of the grid while the thermal mass and heat conductivity govern the temperature. A qualitative description of the results of laser treatments of different samples is given here as the temperature can not be measured directly. Also the adsorption, thermal mass and heat conductivity of the grids were not measured.

Conducting laser cleaning in the microscope column is advantageous as the small spot size of the beam makes it possible to carry out multiple cleaning experiments on one sample. Also the effect of laser irradiation can be observed *in situ*. Fig. 4.1 shows how the contamination on a graphene monolayer changes over seven 40 mW, 10 ms laser pulses. In general the dark area, corresponding to monolayer graphene, grows, however the contamination sometimes locally also grows after some laser pulses.

Very clean sample areas, such as in figure 4.1, are not necessarily beneficial. If medium-sized clean areas are created with dirt still separating them, similar to the overview image in Fig. 4.4 a, the sample is still clean enough for most experiments, however the contamination serves as a

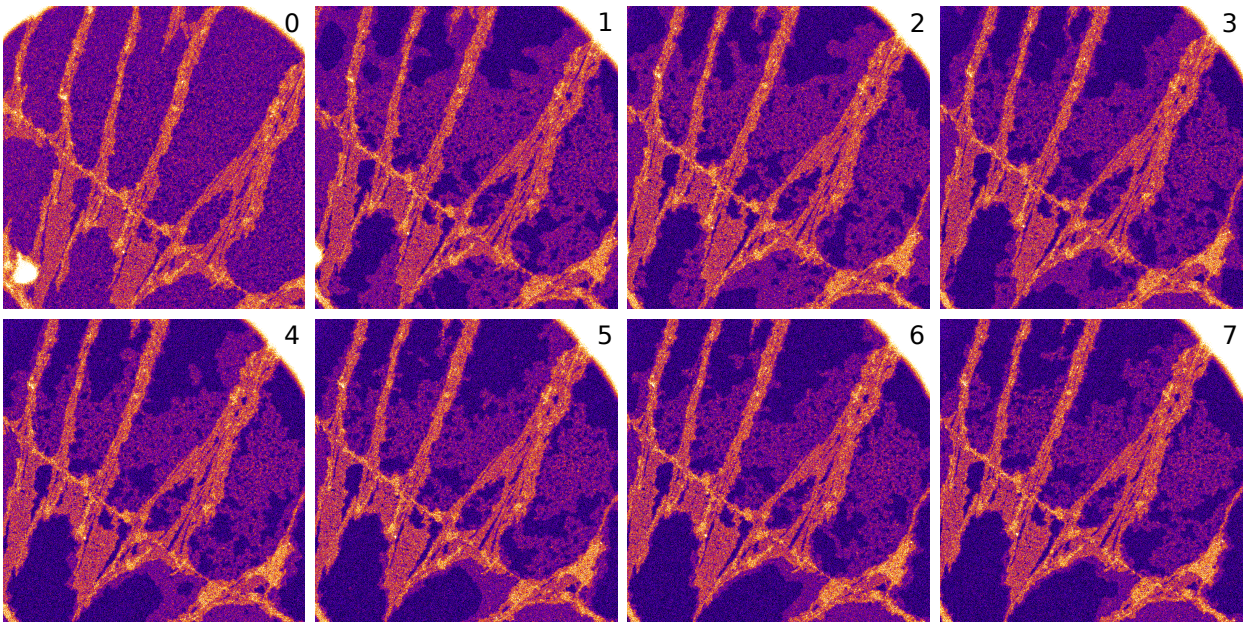

Figure 4.1: **The effect of laser cleaning on free-standing monolayer graphene.** STEM-MAADF images with a nominal FOV of (1024×1024) nm^2. The sample is a CVD-grown monolayer of graphene on a Silson SiN grid imaged before laser pulses. The laser beam was aligned concentrically with the imaging electron beam. The number at the top right corner tells how often the area was hit with a 40 mW, 10 ms laser pulse. Qualitatively there are four different contrasts on the graphene membrane. A very bright cluster on the first image on the bottom left. Thick (bright) contamination stripes that can not be removed with the laser. Thin (darker) contamination areas that change between the laser pulses. The dark contrast corresponds to monolayer regions, growing with the amount of energy deposited.

diffusion barrier for mobile contamination.

4.1.1 Electron irradiation effects

When referring to removal of contamination by laser in electron microscopes, it is important to make a distinction between sample areas that have been and those that have not been irradiated with electrons. The reason is that during TEM observation hydrocarbons, that form the contamination are bombarded by electrons and thus undergo dehydrogenation. The remaining carbon forms C-C bonds and graphite-like structures with stability similar to that of graphene, making the removal of such contamination a challenge. This tendency is visualized in Fig. 4.2 where before the laser pulse an area was imaged with the electron beam. The figure shows a zoom series of the sample after laser annealing. Where the sample was exposed to a high dose of

high energy electrons cleaning does not work as efficiently. This sample was also Ar^+ irradiated. The triangles on the image point at the implanted bubbles.

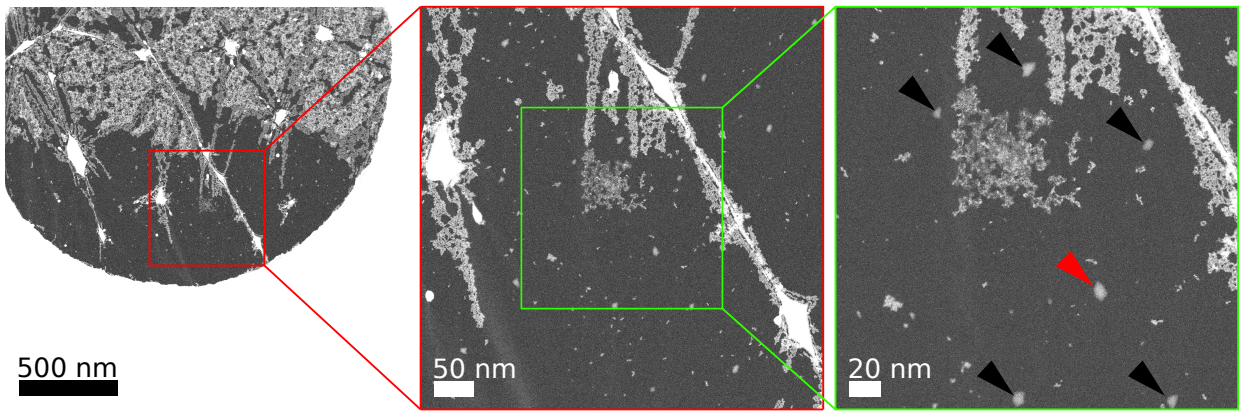

Figure 4.2: **Exposure of contamination to energetic e-beam changes the composition and properties** STEM-MAADF zoom series of Ar^+ irradiated double layer graphene. A nominally (60×60) nm^2 area was imaged before laser cleaning which changes the composition of contamination that is is harder to remove. 25 mW, 1 s laser illumination was used to clean the sample before imaging. Implanted Ar bubbles are visible and marked with black triangles.

4.1.2 Substrate fragility

If higher powers result in higher temperatures and thus in cleaner samples the question arises why the maximum power is not always used. This brings us to the biggest issue with laser cleaning: Samples and especially grids are destroyed by exposure to intense laser radiation. Thus there is a balance between cleaning the specimen and breaking the grid. Damage could be cracking for SiN membranes whereas holey carbon membranes get thinned down until eventually they are too unstable for imaging.

Fig. 4.3 a shows the effect of 15 mW 1.7 ms laser irradiation on a Graphenea Quantifoil grid. The spectra show the low-loss EELS signal on of the membrane before and after laser treatment. For estimating the damage introduced to an amorphous carbon Quantifoil membrane first the thickness (t) which is proportional to of the ratio of the intensity of the zero-loss peak (ZLP) (I_{ZLP}) and the intensity of the plasmon peak ($I_{plasmon}$) is calculated as

$$t \propto \frac{I_{plasmon}}{I_{ZLP}}. \tag{4.1}$$

The ratios of the thickness before (t_{before}) and the thickness after (t_{after}) the laser irradiation

corresponds to the thinning (T) is

$$T = \frac{t_{before}}{t_{after}} = 35.4 \pm 3\%,$$

assuming the same mean free path for electrons before and after the laser treatment in the material. The areas between the dotted line were integrated to estimate the elastically scattered electrons within the ZLP and the plasmon. The error is estimated by changing the integration boundaries a few eV into each direction. This corresponds to the laser treated sample having its thickness reduced by roughly two thirds.

Figure 4.3 b shows the effect of a 9 mW 5 min laser illumination on a SiN QF hybrid sample. The SiN membrane cracked, which is typical for intense laser irradiation. Here, however, the crack is held together by the amorphous carbon membrane attached to the grid. Also signs of degradation and melting of SiN at the edge of the damaged area is visible.

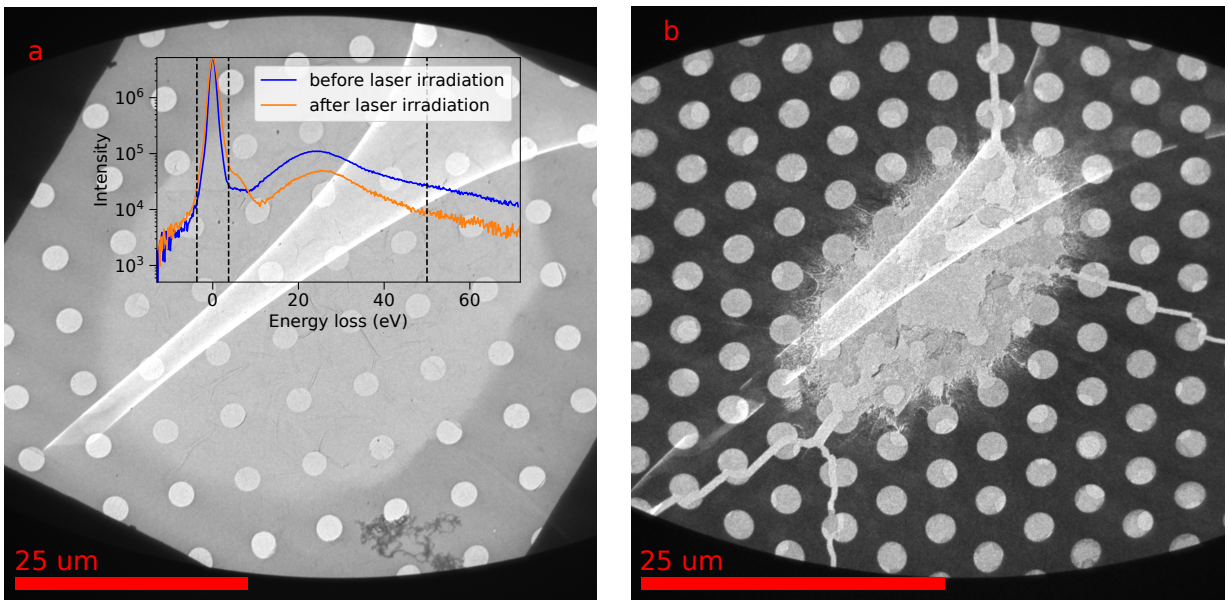

Figure 4.3: **Brightfield TEM images of grids damaged through laser irradiation.** (a) Thinned down amorphous carbon membrane of a Graphenea Quantifoil membrane after a 15 mW 1.7 ms pulse. (b) Cracked SiN grid after 9 mW 5 min illumination. The sample was a hybrid sample so the crack was concealed by the transferred amorphous carbon membrane holding the SiN together.

4.1.3 Recommended parameters

It is hard to provide a simple recipe for cleaning samples of different kinds, however Table 4.1 and 4.2 show parameters for the most common samples that we are using. Low power and long illumination times seem to be the most preferable conditions, considering that high powers usually lead to more damage in TEM grids. We believe this to be caused by the higher temperature gradient within the grid. For the target chamber laser samples can be illuminated indirectly ("upside-down") to reduce damage. This is done by rotating the linear transfer arm holding the puck by 180°. This way the membrane is not directly exposed to the laser but is still heated in the process.

Table 4.1: **Cleaning parameters via the laser at the microscope column.** Unless explicitly stated otherwise the samples are CVD grown.

Grid	Material	Power	Duration	Comment
Quantifoil	exfoliated graphene	15 mW	0.05 ms	
Quantifoil	hBN	5-7 mW	4 - 30 ms	
Quantifoil	graphene	8-18 mW	1-30 ms	
Graphenea	graphene	26 mW	10 ms	
Pelco SiN	hBN	8-11 mW	2-20 ms	cracks start at 9 mW, 10 ms
Pelco SiN	graphene	23 mW	2 ms	cracks start at 9 mW, 10 ms
Silson SiN (SW)	graphene	35 mW	10 ms	
Silson SiN (9W)	graphene	80 mW	6 min	

SW = single window; 9W = nine windows

Table 4.2: **Cleaning parameters for the laser at the target chamber for different samples.** Unless explicitly stated otherwise the samples are CVD graphene.

Grid	Material	Power	Duration	Comment
Quantifoil	ML graphene	1 %	180 s	some areas are too destroyed
Quantifoil	ML graphene	3 %	30 s	some areas are too destroyed
Silson SiN (9W)	ML graphene	27 %	40 min	

ML = monolayer; DL = double layer; SW = single window; 9W = nine windows

4.2 Developing methods for defect-engineering of 2D Materials

As discussed in Section 3.3.2 direct implantation is not an effective method for implanting heavy heteroatoms into graphene. In Refs. [13] and [14] we show that a two-step process utilizing defects to trap adatoms is a reliable method. Defect-creation was attempted using two methods in this work, energetic electrons and low energy ions. One key difference between the two methods is, that while ions create defects everywhere, energetic electrons can be introduced at specific locations.

4.2.1 E-beam induced defects

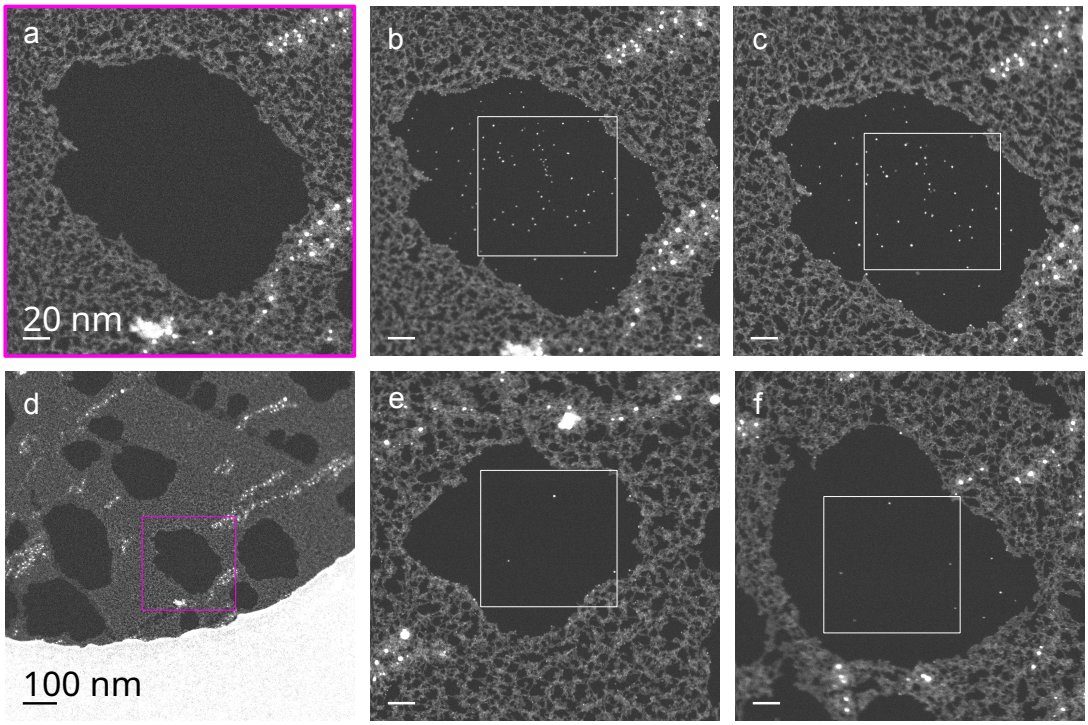

Figure 4.4: **Effect of prior e-beam exposure on cluster growth via PVD.** The area in (a) was exposed to 100 keV electron irradiation for about one hour. Fe was evaporated onto the sample after the irradiation which is shown in (b). In (c) the same hole is shown after laser irradiation/annealing. (d) shows an overview image of the sample where the hole shown in (a)-(c) is marked with a pink rectangle. (e) and (f) show different holes which were not electron irradiated before the Fe evaporation and laser annealing which results in significantly less clusters. All images shown are STEM MAADF images.

Fig. 4.4 shows the influence of e-beam exposure on cluster growth. The clean graphene shown in Fig. 4.4 a was exposed to 100 kV electron irradiation for ca. one hour. Assuming a beam current of 50 ± 5 pA (a slightly lower beam current was measured for 90 and 95 kV for our instrument [133]) using the displacement cross section [65] and assuming the area to be a circle with a radius of ca. 100 nm that would result in ca. 1300 defects in the area or a defect density of about 0.11 ± 0.03 %.

Fig. 4.4 b shows the area after evaporating Fe with an e-beam evaporator (flux 0.69 nA, exposure time 20 s). Within the white rectangle (100×100) nm^2 58 Fe clusters were counted based on the contrast. The sample was exposed to laser irradiation multiple times to test their thermal stability. The number of clusters stabilized at 41 and did not change after the first few pulses (shown in figure 4.4 c). Sample areas that have not been exposed to electron irradiation show between three and five clusters in an equally large area (Fig. 4.4 e and f) after otherwise the same treatment.

4.2.2 Electron-beam-induced deposition (EBID) patterning

The possibility of trapping atoms at well defined anchoring sites (defects) raises the question of what kind of structures can be drawn. Before introducing defects in a specific pattern and filling them we wanted to visualized whether the patterning algorithm can actually be used as described in Section 3.1.7. Due to the low cross section for introducing defects into graphene with 100 keV irradiation and the fact that observing few defects spread out over a large area is challenging the experiments for testing this method directly would take quite a long time. Thus EBID has been used to draw nanometer sized patterns on graphene, which has been done already more than ten years ago by moving the electron beam over the sample [92]. In our group crude patterning was also combined with PVD to draw Au structures [160]. Here the stage is moved to defined the pattern that is drawn with the electron beam.

As discussed, build-up of mobile contamination is triggered by the electron beam and proportional to the exposed dose. The degree of this varies greatly with the grid and sample cleanness. Fig. 4.5 shows different patterns that were drawn using a sample where mobile contamination was pinned down under 60 keV electron irradiation. Whether a pixel is written or not depends not only on the dose but also its microscopic surrounding because the build-up can be enhanced or suppressed depending on the distance from static contamination. The written pixel size $(5 - 10)$ nm using contamination is much larger than the scanned FOV (1 nm).

A side note about the three different patterns shown in Fig. 4.5 can be made about the strength of

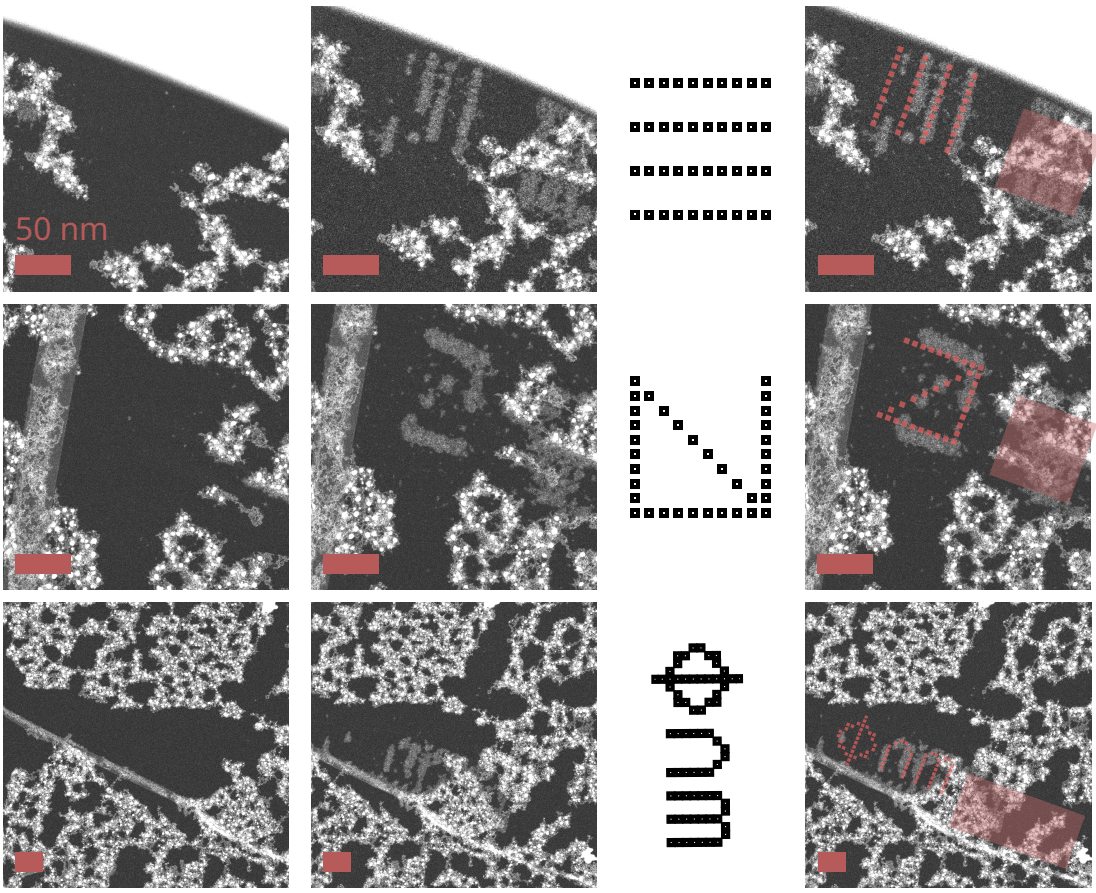

Figure 4.5: **EBID patterns written with the stage movement method.** The first column shows STEM-MAADF images of each respective area before defect patterning. The second column shows the respective areas after defect patterning. The third column shows the pattern that was supposed to be written. Note that the black squares are each 8.5 times the size of the region that was actually irradiated with the electron beam, represented by the white square inside the black square. The fourth column shows the patterns overlaid on the after image (second column). Good overlap is achieved when the pattern is rotated -70° and scaled down to 60%. The FOV in the patterning algorithm was 1 nm, the offset was 12. The imaging parameters were (512 × 512) pixels with a dwell time of 2 µs. All scale bars correspond to 50 nm.

the beam blanker. It was very weak, so for every pattern drawn there appears a "shadow" slightly below it to the right, indicated with the semi-transparent rectangles. This is particularly visible for the first pattern where there are thicker lines than the actual pattern, which corresponds to the "negative" of the pattern that was drawn.

4.2.3 Low-energy ion irradiation using the plasma (deceleration) set-up

The second method for creating defects that was investigated during this work is plasma irradiation within CANVAS. Here the entire sample is exposed to low-energy ions and defects are created everywhere at the same time. In combination with the deceleration set-up this technique can also be used for trapping noble gases between multiple layers.

Measuring the energy distribution

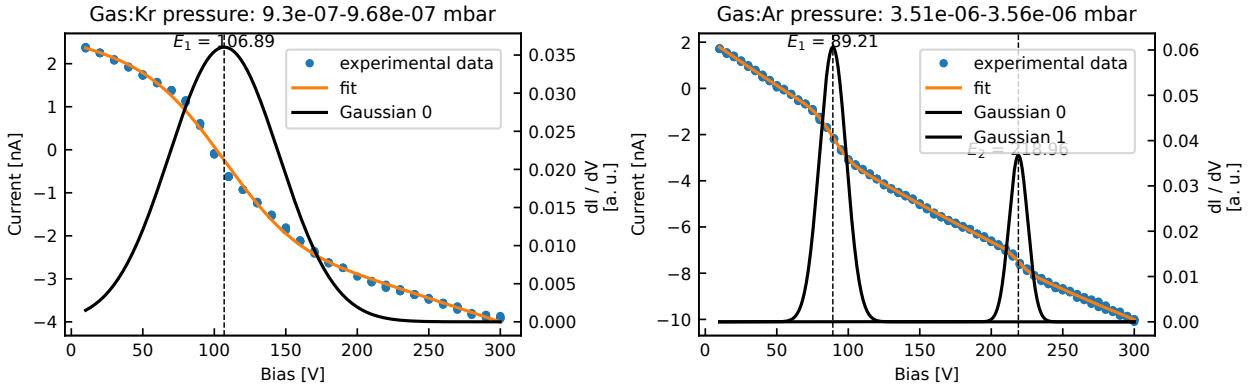

Figure 4.6: **Current-bias plots with fits for determining the beam energy and spread.** Two data sets for current-bias measurements at constant pressure are shown. The experimental data (blue) is fitted with a combination of a second order polynomial and one to three Error functions (orange). The derivative of the error function, a Gaussian distribution, is plotted in black with a separate axis. It corresponds to the beam energy and spread.

For quantifying defect creation and implanting noble gases knowing the exact energy distribution of the ions emitted from the source is necessary. Fig. 4.6 shows two measurements with the fit that was used for estimating the beam energy. First the pressure is stabilized for the duration of the measurement (about 15 min). Then the current at the Faraday cup is measured while the cup is biased from 5 to a few hundred V in steps of 5 or 10 V. At each bias the pressure is measured once and the current is measured five times. The data is collected automatically using a Raspberry Pi that also controls the power supply.

The current as a function of bias decreases with increasing bias (blue dots in Fig. 4.6) due to two effects. The source emits electrons and ions. The positive bias accelerates electrons that would be deflected through the magnet at the aperture such that they are collected, while it also decelerates and repels ions. The difference between the average current at two consequent bias voltages

corresponds to the change of the beam at this energy interval. Thus, the $\frac{dI}{dV}$ curve of the current measurement corresponds to the beam profile. In a similar argument the measured current represents the integral of all ions and electrons that reach the Faraday cup at a certain bias. Assuming a Gaussian shape of the beam energy an error function is fitted for the ionic contributions. As the steep declines of current are attributed to the ionic contribution for each of them one error function is added to the fit. The background from the electrons is fitted with a second order polynomial. We believe the background to result from the resistance of the measurement system as well as electrons that are attracted by the positive potential of the Faraday cup.

Results for analysis

Fig. 4.7 shows the results of the ion energy measurements similar to the ones shown in Fig. 4.6. It is found that the parameter that determines the fluence and energy of the ion beam is the pressure in the reaction chamber, proportional to the measured pressure in the target chamber. The energy of the ions is usually between 50 and 200 eV. For many pressures and noble gases there exist multiple ion energies within the beam. The energy spread of the plasma is surprisingly narrow in many cases (about $10 - 20$ eV). Most measurements were carried out using Ar where we can see, especially for the lower pressure regimes, that the beam energies are very reproducible. At pressures where high changes in current follow minor changes in pressure the energy distribution of beams is in general wider, thus these pressure regions should be avoided for irradiation experiments. We expect all ions to be singly charged due to the low collision rates in the plasma.

Regarding the pressure values the measurement efficiencies for the different elements should still be mentioned. As hot cathode pressure gauges (used here) are calibrated for N the gauge pressure should be divided by the gas correction factors for the different gases. They are 0.3 for Ne, 1.29 for Ar, 1.94 for Kr and 2.87 for Xe.

This method for analysing the ion beam was developed by us. A rather practical but, but very important component for this project was how to record, store and evaluate data sets. While first we did not have a proper metadata format throughout the project it became clear that all metadata needs to be stored with the data itself in order to be able to do analysis in a reasonable way. Thus a significant part of this project was coding. Both, the automatic data recording as well as the semi-automatic data analysis was done using self-developed Python code.

The resulting ion energies show quite significant disagreement to the expectations from the man-

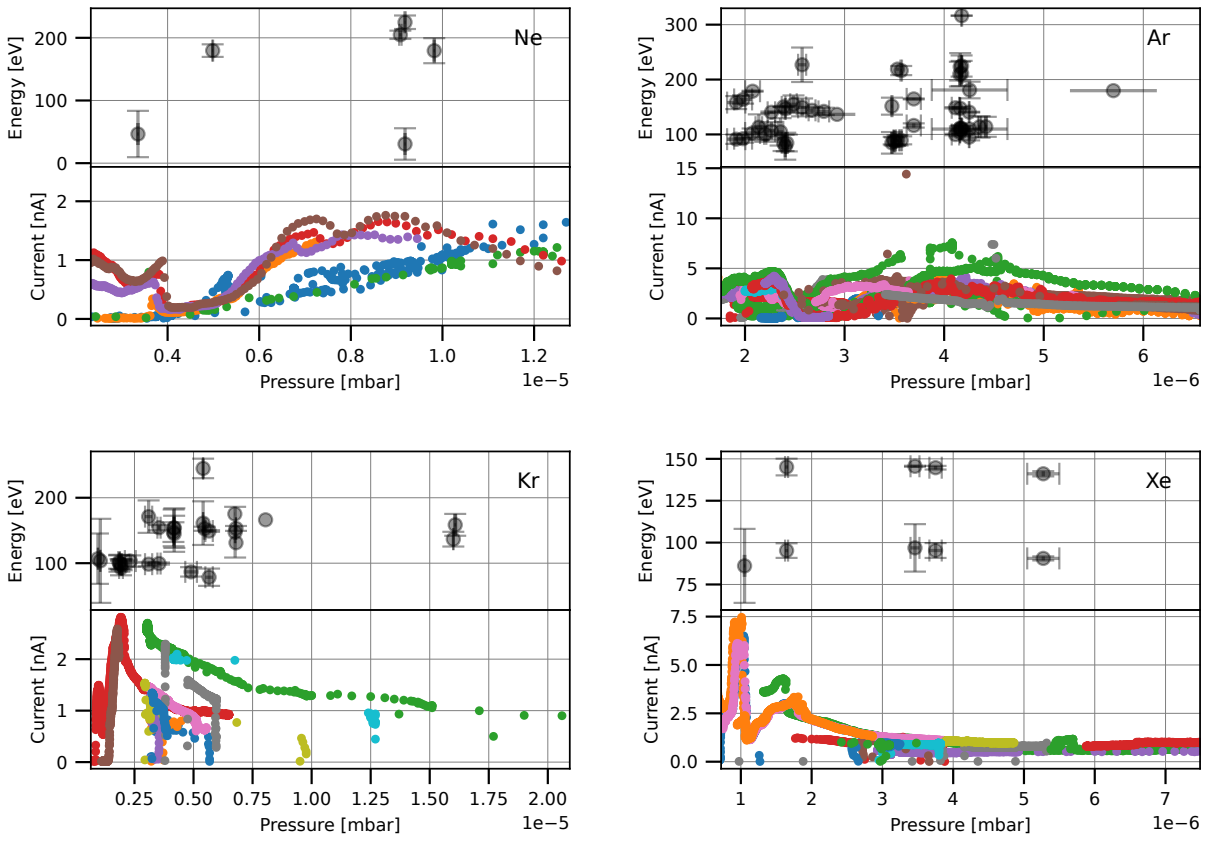

Figure 4.7: **Measured beam energies, spreads and currents as a function of pressure for Ne, Ar, Kr & Xe.** For all measurements shown the magnetron current was 16 mA the anode bias was 0 kV and extractor bias was −0.06 kV. The top of the plots always shows the result of beam shape measurements at different pressures with the uncertainty in the energy being the standard deviation from the Gaussian distribution. The uncertainty in the pressure represents the standard deviation of the pressure recorded during the biasing measurement. The bottom plot shows different current measurements as a function of (non corrected) pressure.

ual of the instrument. It is not obvious why the ions have such a high energy even though they are not accelerated by an anode voltage. One possibility is that as electrons are much lighter, they leave the reaction chamber faster leaving more ions behind which repel each other electrostatically.

4.3 Heteroatom implantation

The first time vacancy assisted implantation was used within our group was using plasma irradiation within the CANVAS to trap Si adatoms existing on samples [116]. The method was later used [13] to implant Au in a two-step process in Helsinki using an ion implanter. Au ions at 200 eV were used to create vacancies. Subsequently Au ions were deposited onto the sample at 25 eV. Within CANVAS the plasma source was used together with PVD for aluminium trapping around the same time [14]. My contributions to the studies [13, 14] can be summarized as helping with the characterization of the ion implanter and the plasma source. The general applicability of this approach was later demonstrated [3] where I conducted experiments and characterisation for the element Fe.

The following text is an adapted version of reference [3] where we report the creation of atomically clean graphene using laser cleaning with uniformly distributed and covalently bound Al, Ti, Fe, Ag and Au single atoms or nanoclusters. Vacancies introduced into atomically clean graphene via low-energy ion irradiation were used as anchoring sites for single atoms and clusters were introduced via PVD for different elements.

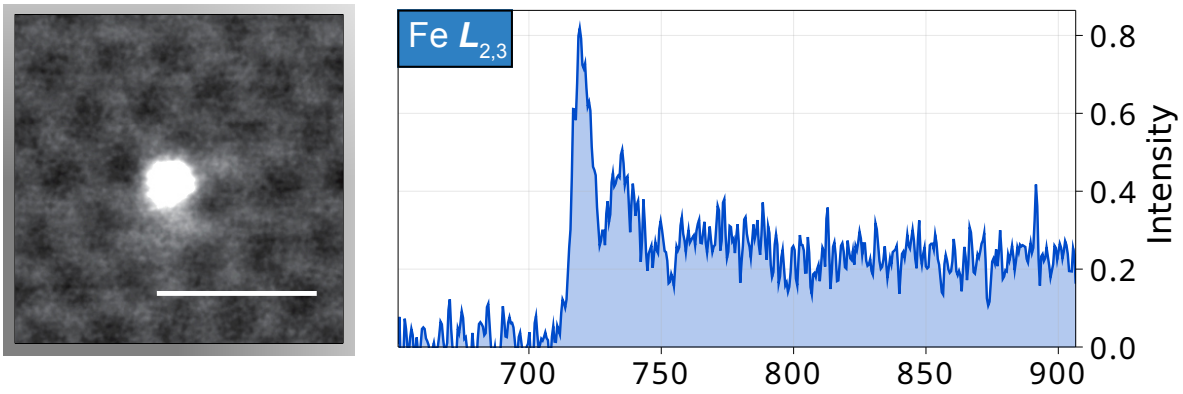

Figure 4.8: **Individual Fe atom implanted in graphene.** STEM-MAADF image of single implanted Fe atom, as well as EELS data confirming the atomic species. From [3] used with permission.

Fig. 4.8 shows an experimental STEM-MAADF images and an EEL spectrum. The EELS data was recorded for the impurity atom shown in the image embedded in graphene. The signal of graphene recorded nearby (adjusted to coincide with the spectrum before the impurity peak) was used as background. The image shows how the atom occupies a divacancy in graphene and the

spectrum clearly identifies the atom as Fe.

The samples used were CVD-grown monolayer graphene transferred to Quantifoil grids. The samples were cleaned using laser illumination with typical parameters described above. After cleaning, vacancies were introduced into graphene via low-energy Ar^+ irradiation as described above (less than 200 eV, which should mostly produce single and double vacancies in graphene [12]). Subsequently, the vacancies were filled with Fe atoms introduced via e-beam evaporation (flux of ca. 0.5 nA for about 180 s). Fig. 4.9 a-c shows an area after defect engineering and Fig. 4.9 d-f after subsequent Fe evaporation. The images show how in an area with defects after Fe evaporation many defects are filled with individual Fe atoms and small clusters. This also agrees with the results previously presented.

With this method the number of heteroatoms sites is controlled via the number of vacancies and thus the dose of the ion irradiation and the size of the clusters with the amount of evaporated material. Many impurity atoms, however, are not the desired element but silicon, a typical impurity in graphene [114, 161] that is known to occupy vacancies [116]. Some heteroatoms will also be filled with C [116] or might be replaced during imaging [13, 19, 150].

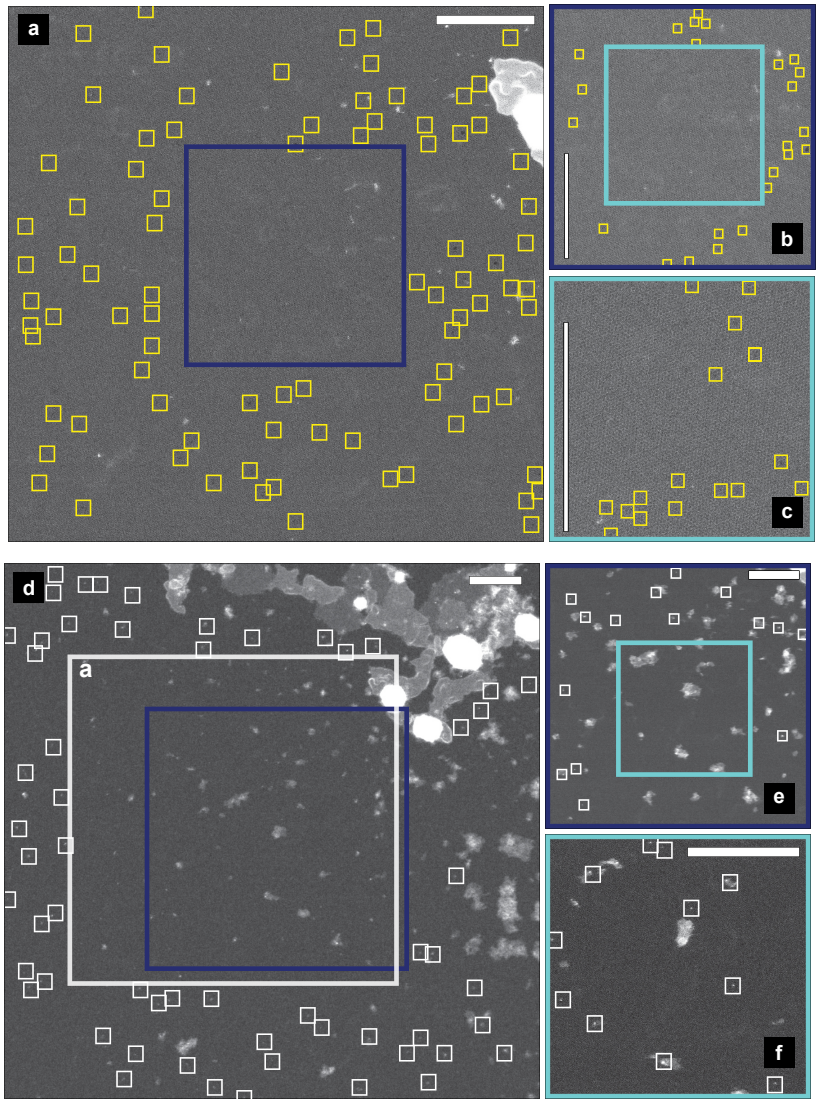

Figure 4.9: **Iron single-atom implantation.** (a-c) STEM-MAADF zoom sequence after defect-engineering. The blue colored squares show the location of the following image. (d-f) STEM-MAADF zoom sequence of the same area after Fe evaporation. The blue colored squares show the location of the following image, whereas the large white square in (d) shows the location where the image shown in panel (a) was recorded before the evaporation. The images were recorded from the smallest to the largest field of view. As can be seen comparing panel (f) to panel (e) and panel (e) to panel (d), mobile contamination has been pinned down to the single-atom impurity sites during imaging. Most locations with small light gray features correspond to locations of single-atom impurities. Iron was evaporated with an ebeam evaporator onto defect-engineered graphene (ca. 3 min, flux of ca. 0.55 nA). Small white squares highlight impurity atoms and yellow ones vacancies (Areas inside the squares are not marked). Instead, markings for those areas are shown always in the smaller field of view image. The scale bars are 15 nm. From [3] used with permission.

4.4 Defects in hBN

This text is an adapted version of [2] which is currently still in preparation.

Due to the interesting properties of point defects in hBN as quantum emitters discussed in Section 2.1.4 the creation of such defects under low energy ion irradiation was studied here. A suspended monolayer hBN sample on a hybrid Quantifoil SiN grids was produced as described in the materials section. The sample is shown in Fig. 4.10 a. Suspended hBN can be found where the holes of the Quantifoil and the SiN overlap, shown in 4.10 b. This hybrid grid allows a polymer-free transfer of hBN onto the final grid, which is mechanically robust and allows sample cleaning with a laser in vacuum.

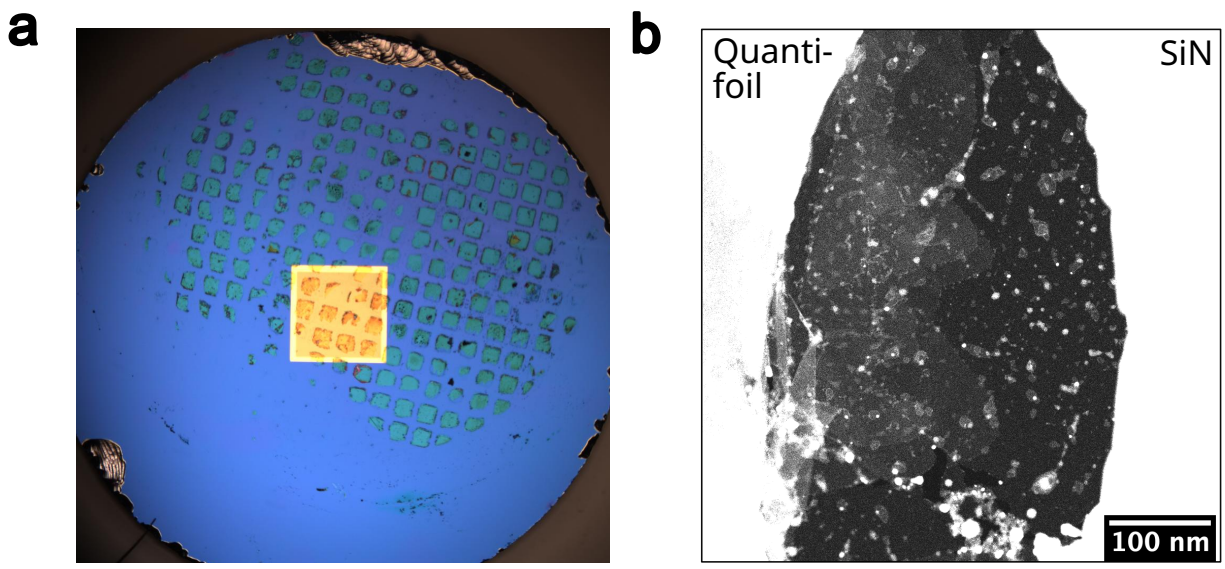

Figure 4.10: **Overview of the sample.** (a) Light microscopy image of the sample after transfer. The blue area corresponds to the Si grid, the light blue squares to Quantifoil. The yellow square is the perforated SiN window where the suspended sample can be found when holes in SiN and the Quantifoil overlap. (b) STEM-MAADF image of a suspended sample area. The dark contrast is clean suspended hBN with the brighter areas correspond to fewlayer hBN (continuous areas on the left-hand side) There are also small contaminated areas throughout the sample. The white area on the left corresponds to Quantifoil and the white area on the right to SiN.

After insertion into the CANVAS as described in the methods the sample is surveyed via STEM MAADF imaging to find a location with good coverage and reasonable surface cleanliness. A 9 mW 2 ms laser pulse is used to remove most of the remaining contamination (see Sections 3.2.1 and 3.4.1). An example large scale STEM-MAADF image of a cleaned sample is shown in Fig. 4.10 b.

Automated atomic-resolution STEM-MAADF imaging as described in Section 3.1.6 is carried out at 60 kV to estimate the intrinsic defect concentration and distribution. During the automatic image acquisition minor adjustments of the electron energy and the correction of astigmatism and coma were done manually. The images were recorded with a (calibrated [137]) field of view of 4.2×4.2 nm^2, a pixel dwell time of 16 µs and 512×512 pixels, the chosen offset was 1.

In total, 16500 nm^2 of hBN were imaged in the area shown in Fig. 4.10, out of which ca. 68% were contamination-free and were imaged with a resolution that allows atomic structural analysis. The images are analysed automatically with a convolutional neural network using a pipeline similar to those described in Refs. [162, 12]. In short, the neural network first separates image areas to either contamination or lattice. Next, each lattice site is assigned an intensity value at different values of Gaussian blurring. These values are provided to a classifier that determines whether the site contains an atom or a vacancy. The process is illustrated in Fig. 4.11. In total, 335 defects were identified in this data set leading to a defect concentration of ca. 0.03 nm^{-2} with ca. 55% boron and ca. 8% nitrogen single vacancies.

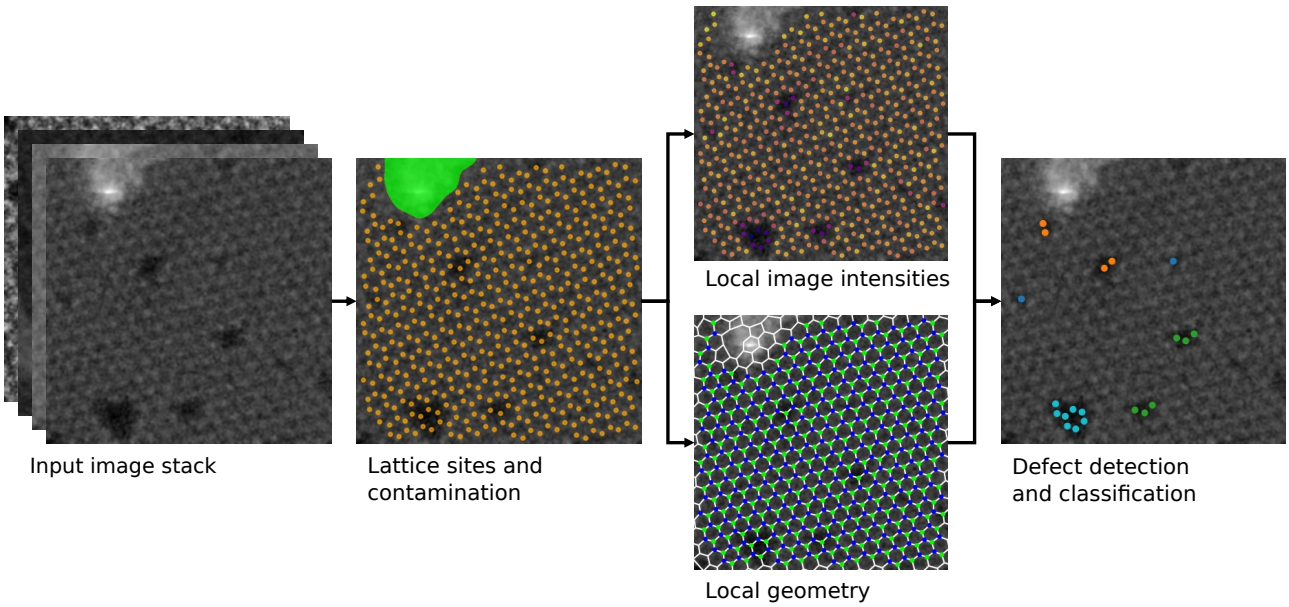

Figure 4.11: **Automated analysis pipeline.** The analysis pipeline operates on a stack of images. Each image is analyzed with a convolutional neural network to find the (possible) contamination and each of the hBN lattice sites. For each lattice site, local intensity features are extracted, which are used to classify whether the site contains an atom or a vacancy. In addition, the geometric relationship between the lattice sites is used for finding neighboring lattice sites and separating the boron and nitrogen sublattices. Finally, the defect size and type is determined by counting connected vacancies.

It is worth pointing out, that electron irradiation during imaging is known to introduce defects into hBN [163, 164, 70] even under ultra-high vacuum [31]. Taking the imaging parameters, the flyback time at the end of each scan line (120 μs) and half of the time to move the stage from one position to the next (0.5 × 2 s), the electron dose per frame is $(3.6 \pm 0.14) \times 10^5$ electrons Å^{-2} using a current of 19.4 ± 0.6 pA [133]. Since the density of hBN is ca. 36.8 atoms nm^{-2}, based on the displacement cross section [31], we estimate that ca. 0.046 ± 0.005 defects are created per image (or 0.00264 ± 0.0003 per nm^2, of which 0.0016 ± 0.0003 are boron and 0.0011 ± 0.0005 nitrogen). Therefore, ca. 29.7 ± 2.8 (out of 335) defects have been created during imaging. Hence, ca. 90% of the defects must be intrinsic to the sample and arise from growth or sample fabrication, leading to an intrinsic defect concentration of ca. 0.027 nm^{-2}.

Next, the sample was transported in vacuum to a chamber containing a plasma generator where low-energy Ar^+ (< 200 eV) ion irradiation is used to create defects [12]. The pressure of the chamber was kept approximately constant at ca. 3.5×10^{-6} mbar, but variations ($\pm 0.3 \times 10^6$ mbar) from this could not be entirely avoided. The irradiation time was ca. 150 s. The irradiation is carried out at room temperature, similar to all other experiments except for sample cleaning in this study. This yields an ion beam consisting of two peaks at 89 ± 10 eV and 228 ± 11 eV with the lower-energy peak contributing ca. 2/3 of the ions. We have no satisfying explanation for how these two peaks arise. One possibility would be singly and doubly charged ions, however the energies do not match up so we can not be sure. The total current was calculated by summing up the ions contributing to each of these distributions. From the ion current and the irradiation time, we estimate the total dose at the sample to be 0.10 ± 0.04 ions per nm^2.

After ion irradiation, the sample was again automatically imaged to estimate the post-irradiation defect density and distribution at another sample position. A comparison between the intrinsic and irradiation-induced defect distributions is shown in Fig. 4.12 a and b. Now, a total area of ca. 14, 500 nm^2 was imaged with ca. 50% of the imaged area that could be used for the analysis (clean and sufficient resolution). In total, 2169 defects were identified leading to a defect concentration of ca. 0.30 nm^{-2}, i.e., close to ten times higher than before the irradiation. Similar to before 19.1 ± 1.9 (out of 2169) defects can be attributed to the electron beam. The amount of irradiation-induced defects is thus ca. 0.27 nm^{-2}. It is worth noting that the defect density is also higher than the estimated total irradiation dose (by a factor of nearly three). This most likely reveals the inherent uncertainty in accurately estimating the current of the plasma source by measurements carried out separately from the irradiation experiment.

The defect density is low enough so that the vast majority of the ions have impinged on pristine defect-free hBN. After the irradiation, ca. 55.7 % of defects are boron and 11.5 % nitrogen single vacancies. Further 14.4 % are double vacancies and the rest (18.4 %) more complex vacancy defects. The spatial distributions for V_B and V_N as well as all other defects are shown in Fig. 4.12 c. The grid-like pattern of the defect locations arises from the images recorded in discrete non-overlapping parts of the sample and the larger defect-free areas have been obscured by surface contamination. Overall, the spatial distribution shows that the defects have been created on a random pattern uniformly on the sample. Example STEM-MAADF images of the most typical defects are shown in Fig. 4.13.

The results are in clear contradiction with the theoretical studies based on analytical-potential molecular dynamics simulations, where it was found, depending on which potential was used, either that low-energy Ar irradiation should lead to about 17 % single vacancies of B and N [32] per impinging ion or that the probability would be between 3 – 6 % for B and 9 – 10 % for N [33] for energies similar to the ones we determined experimentally. On the experimental side, since we don't have an accurate measurement of the ion current during the irradiation, we don't precisely know what the probability for creating each type of single vacancy is.

However, since we observe about three times as many defects as we estimate ions to have irradiated the sample, it seems a safe assumption that the probability must be closer to one than the simulations suggest. As already mentioned for the Fe implantation, carbon atoms from the ubiquitous contamination are known to migrate on the surface of 2D materials and fill vacancies [116], especially at elevated temperatures [165]. Due to the similar atomic number (and therefore contrast [130]) of C as that of B and N, it is possible that our characterization has missed some vacancies that have been subsequently filled with carbon. Also vacancies filled with Si, discussed in the previous chapter, are ignored in the analysis. However, here the same argument applies as above: since the defect concentration is higher than expected based on the estimated ion current, it seems unlikely that such a large number of N vacancies would have been filled with carbon atoms that the experimental results would agree with the simulation prediction. Instead, the most likely explanation seems to be that analytical molecular dynamics is not a sufficiently accurate method to describe low-energy ion irradiation of hBN, which could be related to the partially ionic bonding.

Overall, this discrepancy highlights that more experimental and computational work is required to obtain a comprehensive understanding of the capabilities of this method for defect-specific

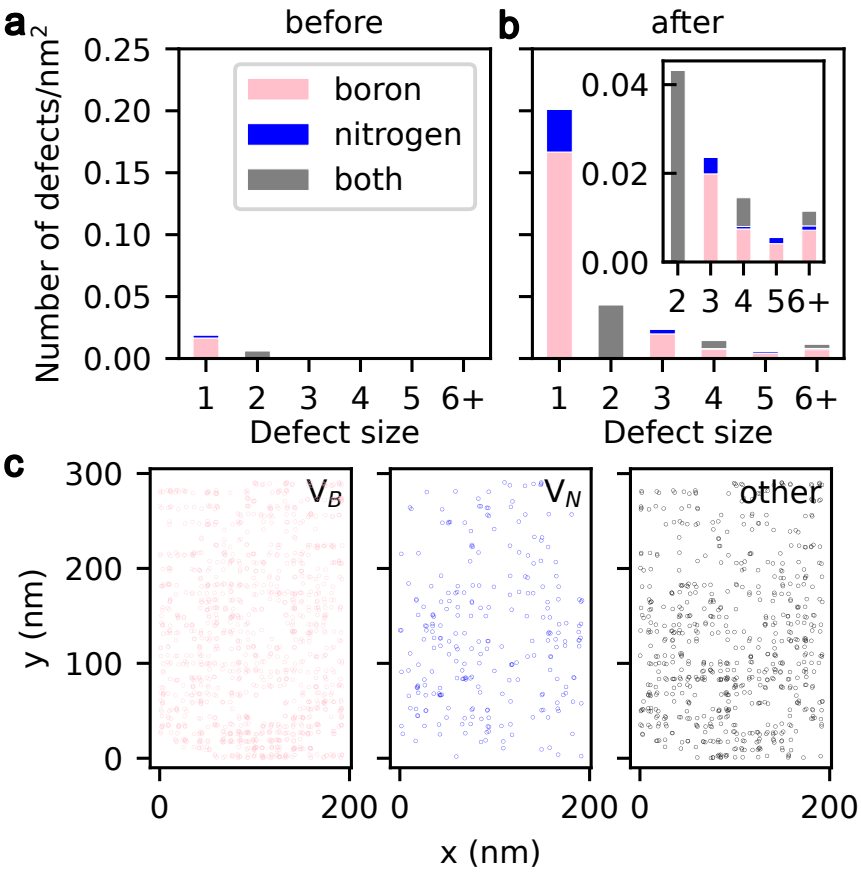

Figure 4.12: **Defect concentration and distribution.** (a) Intrinsic defect concentration as a function of the defect size (number of missing atoms). (b) Post-irradation defect concentration as a function of the defect size (number of missing atoms). The inset shows a magnified view of the defect concentration for defects with at least two missing atoms. (c) Spatial distribution of boron and nitrogen single vacancies (V_B and V_N, respectively) and all other defects.

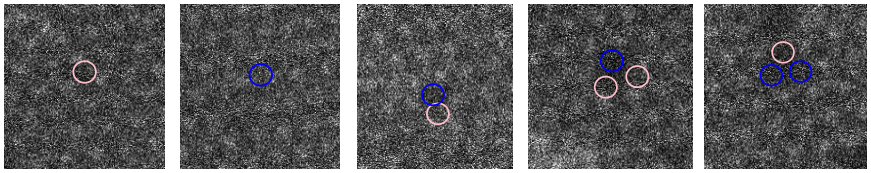

Figure 4.13: **Example STEM-MAADF images of the most typical defects.** Pink circles mark the positions of missing B and blue circles missing N atoms. From left to right: V_B, V_N, double vacancy, triple vacancy with one missing N and two missing N, and triple vacancy with one missing B and two missing N. All images have a field of view of 2 nm.

engineering of hBN. A control experiment still needs to be carried out for this study as only one image stack at one position before and after the irradiation were recorded for one sample so, in principle, all measured effects could be due to inhomogeneity of the sample quality.

4.5 Trapping noble gases in the graphene and hBN sandwich

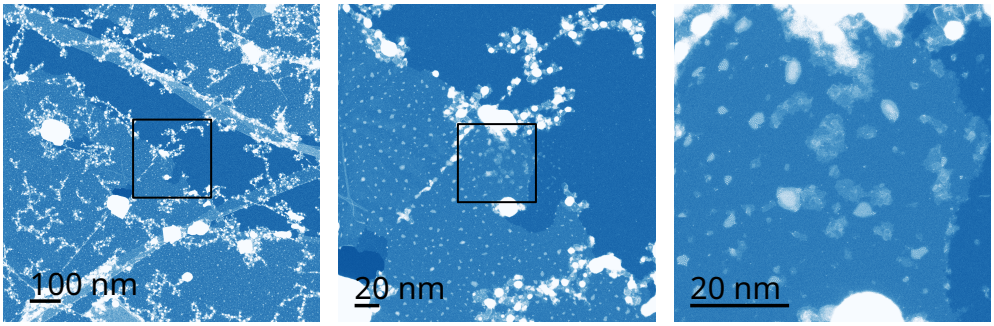

Figure 4.14: **STEM-MAADF zoom series of Xe implanted Gr.** The effect of ultra-low energy Xe^+ irradiation on mono and double layer regions is shown. While in double layer regions clusters and small bubbles form, in monolayer region only defects are created. The images were taken from smallest to largest FOV.

Different irradiation experiments on double and multi-layer graphene samples were carried out. The energy for an implantation using the plasma source and deceleration set-up within CANVAS is set by choosing a pressure, stabilizing the beam and then either taking an old reference measurement for the energy or measuring the beam shape directly. The puck is then biased to decelerate the ions and reduce their energy as desired. The remaining energy is the difference between the energy within the primary beam and the sample bias. Singly charged Ar, Kr and Xe ions were implanted into the vdW gap of graphene within CANVAS. Single charged Kr and Xe was additionally implanted within KIIA at Helsinki University.

In this work mostly Kr and Xe are shown as, due to their significantly higher atomic number Z, their scattering contrast is much higher and thus they show bright contrast in ADF STEM images [130]. Ar was found only in bubbles, similar as shown in Fig. 4.2. The energies at which successful irradiations were carried out are noted in Table 4.3. No systematic study on the implantation efficiency was conducted.

Comparing the results for successful implantations with the values for bulk graphite 3.1 in table 3.1 it is notable, that implantation was achieved at lower energies for 2D materials. Our results are in agreement with 25 eV for He, Ne and Ar [109], however, they are somewhat lower than the results for hBN on Rh(111) (60 eV) [107] and another study where Kr^+ was implanted below the first layer of graphite (30 – 120 eV) [108]. The experimental results are also considerably lower than the simulated lower bound for Xe implantation into bilayer graphene of 70 eV [166].

Table 4.3: **Confirmed successful implantations into graphene.** 60 eV for Kr as well as 55 and 65 eV for Xe were recorded with the ion implanter KIIA in Helsinki. The rest of the energy ranges were recorded with the deceleration set-up within CANVAS.

Element	Energy [eV]
Ar	20 – 30
Kr	25 – 60
Xe	15 – 65

However, a part of this difference could be attributed to the uncertainties for the ion energies as implantation within CANVAS is not an extremely well defined process (small changes in the hard-to-control pressure already causing significant changes in ion energies).

Implantation into hBN multi- and double layers works similar for graphene. Fig. 4.15 shows Kr-implanted few-layer hBN. The imaged area was multi-layered hBN. The irradiation was conducted with a beam consisting of 25 eV and 100 eV Kr^+. After the irradiation there were bubbles as can be seen in Fig. 4.15.

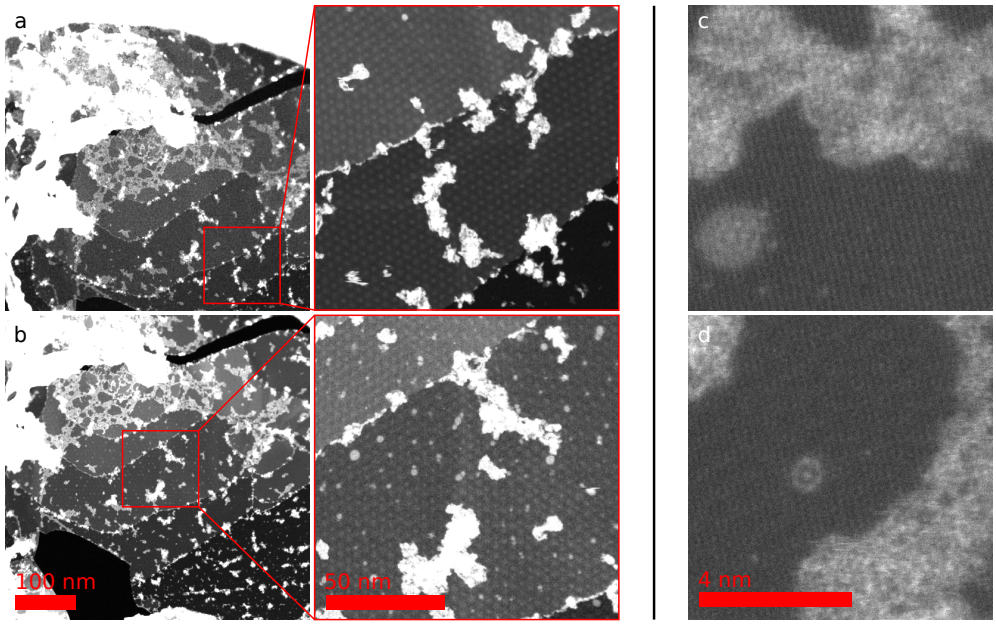

Figure 4.15: **STEM-MAADF images of Kr trapped in multi-layered hBN.** (a) and (b) show a multi-layer hBN sample before (a) and after (b) irradiation. A beam with an ion energy of with 25 eV and 100 eV Kr^+ was used. Small bubbles are distributed all over the multi-layer region. (c) and (d) show small implanted Kr clusters. The cluster in (d) probably consists of seven Kr atoms.

Kr clusters within a hBN double layer are shown in Fig. 4.15 c and d. The atomic positions are

more difficult to make out than in their counterparts trapped between graphene.

4.6 2D noble gas clusters

In this chapter the structure and properties of the created 2D few-atom noble gas clusters between two layers of graphene as reported in Ref. [1] will be explained. The text in this chapter is an adapted version of this publication.

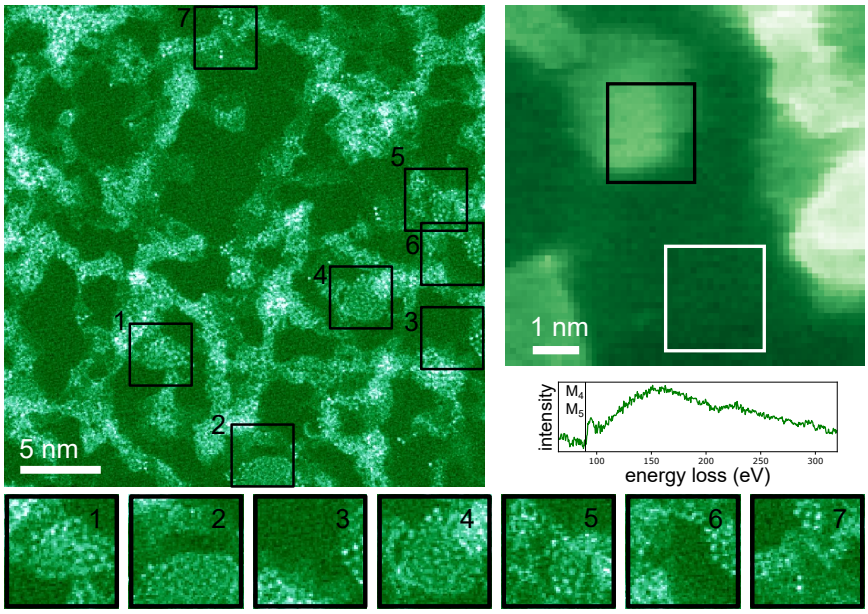

Figure 4.16: **STEM-MAADF overview image of an area containing several Kr clusters (some of which are highlighted by numbered rectangles with magnified versions shown at the bottom) and spectral map.** The EELS map was recorded over a cluster with approximately 50 – 70 atoms, shown on the right side of Fig. 4.28. The contrast here corresponds to the integrated spectrum for each pixel. The signal from the Kr $M_{4,5}$ core loss peak arises from the area spatially located at the cluster, as can be seen from the spectrum obtained by subtracting the graphene signal (from within the area marked by the white rectangle) from the signal corresponding to the area marked by the black rectangle (the spectra were normalised to the values before the peak onset at 89 eV). From [1] used with permission. Copyright ©2024, The Author(s), under exclusive licence to Springer Nature Limited.

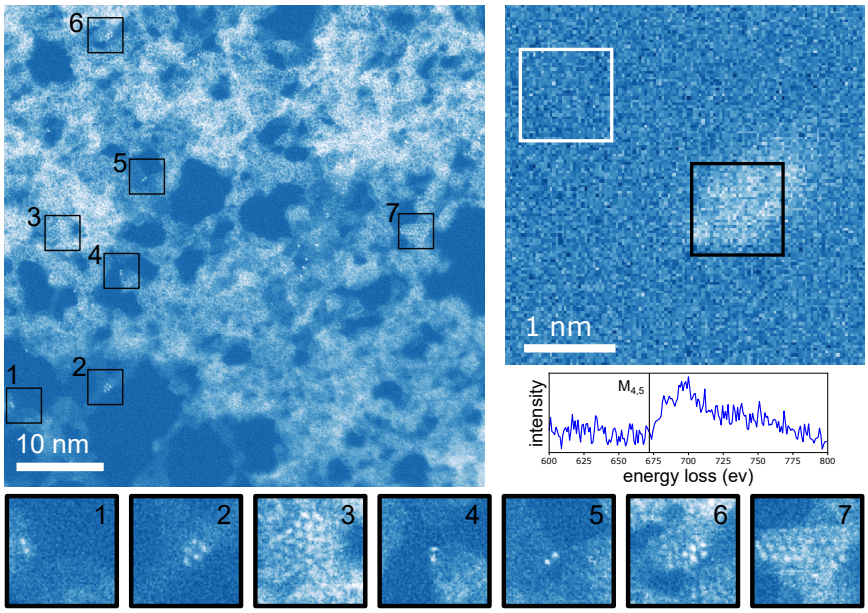

Figure 4.17: **STEM-MAADF overview image of an area containing several Xe clusters (some of which are highlighted by numbered rectangles with magnified versions shown at the bottom) and spectral map.** The EELS map was recorded over a Xe_6 cluster (same cluster as Xe_6 in Fig. 4.18). The contrast here corresponds to the integrated spectrum for each pixel. The Xe M_4 and M_5 core loss peaks arise from the area spatially located at the cluster, as can be seen from the spectrum obtained by subtracting the graphene signal (from within the area marked with a white rectangle) from the signal corresponding to the area marked by the black rectangle (the spectra were normalized to the values before the peak onset at 672 eV). Two very bright pixels, possibly caused by cosmic rays hitting the detector, were replaced by their average surrounding. From [1] used with permission. Copyright ©2024, The Author(s), under exclusive licence to Springer Nature Limited.

Here, we create 2D few-atom noble gas clusters by implanting Kr and Xe between suspended graphene sheets using ultralow-energy ion irradiation, and image them at room temperature using atomic-resolution STEM, complemented by EELS for confirming the chemical identity of the atoms. Kr and Xe implantation for the images shown here was done in Helsinki using the KIIA implanter, unless noted otherwise. Successful implantation between two graphene layers was achieved at 60 eV for Kr, and 55 eV and 65 eV for Xe. To reduce sample contamination during the implantation process, some of the samples were baked in air for 1 h at 300°C and inserted warm into the irradiation setup. One additional sample was implanted using 30-eV Xe ions at the University of Vienna using a plasma source within the vacuum system [10]. The samples were additionally cleaned before imaging with a laser (20 mW, 50 µs pulse). The experiments were conducted with both, exfoliated bilayer graphene and FLG (all shown Xe data) as well as

stacked CVD-graphene (all shown Kr data). Larger scale images of implanted samples with many clearly visible clusters are shown in Fig. 4.16 for Kr and Fig. 4.17 for Xe along with the recorded spectroscopic signatures confirming the elemental identification as Kr and Xe, respectively.

4.6.1 Shape of clusters

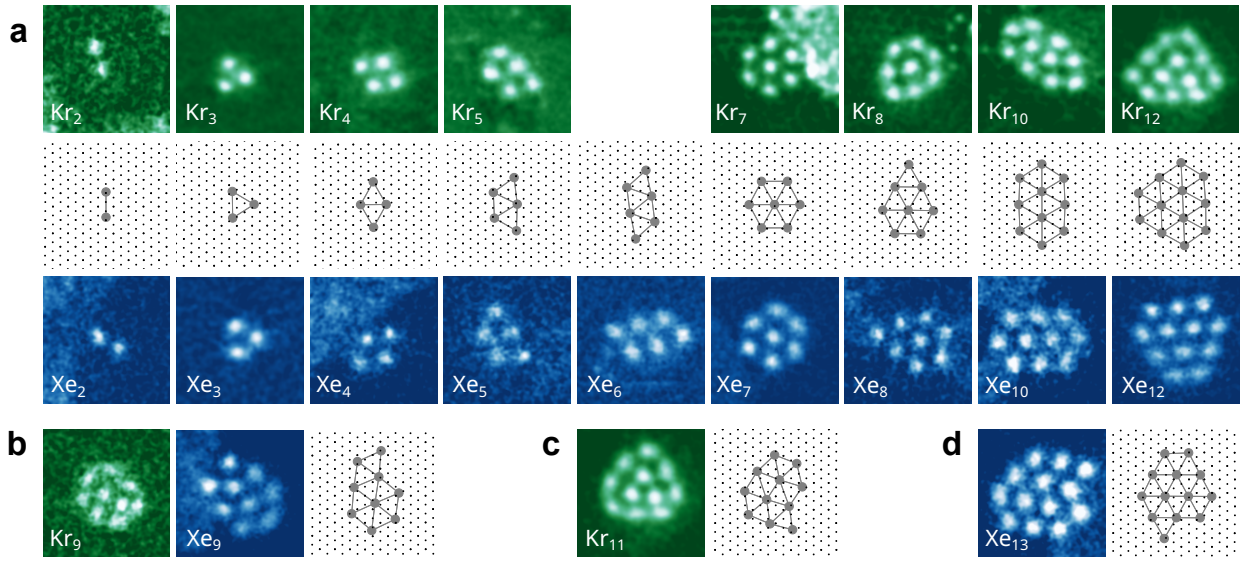

Figure 4.18: **Structure of small clusters.** (a) Filtered STEM-ADF images (see Methods) of Kr (top row) and Xe (bottom row) clusters with $N \in [2, 12]$, including all cases where the experimentally observed structure corresponds to that with the lowest energy according to simulations. The corresponding simulated structures after energy optimization are shown in the middle row for Xe (Kr has the same structure, see Fig. 4.20 for all simulated structures). Carbon atoms are shown with small gray dots, and Xe atoms with large dots connected with lines. (b) Example filtered STEM-ADF images of nine-atom Kr and Xe clusters along with the simulated lowest-energy configuration for Kr. (c) Example filtered STEM-ADF image of a eleven-atom Kr cluster along with the simulated lowest-energy configuration for Kr. (d) Example filtered STEM-ADF image of a thirteen-atom Xe cluster and the corresponding lowest-energy structure for Xe. All images have a size of 2×2 nm^2. From [1] used with permission. Copyright ©2024, The Author(s), under exclusive licence to Springer Nature Limited.

Clusters with $N_{\mathrm{Kr}} \in [2, 12]$ and $N_{\mathrm{Xe}} \in [2, 13]$ atoms are shown in Fig. 4.18 a-d along with the simulated energy-optimized structures[1]. All clusters appear flat, and assume a hexagonal close-packed structure. The same cluster shapes are found both for Xe as well as Kr, and in samples

[1]Simulations were carried out by Harriet Åhlgren.

using both exfoliated graphene and graphene grown via CVD. Therefore, there is no plausible way that the clusters could contain any other element that remains invisible in our microscopy images.

The hexagonal close-packed structure minimizes the number of lower-coordinated atoms while at the same time maximizing the number of nearest neighbors within the cluster (see also Fig. 4.19). Up to $N < 9$, all clusters in the experiment are found also in the optimal structure as predicted by the simulations, although in some cases also other structures with the same N are observed (see Fig. 4.20). Most notably, the Kr_9 cluster also appears in a shape where the atoms are arranged along two lines. In this unexpected Kr_9 structure the number of van der Waals bonds with approximately the nearest neighbor distance (d_{nn}) is only 14 (in one case even 13), whereas in the ideal structure it is 17. In addition to this specific case of Kr_9, the atoms in the outer rim of clusters with $N \geq 9$ appear to have less defined positions (also seen in Fig. 4.18 b & c). These deviations from the ideal structure may arise from factors other than the interaction between the noble gas atoms (for example from deformations in the encapsulating graphene structure, as will be discussed below). We also point out that one Kr_{10} configuration, as well as $Kr_{11,12}$ all show the same cluster with occasional detachment and attachment of one or two atoms (the image series is shown in Fig. 4.21). In many cases, we also observe shape changes both in the simulations (Fig. 4.22), as well as in the experimental images (Fig. 4.20). Although we did not find Kr_6, Xe_{11} or Kr_{13} within our images of small crystals, there is no reason to assume that they would be less stable than the clusters shown in Fig. 4.18.

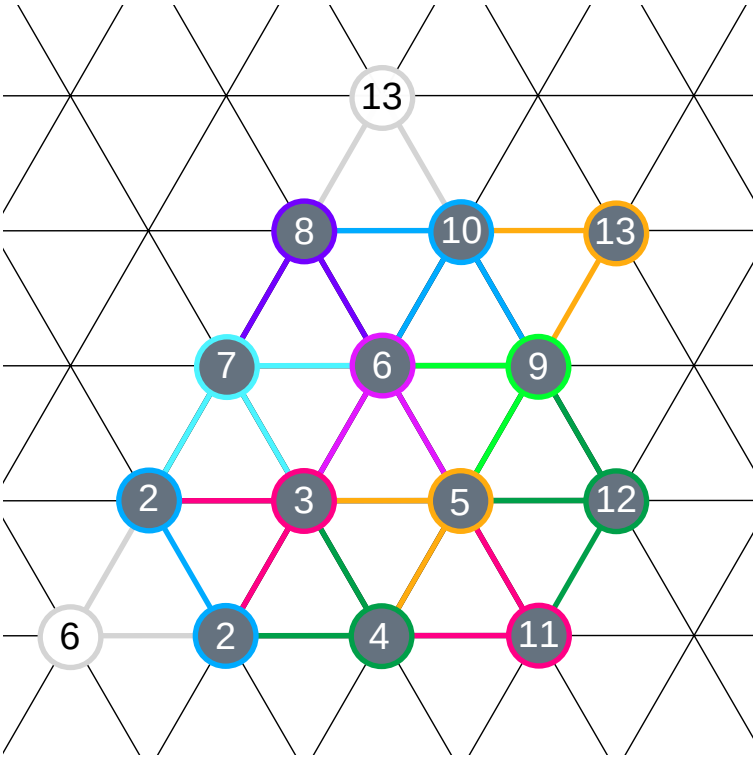

Figure 4.19: **Schematic presentation of the observed atomic structures.** The numbers indicate the size of the cluster (positions marked with $i \leq N$ constitute the cluster with N atoms). For each added atom, the bonds with the same color as the circle are new compared to the cluster with one less atom. The position shown with gray outline and black number 6 corresponds to the position of the sixth atom in Xe_6 in the observed cluster, whereas the colored circle with white 6 is the position of the sixth atom in all clusters with $N > 6$. In contrast, the colored circle with white 13 corresponds to the observed structure of Xe_{13}, whereas the gray circle with black 13 would lead to a more symmetric structure but with the same number of nearest neighbor interactions. From [1] used with permission.

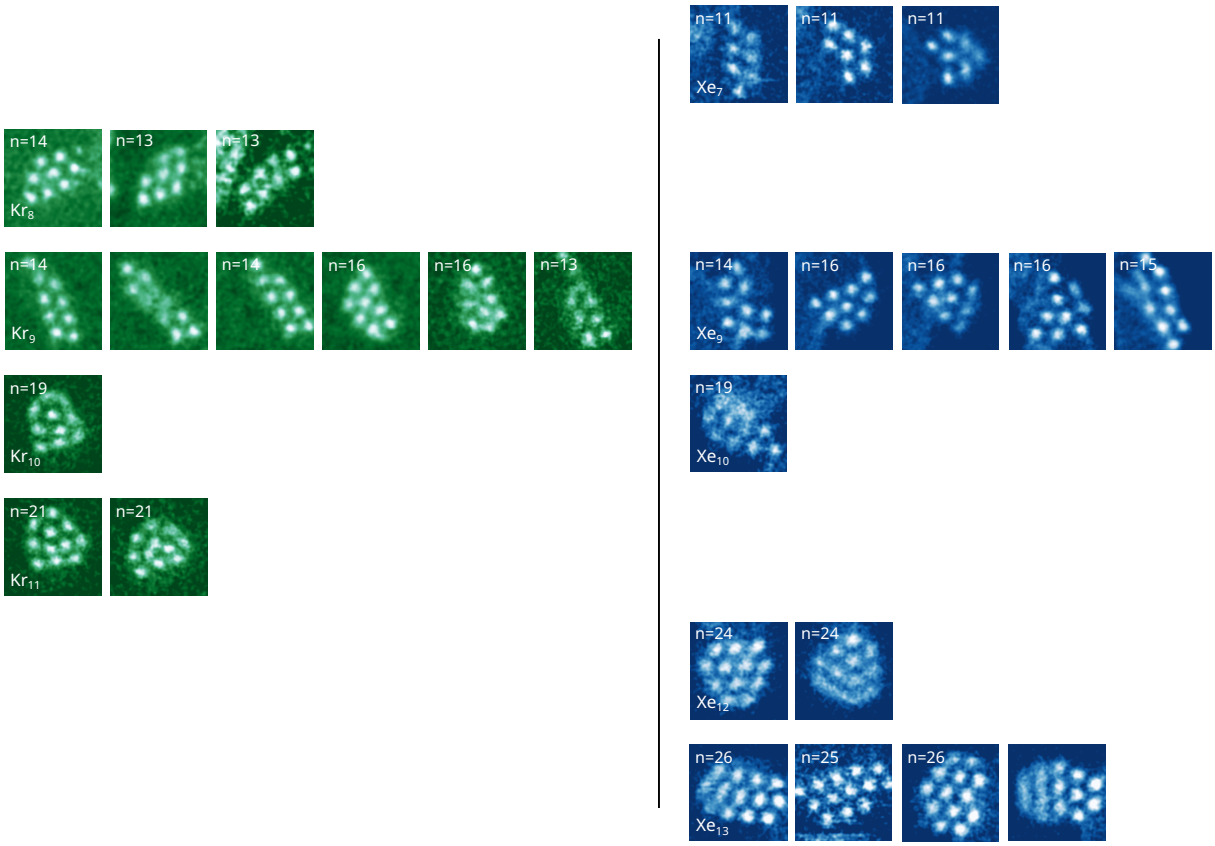

Figure 4.20: **Filtered STEM-ADF images (see Section 3.1.8) of small Kr and Xe clusters displaying all additionally observed shapes in our experiments.** All images have an area of 2×2 nm^2. Left are Kr and right are Xe clusters. The overlaid values for n show the number of nearest-neighbor pairs for each configuration. From [1] used with permission. Copyright ©2024, The Author(s), under exclusive licence to Springer Nature Limited.

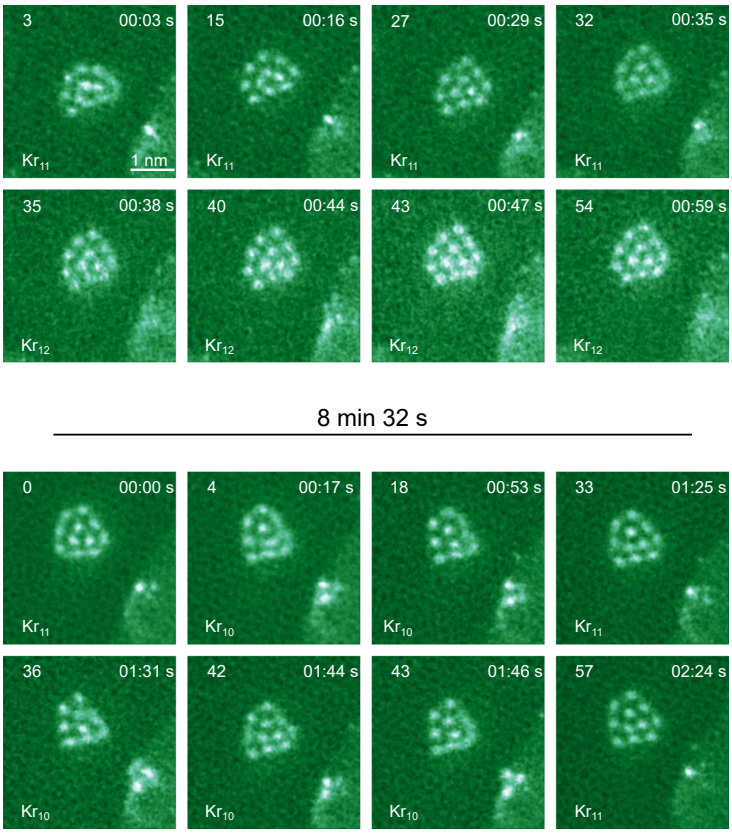

Figure 4.21: **Filtered STEM-HAADF images (see Section 3.1.8) of a Kr cluster changing size over time.** The labels correspond to the frame numbers within the image sequence and the corresponding time. The second images series was recorded 8 min 32 s after the first frame of the first sequence. From [1] used with permission. Copyright ©2024, The Author(s), under exclusive licence to Springer Nature Limited.

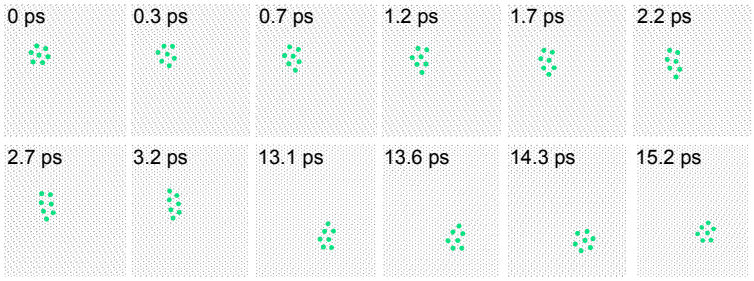

Figure 4.22: **Shapes of a simulated cluster.** Snapshots of a room temperature molecular dynamics simulation showing configuration changes for a Kr_7 cluster. C atoms are shown in grey. Kr atoms are shown in green. From [1] used with permission. Copyright ©2024, The Author(s), under exclusive licence to Springer Nature Limited.

4.6.2 Quantitative measurements, pressure, forces and simulations

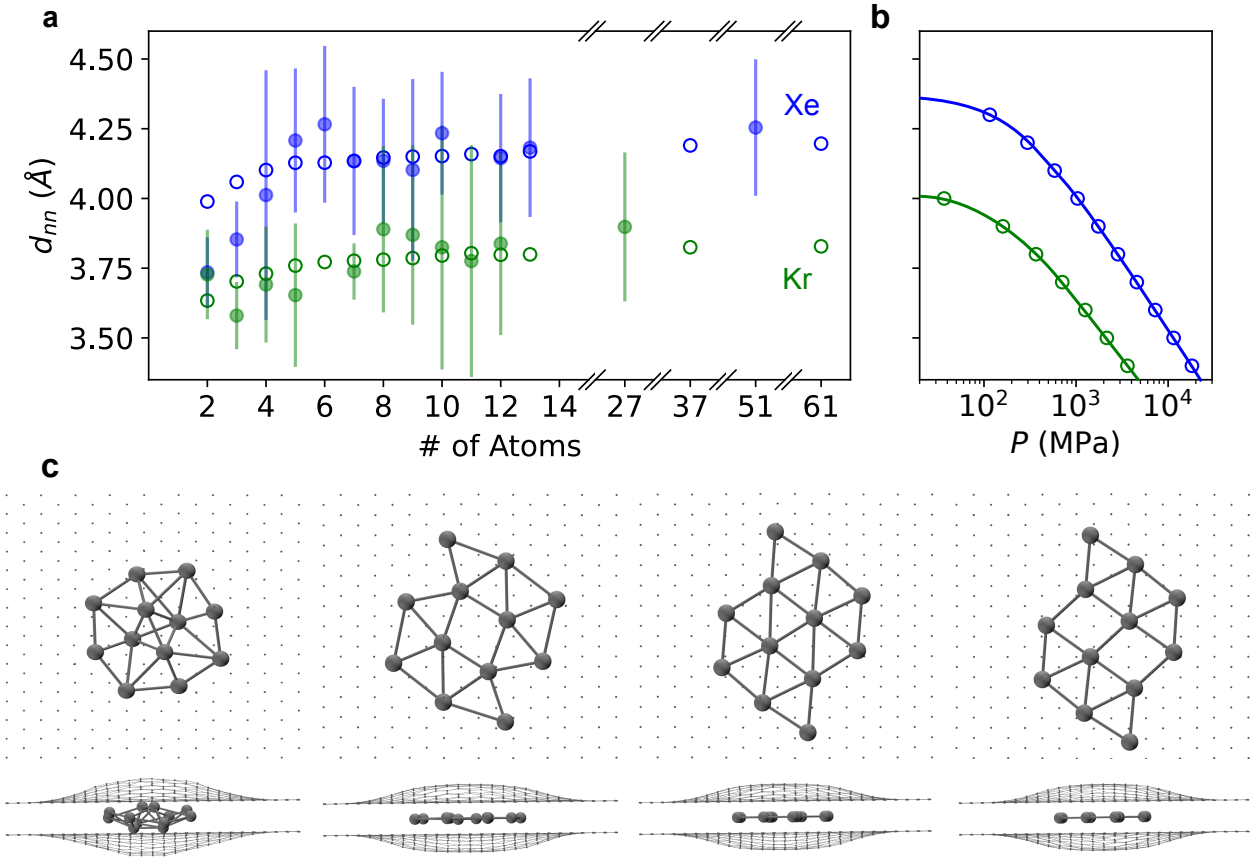

Figure 4.23: **Interatomic distances and 3D to 2D transformation.** (a) Measured interatomic distances d_{nn} (full circles) in the experimentally observed Kr (green) and Xe (blue) clusters as a function of the cluster size. Each data point is averaged over all images where the structure was clearly visible, taking always the mean value per image. The errorbars show the standard deviation of the data. Open symbols correspond to the simulation results. (b) Relationship between the pressure (plotted on logarithmic scale) exerted on the simulated 2D noble gas structure and the interatomic separation. The lines are guides for the eye. (c) Sequence of images showing selected steps from structural optimization starting with the twelve-atomic 3D Kr cluster in a graphene sandwich, which turns into a 2D structure. The change in energy from left to right between the configurations is −5.564, −0.565 and −0.033 eV, respectively. From [1] used with permission.

To get a more quantitative view the data was analyzed using self-written Python code described in the Section 3.1.8. Nearest neighbor distances for the clusters are shown in Fig. 4.23a. These are the in-plane projections, as only those can be observed, however, we assume the clusters to be flat, also due to the MD results. Both experimental and simulated results show clearly the same

trend, where the smallest clusters have the shortest interatomic distances, with the strongest effect seen in the experimental data for the Xe clusters. In all cases, the values are fairly constant with a slowly increasing trend for cluster sizes of $N \geq 10$, however, the spread within data sets was immense (the standard deviation was between 3 and 12 % of the measured value for Kr and Xe).

Comparing d_{nn} to the corresponding pressures estimated via simulations (Fig. 4.23b) shows that the smallest clusters are under a pressure of up to 1 GPa, whereas for the larger clusters this drops to around 0.3 GPa. These values are in the same range, but somewhat smaller than 1 GPa that has been estimated for 10 nm-sized clusters experimentally [59], and significantly lower than 30 GPa estimated for smaller He and Ar clusters computationally [109]. However, in neither of those cases were the clusters encapsulated between two graphene sheets.

The increasing pressure when the cluster size decreases is likely due to the higher necessary local curvature for graphene required for accommodating the smaller clusters. Additionally, the pressure for the smallest experimental clusters appears to increase even faster than what is predicted by the simulations. This can be related to the size of the point defect trapping the clusters, as will be discussed below. Also pressure is a relatively ill-defined term in two dimensions and it must be highly anisotropic in the sandwich.

To understand the influence of the graphene sandwich on the shape of the crystals, further structure optimization for cluster sizes up to 18 atoms (Fig. 4.24) were carried out by my colleague Harreit Åhlgren. These show, that in all cases, the optimum shape for the cluster (even at zero temperature) is three-dimensional for clusters larger than three atoms. As a plane is defined by three points a three atom cluster can only be two-dimensional. However, when larger clusters are placed inside the graphene sandwich, they relax into two-dimensional structures. All clusters retain the 2D shape between the graphene sheets, even up to 61 atoms, which was the maximum simulated cluster size. The change between the 3D and 2D structures is associated with an energy cost of ca. 60 meV/atom for the Xe_{18} cluster. This energy is compensated by the interface energy between the cluster and graphene, and the lower deformation energy for the graphene sandwich in the flatter configuration. An upper estimate for the interface energy (per atom) can be obtained by calculating the energy associated with an individual noble gas atom placed within two graphene sheets (total energy minus the energy of the similarly deformed graphene sheets without the additional atom). This is ca. 149 meV for Kr and ca. 66 meV for Xe, which shows that the interface energy has a similar order of magnitude as the energy difference of the 3D

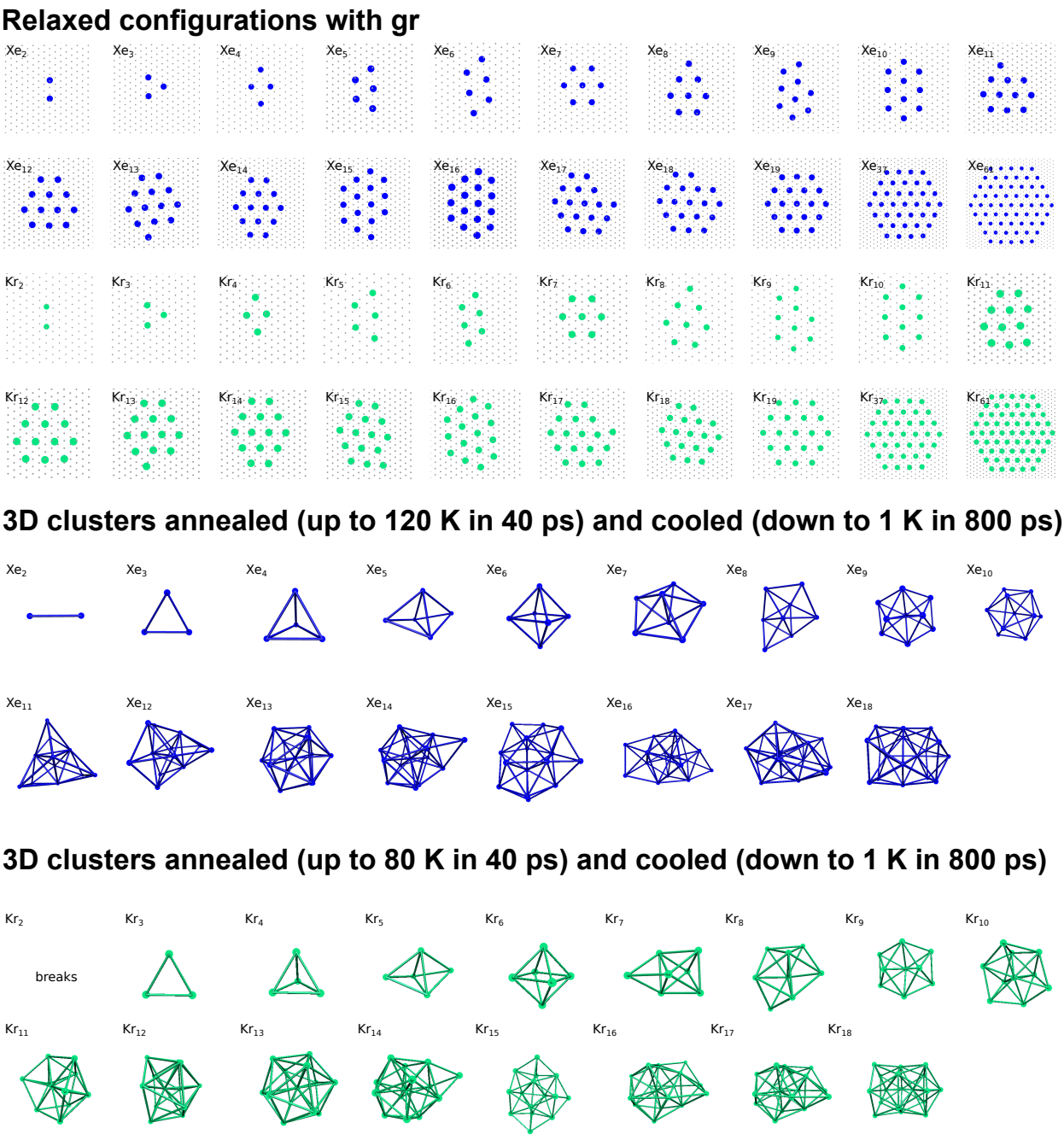

Figure 4.24: **Lowest-energy configurations of simulated cluster shapes in 2D and 3D.** Blue and green dots represent Xe and Kr atoms, respectively, the connecting lines for the 3D shapes represent the bonds. The four top rows show relaxed configurations of Xe and Kr between two layers of graphene. When graphene is removed the clusters do not take a 2D but a 3D shape. From [1] used with permission. Copyright ©2024, The Author(s), under exclusive licence to Springer Nature Limited.

and 2D clusters. Indeed, when graphene is removed from around the simulated 2D clusters, they transform to the 3D shape during further relaxation.

4.6.3 Dynamics

It is rather surprising, that the small clusters remain stationary at room temperature for long enough to allow their imaging in the microscope. In fact, one could even expect that all noble gas atoms would escape through edges from between the two graphene layers before they are able to form solid structures. While loosing all atoms is unlikely due to the large size of the samples (up to tens of μm for exfoliated samples and up to even mm for the CVD-grown ones) compared to atomic length scales, the motion of noble gases in the graphene sandwich warrants a discussion. To study this, we turn to room temperature molecular dynamics simulations. Simulations carried out by Harriet Åhlgren of individual Kr and Xe atoms show that they are both highly mobile in a graphene sandwich with estimated speeds of ca. 316 m/s and 233 m/s, respectively.

For three-atom clusters this changes to ca. 334 m/s and 231 m/s and for the Kr_7 cluster to ca. 369 m/s at 300 K. (The corresponding speeds in gas under normal conditions, according to ideal gas law, would be 180 m/s and 130 m/s, respectively, for two dimensions). Therefore, the migration barriers for both individual noble gas atoms as well as for few-atom clusters are clearly too low to prevent their migration at room temperature. Correspondingly, it should not be possible to image them given the experimental time resolution of ca. 1 s per image. The simulations further reveal that despite the weakness of the interaction between the noble gas atoms, already at $N = 3$, all atoms within the clusters move together rather than separating (also seen for Kr_7 in Fig. 4.27). This is in good agreement with our experimental results, where we only rarely observe detachment of individual atoms from the clusters.

Obviously, regardless of the fast expected migration, the clusters remain static for long enough for us to be able to image them. This suggests that the experimentally observed clusters are pinned to their positions either by corrugations associated with the surface contamination (many clusters appear at the edges of contamination) or by defects [167, 12], some of which are expected to lead to out-of-plane distortion of graphene [168]. To test this hypothesis, we created two different defects in the graphene sandwich, and simulated the migration of a Xe_3 cluster in both cases. We point out that these serve simply as examples of defects that would lead to either negative or positive Gaussian curvature in the graphene structure, and other defects may in reality be more likely to result from the low energy ion irradiation. In the first case, we introduce an interlayer covalent bond, which locally brings the two graphene sheets together (Fig. 4.25 a, c). This leads to the cluster avoiding the defect position and instead migrating everywhere else. In the second case, we introduced an inverse Stone-(Thrower)-Wales defect [169] that leads to negative

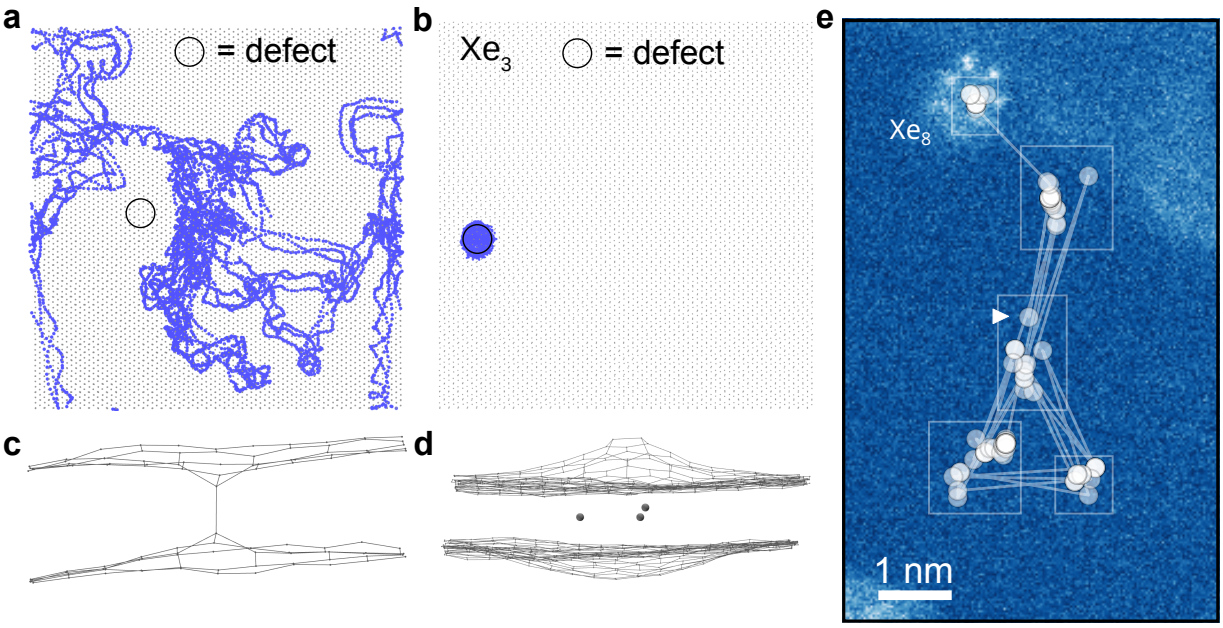

Figure 4.25: **Cluster migration.** (a) Trajectory of a Xe_3 cluster in a graphene sandwich with an interlayer bond-defect, simulated for ca. 1 ns via room temperature molecular dynamics. (b) Trajectory of a Xe_3 cluster in a graphene sandwich where one of the layers contains an inverse Stone-(Thrower)-Wales defect, simulated for ca. 1 ns. For both simulations, the positions for the cluster atoms are shown for every 0.1 ps, and the defect location is marked with an open circle. (c) Side view of graphene with the interlayer bond, where covalent bonds between the carbon atoms are shown with thin lines. (d) Side view of graphene with the inverse Stone-(Thrower)-Wales defect, and the Xe_3 cluster (shown with small balls). (e) Experimentally measured trajectory of an eight-atomic Xe cluster overlaid on a STEM-ADF image recorded at the end of the image sequence. The position of the cluster at the beginning of the sequence is marked with a white arrow, and the final position at the top of the image is visible due to the higher contrast of the Xe atoms. Positions for each of the images in the sequence are shown with semitransparent white circles, and the jumps between the images are marked with semitransparent white lines. The five distinct locations are highlighted with the rectangles. From [1] used with permission. Copyright ©2024, The Author(s), under exclusive licence to Springer Nature Limited.

curvature in graphene. Here, the Xe_3 cluster is clearly attracted to the defect, and once trapped in its vicinity, it remains there (Fig. 4.25 b, d). Although it can not be directly seen from the images, in both cases all atoms moved together throughout the whole simulation. We assume that similar to these simulations, also in our experiments the observed clusters are attracted to defect sites. Indeed, the ultralow-energy irradiation which is used to introduce the noble gas atoms into the graphene sandwich also by necessity creates defects into it. Some of them in turn are associated

with a negative curvature of the graphene sheet, which provides a favorable pocket for a small noble gas cluster.

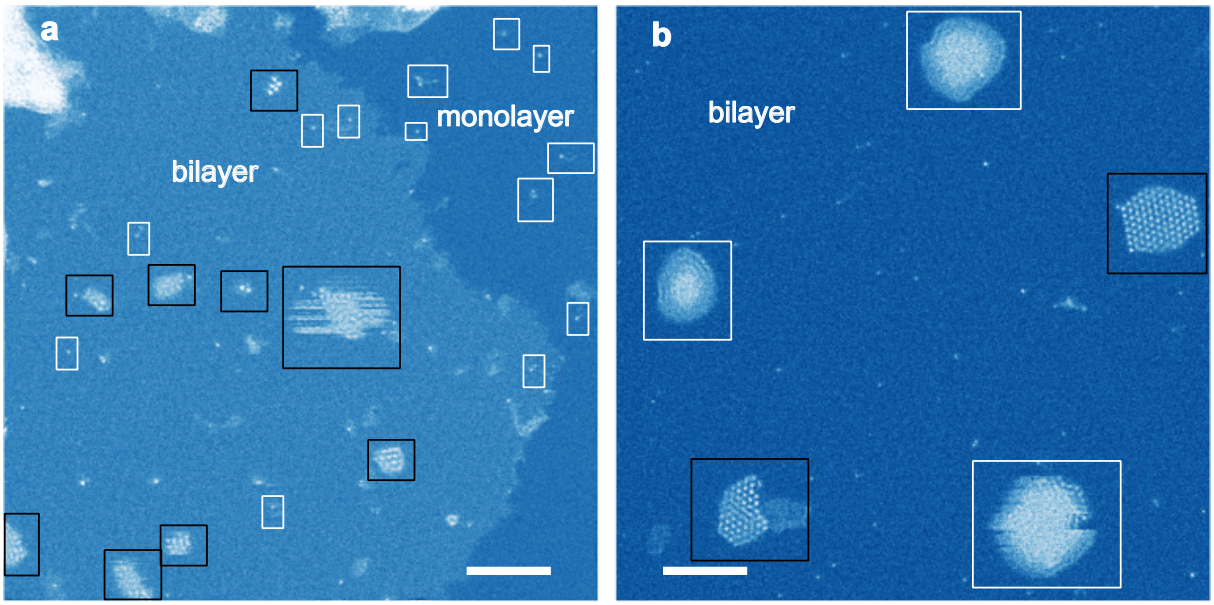

Figure 4.26: **Filtered STEM-MAADF images (see Section 3.1.8) showing (a) a step edge between a double layer and a single layer and (b) Xe clusters with $N \sim 100$ implanted in a double layer.** In panel (a) white rectangles mark some positions where Si heteroatoms have been trapped at defects in both areas, whereas black rectangles show locations of noble gas clusters, that are exclusively in the double layer area. In panel (b), black rectangles show solid Xe clusters and the white ones mark clusters that have a liquid-like structure. The larger solid cluster has $N = 93$ atoms, whereas the smallest liquid-like structure has only a few atoms more. Both images have been recorded on the same sample prepared from CVD-graphene, which–in contrast to all other samples–was implanted with Xe clusters with a plasma source at the University of Vienna, as described in Section 3.1.8. Both scale bars are 5 nm. From [1] used with permission. Copyright ©2024, The Author(s), under exclusive licence to Springer Nature Limited.

Point defects are indirectly visible both in single and double layer parts of the sample in Fig. 4.26 a (by covalently bound heavier impurity atoms [116]), which additionally shows that noble gas clusters are only trapped in the double layer, highlighting that they can only be captured within the van der Waals gap between two graphene layers. The size of the defect-related deformation may be a cause for the apparent unexpectedly high pressure for the smallest Xe clusters; the smallest clusters may fit into the deformation without further bending graphene by being squeezed tighter together leading to less bending in graphene but tighter pressed Xe atoms.

Interestingly, we also see occasionally that the clusters in the experiments jump between differ-

ent sites in the graphene sandwich, even in areas void of visible contamination. As an example, Fig. 4.25 e shows the trajectory of a Xe_8 cluster that was observed jumping between five different locations. Another example of a jumping cluster is shown in Fig. 4.27, where the cluster eventually merges with a stationary one.

The 60 keV electrons of the beam used for imaging here can transfer (at maximum) ca. 11.6 eV to a stationary carbon atom (and ca. 1.7 eV to a Kr and 1.1 eV to a Xe atom), which is enough to overcome the barrier associated with a local potential energy minimum within the graphene van der Waals gap, or to locally change the atomic structure of a defect site in graphene [170] that serves as the pinning site. These pinning sites cannot arise from the moiré superstructure of the two graphene layers, because we observe similar behavior for samples regardless of the relative orientation of the graphene sheets (and even for mechanically exfoliated graphene with AB stacking). Our interpretation is also in line with Ref. [171], where individual W atoms were observed to similarly jump between discrete positions in graphene, assumed to be associated with point defects. The main difference is that the W atoms migrate on top of graphene, whereas the noble gas clusters are confined within the van der Waals gap, which presumably has a significant influence on the associated energy barriers.

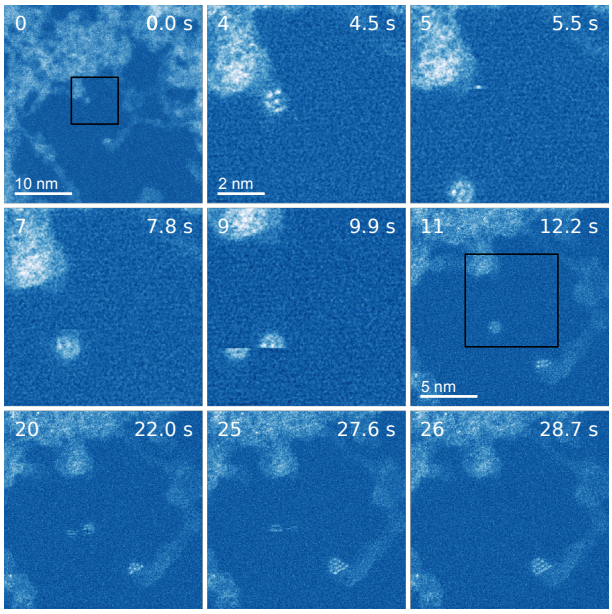

Figure 4.27: **Filtered STEM-MAADF images (see Section 3.1.8) of a Xe_6 cluster jumping between different positions, and finally merging with another cluster.** The labels correspond to the frame numbers within the image sequence and the corresponding time. The black squares on frames 0 and 11 show the area shown in frames 4 – 9. From [1] used with permission. Copyright ©2024, The Author(s), under exclusive licence to Springer Nature Limited.

4.6.4 Big clusters

One interesting question regarding the pressure-induced stability of 2D van der Waals atomic structures is under which conditions they remain solid. The solid-fluid phase transitions carry information of the size-dependent interaction strength within the noble gas clusters, being of high relevance for future studies. This is also interesting, since from a purely energetic point of view, one would expect smaller clusters to have a lower melting point and therefore to display liquid-like characteristics before the larger ones. However, in the case of our clusters sandwiched between two graphene sheets, this is counterbalanced by the increasing pressure for the decreasing cluster sizes, as discussed above. Nevertheless, it is natural to expect that there is a pressure- and temperature-dependant size limit, beyond which the energy cost of the undercoordinated atoms at the rim (corresponding to the surface energy of a 3D structure) becomes too large, and the structure undergoes a transformation into a three-dimensional shape. Phase diagrams suggest a solid-to-liquid transformation at room temperature for pressures slightly above 1 GPa for Kr and around 0.5 GPa for Xe [95]. Therefore, one would expect larger Kr clusters to loose their solid shape, which we indeed observe (Fig. 4.28). Although according to simulations, both Xe_{61} and Kr_{61} clusters should retain the 2D shape, experimental images (Fig. 4.28) show a brighter area within the Kr structure, which may indicate that the structure is not strictly two-dimensional. STM measurements on similar systems suggest that bilayers are formed [38, 39].

Indeed, Kr structures larger than $N \sim 16$ already start to show less defined atomic positions (at the rim already discussed earlier, see Fig. 4.18 a), and shapes that resemble liquid more than small crystallites. However, Xe clusters remain two-dimensional and exhibit characteristics of solid crystallite structures (clearly discernible atomic positions with long-range order) up to much larger sizes, although the estimated pressure is only 0.3 GPa. In fact, as shown in Fig. 4.26 b, the Xe clusters start to loose their solid characteristics only at the size of $N \sim 100$ atoms.

As evident in all the images of clearly liquid-like structures (Fig. 4.28 and Fig. 4.26), the solid-to-fluid transition is also associated with loosing the strict two-dimensionality. Although the energy per atom decreases faster for 3D clusters than for 2D ones (Fig 4.29), this energy gain is countered with a cost for deformation in graphene, which is larger for Xe than for Kr due to its larger size. This may provide a partial explanation for why Xe remains solid for much larger structures than Kr. Finally, we point out that as evident in Fig. 4.28, the larger clusters rotate during imaging, ruling out epitaxy with the graphene lattice.

Creation of small solid state noble gas clusters in a graphene sandwich, as was demonstrated here,

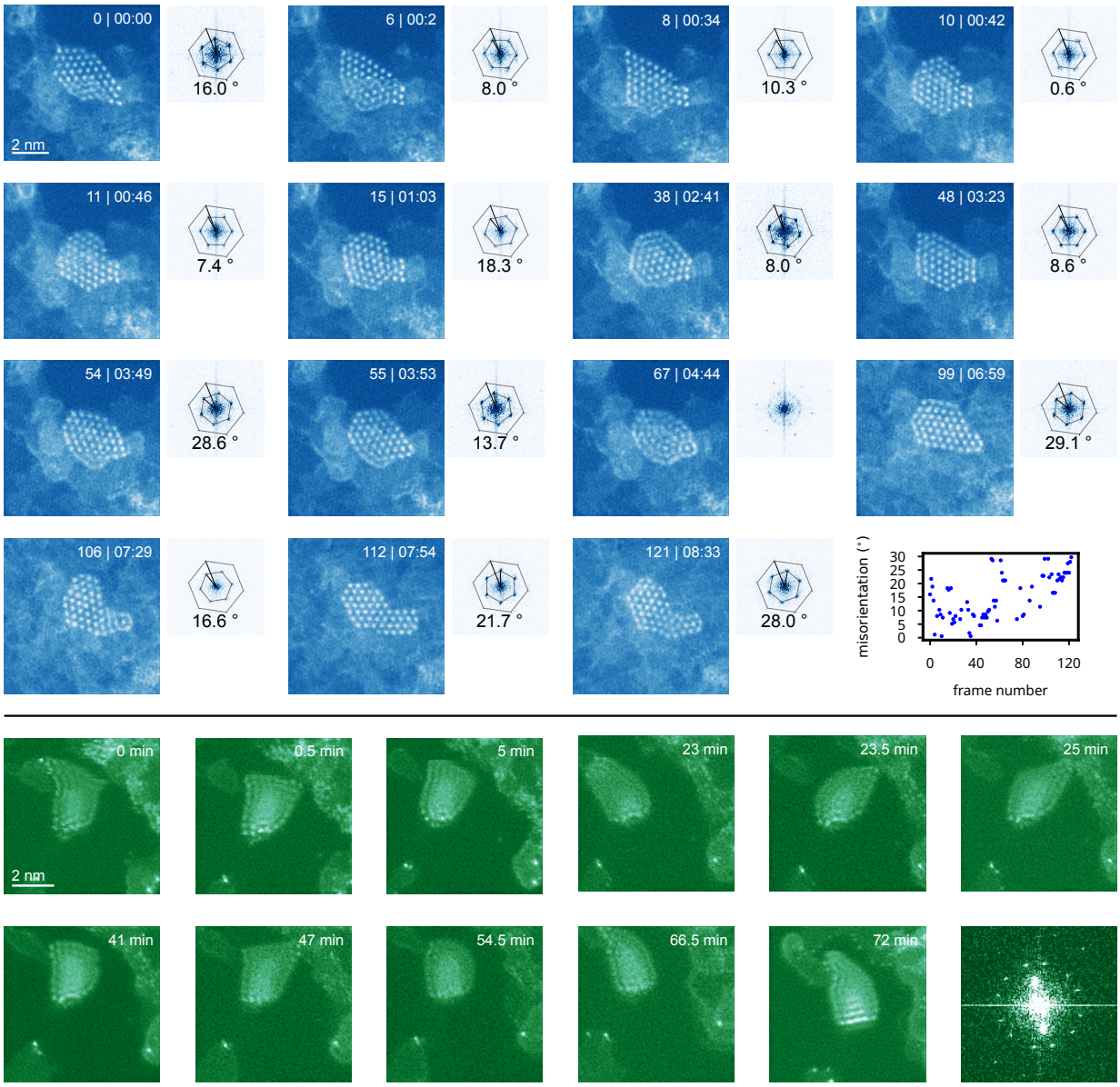

Figure 4.28: **Structure of larger clusters.** (Top) Filtered STEM-MAADF images of a Xe_{51} cluster within AB-stacked bilayer graphene that remains crystalline throughout the entire experiment (over 8 min). The numbers on the images indicate the frame number within the image sequence and the corresponding time. The small images next to them show a fast Fourier transform of each image with overlaid hexagons highlighting the spots corresponding to graphene and to the noble gas cluster and the misorientation angle between them. These angles for each image frame are shown in the plot in the lower right corner. (Bottom) Filtered STEM-HAADF images of a Kr cluster of a similar size. The provided example of a fast Fourier transform shows the orientation of the two graphene sheets in the double layer sandwich (misorientation of 25°). Due to the lack of crystallinity, the Kr cluster does not show characteristic spots. From [1] used with permission.

opens the so-far unexplored frontier of encapsulated 2D van der Waals atomic solids. Simulations show that the small clusters would assume a 3D shape without the graphene encapsulation, even at zero temperature, and that noble gas clusters are extremely mobile in the graphene sandwich, unless pinned to a position due to a deformation in at least one of the encapsulating graphene layers. Although small clusters remain solid for both Kr and Xe, larger Kr clusters ($N > 16$) start loosing their solid structure whereas Xe clusters remain solid up to $N \sim 100$. Larger solid structures may be achieved by providing more structural rigidity for example through increasing the number of the encapsulating layers, which can be expected to increase the pressure. Combined with *in situ* techniques for example allowing experimentation from cryogenic to elevated temperatures, encapsulated 2D noble gas structures provide exciting possibilities for studies in fundamental condensed matter physics ranging from research on the growth and atomic-scale dynamics in solids to phase transitions and topological defects.

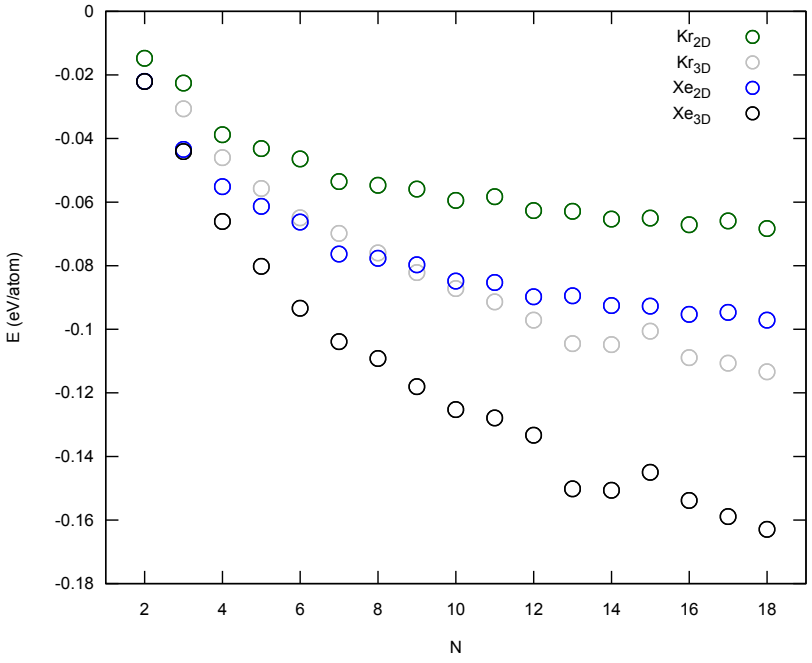

Figure 4.29: **Energy difference between 2D and 3D clusters.** The lowest-energy 3D structures were obtained by removing the graphene encapsulation and relaxing the clusters again after annealing. From [1] used with permission. Copyright ©2024, The Author(s), under exclusive licence to Springer Nature Limited.

Chapter 5

Conclusions

In this work we have shown that material manipulation using laser illumination, low-energy ion irradiation and energetic electron irradiation is promising for various use cases. Defect creation in graphene and hBN can be done using low-energy ion irradiation. A systematic experimental study on defect creation at the atomic level in hBN, a promising platform for quantum emitters, is done here for the first time. The defects in graphene have been filled with various desired heteroatoms, which should in principle also be possible using hBN. Energetic electrons were used to introduce defects for heteroatom incorporation and cluster growth while they were also used to draw nanometer-sized patterns using EBID. While direct proof for the combination of these two results is missing it offers a promising platform for patterned covalent implantation of desired species which enables material design at the atomic level. Lastly ultralow-energy noble gas ion irradiation was used to trap the impinging ions between individual sheets of graphene an hBN where they form 2D noble gas structures which have been thoroughly investigated.

Aberration-corrected STEM is the method enabling all of these experiments. Through CANVAS we are able to design and alter materials at the atomic level and gain fundamental understanding of their behaviour.

Developing implantation methods

The plasma source is a surprisingly powerful tool. When we started working with it it was a black box that people used while not even knowing what the beam leaving the source constitutes of. In the last few years we have learned that it delivers reproducible results better than anticipated. The energy spread is narrower than expected and the additional capability of decelerating ions

enables us to study physical effects at very low energies, such as trapping noble gases in bilayers.

Method development is always a lot of trial and error but the learning effect when taking instruments apart is extremely valuable. The amount of knowledge that can be extracted from a device using simple, home-built tools is very satisfying. What would still be desirable is an understanding of the (ion) energy-pressure relation.

Patterning defect structures

Here we show that the microscope stage is indeed reliable enough to write structures with EBID as intended. While the structures drawn with the electron beam do not show a one-to-one correspondence to the intended patterns the similarity is promising. The original goal of this project was to write patterns with covalently bound heteroatoms. Due to time constraints and other reasons here we can only show this motivation as a proof-of-concept. We are confident, however, that it will work as there is no obvious reason why it should not. Writing with contamination should be less reliable than introducing defects using high-energy electrons as there the cross section does not depend on the microscopic surrounding. The precision of stage movement might be an issue, as in fact there are deviations of the desired and actually reached stage positions, however, these stage movements were estimated to be small and it is yet to see whether they will pose a significant hindrance. Regarding the patterning of larger structures EBID might even be more practical due to the much higher interaction cross section and thus lower necessary exposure time. Evaporated adatoms can be used in both cases as they stick to contamination and to defects.

Implantation of covalently bound heteroatoms

A technique to introduce impurity atoms or nanoclusters reliably into graphene was demonstrated here. Atomically clean graphene produced with laser annealing in vacuum, and subsequent defect-engineering using low-energy ion irradiation in combination with PVD of the desired impurity species can be used to incorporate heteroatoms into graphene. This is demonstrated in this work for Fe. The density of the impurity configurations is controlled with the dose, whereas the sizes of the introduced structures are controlled with the amount of evaporated material, starting from individual impurity atoms. The created structures are expected to have applications in catalysis as well as single-atom microscopy and spectroscopy or even atom

manipulation.

Defect-engineering hBN

Here we demonstrated that low-energy Ar^+ irradiation is a suitable method for defect-engineering hBN with a high selectivity for boron single vacancies. The intrinsic defect concentration in the as-prepared and cleaned samples was found to be ca. 0.027 nm^{-2} (with 55.5 % boron and 8.1 % nitrogen vacancies). Additional ca. 0.003 defects per nm^2 was estimated to have been created during the automated imaging of the sample pre-irradiation. The ion irradiation dose was chosen high enough to separate the irradiation-induced defects from the intrinsic ones, but sufficiently low to avoid ions impinging on already defective sites. Most (55.7 %) of the irradiation-induced defects were boron single vacancies, followed by nitrogen single vacancies (11.5 %), double vacancies (14.4 %) and more complicated vacancy structures. These results are in contrast to earlier computational work predicting either similar probabilities for B and N single vacancies or a prevalence of N vacancies as a result of Ar^+ irradiation at similar energies. A potential error source for these measurements is that the data used for this study was obtained from only one sample at one position and thus is not confirmed for different samples and positions. This shows that more research is needed both experimentally and computationally to understand the possibilities for defect-engineering hBN with low-energy ions. The results show that defect-selectively indeed can be achieved with low energy noble gas irradiation. Future work should explore whether modifying irradiation parameters (ion species, kinetic energy, charge state, irradiation angle) changes the distribution either from boron to nitrogen single vacancies or towards more complicated defect structures.

Creating 2D noble gases

Trapping of noble gases between two layers of graphene and hBN was shown here. This opens the so-far unexplored frontier of encapsulated 2D van der Waals atomic solids. Simulations show that the small clusters would assume a 3D shape without the graphene encapsulation, even at zero temperature, and that noble gas clusters are extremely mobile in the graphene sandwich, unless pinned to a position due to a deformation in at least one of the encapsulating graphene layers. Although small clusters remain solid for both Kr and Xe, larger Kr clusters ($N > 16$) start loosing their solid structure whereas Xe clusters remain solid at least up to $N \sim 100$. Larger solid structures may be achieved by providing more structural rigidity for example through increasing

the number of the encapsulating layers. Combined with *in situ* techniques for example allowing experimentation from cryogenic to elevated temperatures, encapsulated 2D noble gas structures provide exciting possibilities for studies in fundamental condensed matter physics ranging from research on the growth and atomic-scale dynamics in solids to phase transitions and topological defects. They may also lead to well-defined quantum systems for example for quantum information research.

Not presented publications

1. Georg Zagler, Maximilian Stecher, Alberto Trentino, Fabian Kraft, Cong Su, Andreas Postl, **Manuel Längle**, Christian Pesenhofer, Clemens Mangler, E. Harriet Åhlgren, Alexander Markevich, Alex Zettl, Jani Kotakoski, Toma Susi, and Kimmo Mustonen
   Beam-driven dynamics of aluminium dopants in graphene, 2D Materials 9 (3) (2022) 035009. [14]

   Contributed by characterizing the plasma source.

2. Alberto Trentino, Kenichiro Mizohata, Georg Zagler, **Manuel Längle**, Kimmo Mustonen, Toma Susi, Jani Kotakoski and E Harriet Åhlgren
   Two-step implantation of gold into graphene, 2D Materials 9 (2) (2022) 025011. [13]

   Contributed by performing ion irradiation experiments.

3. **Manuel Längle**, Kenichiro Mizohata, E. Harriet Åhlgren, Alberto Trentino, Kimmo Mustonen and Jani Kotakoski
   2D Noble Gas Crystals Encapsulated in Few-layer Graphene, Microscopy and Microanalysis 26 (S2) (2020) 1086–1089. [69]

   Contributed by designing the experiments, preparing the samples, carrying out ion irradiation, carrying out microscopy, analysing the data, plotting the figures and writing the first draft of the manuscript.

Attended conferences

Table 5.1: **Conference and workshop participations**

Date, Location	Name	Contribution
August 2020, Online	Microscopy & Microanalysis 2020 Virtual Meeting	talk
August 2021, Online	ICPS 2021	talk
Sept. 2021, Online	EUROMAT	talk
April 2022, Linz, Austria	ASEM Workshop 2022	poster
July 2022, Aachen, Germany	Graphene 2022	poster
Sept. 2022, Brno, Czech Republic	16mcm	poster
March 2023, Kirchberg in Triol, Austria	IWEPNM	poster
April 2023, Vienna, Austria	ASEM Workshop 2023	poster
May 2023, Bad Honnef, Germany	Defects in Two-dimensional Materials	talk
Sept. 2023, Busan, South Korea	IMC20	talk and poster

Secondments

Table 5.2: **Secondments in other groups.**

Year, Location	Duration	Group	Task
2020, Helsinki	six weeks	Helsinki Accelerator Laboratory, University of Helsinki	ion irradiation experiments
2022, Berlin	one week	Koch group, Humboldt-Universität zu Berlin	electron microscopy
2023, Berlin	seven weeks	Koch group, Humboldt-Universität zu Berlin	electron microscopy

Teaching

Table 5.3: **Teaching experience.**

Semester	Course	Role
Winter 2020	The societal responsibility of higher education institutions	lecturer and organizer
Winter 2021	Programming for Physicists	exercise class teacher
Winter 2022	Programming for Physicists	exercise class teacher
Summer 2022	Telling your story - science communication of research projects	lecturer and co-organizer
Winter 2023	Programming for Physicists	exercise class teacher

Student mentoring

Table 5.4: **Research Guidance mentoring.**

Name	Role	Topic
Daniel Imrich	M. Sc. student	defect patterning
Nika Pesenhofer	M. Sc. student	plasma source
Barbara Maria Mayer	B. Sc. student	defects in hBN
Luis Alfredo Ixquiac Méndez	summer intern	defects in hBN
Vinzent Hana	B. Sc. Student	plasma source

Bibliography

[1] M. Längle, K. Mizohata, C. Mangler, A. Trentino, K. Mustonen, E. H. Åhlgren, J. Kotakoski, Two-dimensional few-atom noble gas clusters in a graphene sandwich, Nature Materials (Jan. 2024). doi:10.1038/s41563-023-01780-1.

[2] M. Längle, B. M. Mayer, J. Madsen, D. Propst, A. Bo, C. Kofler, V. Hana, C. Mangler, T. Susi, J. Kotakoski, Defect-engineering of hexagonal boron nitride via low-energy plasma irradiation, in preparation.

[3] A. Trentino, G. Zagler, M. Längle, J. Madsen, T. Susi, C. Mangler, E. H. Åhlgren, K. Mustonen, J. Kotakoski, Single atoms and metal nanoclusters anchored to graphene vacancies, submitted for publication.

[4] K. S. Novoselov, Electric Field Effect in Atomically Thin Carbon Films, Science 306 (5696) (2004) 666–669. doi:10.1126/science.1102896.

[5] A. R. Urade, I. Lahiri, K. S. Suresh, Graphene Properties, Synthesis and Applications: A Review, JOM 75 (3) (2023) 614–630. doi:10.1007/s11837-022-05505-8.

[6] S. Das, M. Kim, J.-w. Lee, W. Choi, Synthesis, Properties, and Applications of 2-D Materials: A Comprehensive Review, Critical Reviews in Solid State and Materials Sciences 39 (4) (2014) 231–252. doi:10.1080/10408436.2013.836075.

[7] M. Schleberger, J. Kotakoski, 2D Material Science: Defect Engineering by Particle Irradiation, Materials 11 (10) (2018) 1885. doi:10.3390/ma11101885.

[8] Z. Li, F. Chen, Ion beam modification of two-dimensional materials: Characterization, properties, and applications, Applied Physics Reviews 4 (1) (2017) 011103. doi:10.1063/1.4977087.

[9] M. Fox, R. Ispasoiu, Quantum Wells, Superlattices, and Band-Gap Engineering, in: S. Kasap, P. Capper (Eds.), Springer Handbook of Electronic and Photonic Materials, Springer Handbooks, Springer International Publishing, 2017. doi:10.1007/978-3-319-48933-9_40.

[10] C. Mangler, J. Meyer, A. Mittelberger, K. Mustonen, T. Susi, J. Kotakoski, A Materials Scientist's CANVAS: A System for Controlled Alteration of Nanomaterials in Vacuum Down to the Atomic Scale, Microscopy and Microanalysis 28 (S1) (2022) 2940–2942. doi:10.1017/S1431927622011023.

[11] G. Cassabois, P. Valvin, B. Gil, Hexagonal boron nitride is an indirect bandgap semiconductor, Nature Photonics 10 (4) (2016) 262–266. doi:10.1038/nphoton.2015.277.

[12] A. Trentino, J. Madsen, A. Mittelberger, C. Mangler, T. Susi, K. Mustonen, J. Kotakoski, Atomic-Level Structural Engineering of Graphene on a Mesoscopic Scale, Nano Letters 21 (12) (2021) 5179–5185. doi:10.1021/acs.nanolett.1c01214.

[13] A. Trentino, K. Mizohata, G. Zagler, M. Längle, K. Mustonen, T. Susi, J. Kotakoski, E. H. Åhlgren, Two-step implantation of gold into graphene, 2D Materials 9 (2) (2022) 025011. doi:10.1088/2053-1583/ac4e9c.

[14] G. Zagler, M. Stecher, A. Trentino, F. Kraft, C. Su, A. Postl, M. Längle, C. Pesenhofer, C. Mangler, E. H. Åhlgren, A. Markevich, A. Zettl, J. Kotakoski, T. Susi, K. Mustonen, Beam-driven dynamics of aluminium dopants in graphene, 2D Materials 9 (3) (2022) 035009. doi:10.1088/2053-1583/ac6c30.

[15] F. S. Hage, G. Radtke, D. M. Kepaptsoglou, M. Lazzeri, Q. M. Ramasse, Single-atom vibrational spectroscopy in the scanning transmission electron microscope, Science 367 (6482) (2020) 1124–1127. doi:10.1126/science.aba1136.

[16] R. Ishikawa, S. D. Findlay, T. Seki, G. Sánchez-Santolino, Y. Kohno, Y. Ikuhara, N. Shibata, Direct electric field imaging of graphene defects, Nature Communications 9 (1) (2018) 3878. doi:10.1038/s41467-018-06387-8.

[17] T. Susi, J. C. Meyer, J. Kotakoski, Manipulating low-dimensional materials down to the level of single atoms with electron irradiation, Ultramicroscopy 180 (2017) 163–172. doi:10.1016/j.ultramic.2017.03.005.

[18] M. Tripathi, A. Mittelberger, N. A. Pike, C. Mangler, J. C. Meyer, M. J. Verstraete, J. Kotakoski, T. Susi, Electron-Beam Manipulation of Silicon Dopants in Graphene, Nano Letters 18 (8) (2018) 5319–5323. doi:10.1021/acs.nanolett.8b02406.

[19] C. Su, M. Tripathi, Q.-B. Yan, Z. Wang, Z. Zhang, C. Hofer, H. Wang, L. Basile, G. Su, M. Dong, J. C. Meyer, J. Kotakoski, J. Kong, J.-C. Idrobo, T. Susi, J. Li, Engineering single-atom dynamics with electron irradiation, Science Advances 5 (5) (2019) eaav2252. doi:10.1126/sciadv.aav2252.

[20] O. Dyck, M. Ziatdinov, D. B. Lingerfelt, R. R. Unocic, B. M. Hudak, A. R. Lupini, S. Jesse, S. V. Kalinin, Atom-by-atom fabrication with electron beams, Nature Reviews Materials 4 (7) (2019) 497–507. doi:10.1038/s41578-019-0118-z.

[21] A. Mittelberger, C. Kramberger, C. Hofer, C. Mangler, J. C. Meyer, Automated Image Acquisition for Low-Dose STEM at Atomic Resolution, Microscopy and Microanalysis 23 (4) (2017) 809–817. doi:10.1017/S1431927617000575.

[22] O. Dyck, L. Zhang, M. Yoon, J. L. Swett, D. Hensley, C. Zhang, P. D. Rack, J. D. Fowlkes, A. R. Lupini, S. Jesse, Doping transition-metal atoms in graphene for atomic-scale tailoring of electronic, magnetic, and quantum topological properties, Carbon 173 (2021) 205–214. doi:10.1016/j.carbon.2020.11.015.

[23] O. Dyck, S. Yeom, A. R. Lupini, J. L. Swett, D. Hensley, M. Yoon, S. Jesse, Top-Down Fabrication of Atomic Patterns in Twisted Bilayer Graphene, Advanced Materials 35 (32) (2023) 2302906. doi:10.1002/adma.202302906.

[24] A. Sajid, M. J. Ford, J. R. Reimers, Single-photon emitters in hexagonal boron nitride: a review of progress, Reports on Progress in Physics 83 (4) (2020) 044501. doi:10.1088/1361-6633/ab6310.

[25] J. Zhang, R. Sun, D. Ruan, M. Zhang, Y. Li, K. Zhang, F. Cheng, Z. Wang, Z.-M. Wang, Point defects in two-dimensional hexagonal boron nitride: A perspective, Journal of Applied Physics 128 (10) (2020) 100902. doi:10.1063/5.0021093.

[26] L. Gan, D. Zhang, R. Zhang, Q. Zhang, H. Sun, Y. Li, C.-Z. Ning, Large-Scale, High-Yield Laser Fabrication of Bright and Pure Single-Photon Emitters at Room Temperature in Hexagonal Boron Nitride, ACS Nano 16 (9) (2022) 14254–14261. doi:10.1021/acsnano.2c04386.

[27] S. Choi, T. T. Tran, C. Elbadawi, C. Lobo, X. Wang, S. Juodkazis, G. Seniutinas, M. Toth, I. Aharonovich, Engineering and Localization of Quantum Emitters in Large Hexagonal Boron Nitride Layers, ACS Applied Materials & Interfaces 8 (43) (2016) 29642–29648. doi:10.1021/acsami.6b09875.

[28] H. Zhang, M. Lan, G. Tang, F. Chen, Z. Shu, F. Chen, M. Li, Discrete color centers in two-dimensional hexagonal boron nitride induced by fast neutron irradiation, Journal of Materials Chemistry C 7 (39) (2019) 12211–12216. doi:10.1039/C9TC03695D.

[29] A. L. Exarhos, D. A. Hopper, R. R. Grote, A. Alkauskas, L. C. Bassett, Optical Signatures of Quantum Emitters in Suspended Hexagonal Boron Nitride, ACS Nano 11 (3) (2017) 3328–3336. doi:10.1021/acsnano.7b00665.

[30] C. Su, F. Zhang, S. Kahn, B. Shevitski, J. Jiang, C. Dai, A. Ungar, J.-H. Park, K. Watanabe, T. Taniguchi, J. Kong, Z. Tang, W. Zhang, F. Wang, M. Crommie, S. G. Louie, S. Aloni, A. Zettl, Tuning colour centres at a twisted hexagonal boron nitride interface, Nature Materials 21 (8) (2022) 896–902. doi:10.1038/s41563-022-01303-4.

[31] T. A. Bui, G. T. Leuthner, J. Madsen, M. R. A. Monazam, A. I. Chirita, A. Postl, C. Mangler, J. Kotakoski, T. Susi, Creation of Single Vacancies in hBN with Electron Irradiation, Small (2023) 2301926doi:10.1002/smll.202301926.

[32] O. Lehtinen, E. Dumur, J. Kotakoski, A. Krasheninnikov, K. Nordlund, J. Keinonen, Production of defects in hexagonal boron nitride monolayer under ion irradiation, Nuclear Instruments and Methods in Physics Research Section B: Beam Interactions with Materials and Atoms 269 (11) (2011) 1327–1331. doi:10.1016/j.nimb.2010.11.027.

[33] S. Ghaderzadeh, S. Kretschmer, M. Ghorbani-Asl, G. Hlawacek, A. V. Krasheninnikov, Atomistic Simulations of Defect Production in Monolayer and Bulk Hexagonal Boron Nitride under Low- and High-Fluence Ion Irradiation, Nanomaterials 11 (5) (2021) 1214. doi:10.3390/nano11051214.

[34] J. S. Bunch, S. S. Verbridge, J. S. Alden, A. M. van der Zande, J. M. Parpia, H. G. Craighead, P. L. McEuen, Impermeable Atomic Membranes from Graphene Sheets, Nano Letters 8 (8) (2008) 2458–2462. doi:10.1021/nl801457b.

[35] R. Gross, A. Marx, Festkörperphysik, Oldenbourg Wissenschaftsverlag, 2012.

[36] G. Grosso, G. Pastori Parravicini, Solid state physics, second edition Edition, Academic Press, Elsevier, Amsterdam, 2014.

[37] J. Jortner, L. Meyer, S. A. Rice, E. G. Wilson, Localized Excitations in Condensed Ne, Ar, Kr, and Xe, The Journal of Chemical Physics 42 (12) (1965) 4250–4253. doi:10.1063/1.1695927.

[38] P. Valerius, C. Herbig, M. Will, M. A. Arman, J. Knudsen, V. Caciuc, N. Atodiresei, T. Michely, Annealing of ion-irradiated hexagonal boron nitride on Ir(111), Physical Review B 96 (23) (2017) 235410. doi:10.1103/PhysRevB.96.235410.

[39] C. Herbig, T. Michely, Graphene: the ultimately thin sputtering shield, 2D Materials 3 (2) (2016) 025032. doi:10.1088/2053-1583/3/2/025032.

[40] C. Herbig, E. H. Åhlgren, W. Jolie, C. Busse, J. Kotakoski, A. V. Krasheninnikov, T. Michely, Interfacial Carbon Nanoplatelet Formation by Ion Irradiation of Graphene on Iridium(111), ACS Nano 8 (12) (2014) 12208–12218. doi:10.1021/nn503874n.

[41] C. Herbig, E. H. Åhlgren, U. A. Schröder, A. J. Martínez-Galera, M. A. Arman, W. Jolie, C. Busse, J. Kotakoski, J. Knudsen, A. V. Krasheninnikov, T. Michely, Comment on "Interfacial Carbon Nanoplatelet Formation by Ion Irradiation of Graphene on Iridium(111)", ACS Nano 9 (5) (2015) 4664–4665. doi:10.1021/acsnano.5b02303.

[42] A. K. Geim, Graphene: Status and Prospects, Science 324 (5934) (2009) 1530–1534. doi:10.1126/science.1158877.

[43] A. K. Geim, K. S. Novoselov, The rise of graphene, Nature Materials 6 (3) (2007) 183–191. doi:10.1038/nmat1849.

[44] A. Gupta, T. Sakthivel, S. Seal, Recent development in 2D materials beyond graphene, Progress in Materials Science 73 (2015) 44–126. doi:10.1016/j.pmatsci.2015.02.002.

[45] K. S. Novoselov, D. Jiang, F. Schedin, T. J. Booth, V. V. Khotkevich, S. V. Morozov, A. K. Geim, Two-dimensional atomic crystals, Proceedings of the National Academy of Sciences of the United States of America 102 (30) (2005) 10451. doi:10.1073/pnas.0502848102.

[46] A. Pakdel, Y. Bando, D. Golberg, Nano boron nitride flatland, Chemical Society Reviews 43 (3) (2014) 934–959. doi:10.1039/C3CS60260E.

[47] M. Tripathi, Modifying low-dimensional materials using energetic charged particles, PhD Thesis, Wien (2019).

[48] S. Roy, X. Zhang, A. B. Puthirath, A. Meiyazhagan, S. Bhattacharyya, M. M. Rahman, G. Babu, S. Susarla, S. K. Saju, M. K. Tran, L. M. Sassi, M. A. S. R. Saadi, J. Lai, O. Sahin, S. M. Sajadi, B. Dharmarajan, D. Salpekar, N. Chakingal, A. Baburaj, X. Shuai, A. Adumbumkulath, K. A. Miller, J. M. Gayle, A. Ajnsztajn, T. Prasankumar, V. V. J. Harikrishnan, V. Ojha, H. Kannan, A. Z. Khater, Z. Zhu, S. A. Iyengar, P. A. D. S. Autreto, E. F. Oliveira, G. Gao, A. G. Birdwell, M. R. Neupane, T. G. Ivanov, J. Taha-Tijerina, R. M. Yadav, S. Arepalli, R. Vajtai, P. M. Ajayan, Structure, Properties and Applications of Two-Dimensional Hexagonal Boron Nitride, Advanced Materials 33 (44) (2021) 2101589. doi:10.1002/adma.202101589.

[49] C. Lee, X. Wei, J. W. Kysar, J. Hone, Measurement of the Elastic Properties and Intrinsic Strength of Monolayer Graphene, Science 321 (5887) (2008) 385. doi:10.1126/science.1157996.

[50] J.-U. Lee, D. Yoon, H. Cheong, Estimation of Young's Modulus of Graphene by Raman Spectroscopy, Nano Letters 12 (9) (2012) 4444–4448. doi:10.1021/nl301073q.

[51] A. Falin, Q. Cai, E. J. Santos, D. Scullion, D. Qian, R. Zhang, Z. Yang, S. Huang, K. Watanabe, T. Taniguchi, M. R. Barnett, Y. Chen, R. S. Ruoff, L. H. Li, Mechanical properties of atomically thin boron nitride and the role of interlayer interactions, Nature Communications 8 (1) (2017) 15815. doi:10.1038/ncomms15815.

[52] H. Rokni, W. Lu, Direct measurements of interfacial adhesion in 2D materials and van der Waals heterostructures in ambient air, Nature Communications 11 (1) (2020) 5607. doi:10.1038/s41467-020-19411-7.

[53] A. A. Balandin, S. Ghosh, W. Bao, I. Calizo, D. Teweldebrhan, F. Miao, C. N. Lau, Superior Thermal Conductivity of Single-Layer Graphene, Nano Letters 8 (3) (2008) 902–907. doi:10.1021/nl0731872.

[54] Q. Cai, D. Scullion, W. Gan, A. Falin, S. Zhang, K. Watanabe, T. Taniguchi, Y. Chen, E. J. G. Santos, L. H. Li, High thermal conductivity of high-quality monolayer boron nitride and its thermal expansion, Science Advances 5 (6) (2019) eaav0129. doi:10.1126/sciadv.aav0129.

[55] L. H. Li, J. Cervenka, K. Watanabe, T. Taniguchi, Y. Chen, Strong Oxidation Resistance of Atomically Thin Boron Nitride Nanosheets, ACS Nano 8 (2) (2014) 1457–1462. doi:10.1021/nn500059s.

[56] F. Liu, M. Wang, Y. Chen, J. Gao, Thermal stability of graphene in inert atmosphere at high temperature, Journal of Solid State Chemistry 276 (2019) 100–103. doi:10.1016/j.jssc.2019.04.008.

[57] P. Z. Sun, Q. Yang, W. J. Kuang, Y. V. Stebunov, W. Q. Xiong, J. Yu, R. R. Nair, M. I. Katsnelson, S. J. Yuan, I. V. Grigorieva, M. Lozada-Hidalgo, F. C. Wang, A. K. Geim, Limits on gas impermeability of graphene, Nature 579 (7798) (2020) 229–232. doi:10.1038/s41586-020-2070-x.

[58] E. Stolyarova, D. Stolyarov, K. Bolotin, S. Ryu, L. Liu, K. T. Rim, M. Klima, M. Hybertsen, I. Pogorelsky, I. Pavlishin, K. Kusche, J. Hone, P. Kim, H. L. Stormer, V. Yakimenko, G. Flynn, Observation of Graphene Bubbles and Effective Mass Transport under Graphene Films, Nano Letters 9 (1) (2009) 332–337. doi:10.1021/nl803087x.

[59] K. S. Vasu, E. Prestat, J. Abraham, J. Dix, R. J. Kashtiban, J. Beheshtian, J. Sloan, P. Carbone, M. Neek-Amal, S. J. Haigh, A. K. Geim, R. R. Nair, Van der Waals pressure and its effect on trapped interlayer molecules, Nature Communications 7 (1) (2016) 12168. doi:10.1038/ncomms12168.

[60] M. Kühne, F. Börrnert, S. Fecher, M. Ghorbani-Asl, J. Biskupek, D. Samuelis, A. V. Krasheninnikov, U. Kaiser, J. H. Smet, Reversible superdense ordering of lithium between two graphene sheets, Nature 564 (7735) (2018) 234–239. doi:10.1038/s41586-018-0754-2.

[61] R. Mirzayev, K. Mustonen, M. R. A. Monazam, A. Mittelberger, T. J. Pennycook, C. Mangler, T. Susi, J. Kotakoski, J. C. Meyer, Buckyball sandwiches, Science Advances 3 (6) (2017) e1700176. doi:10.1126/sciadv.1700176.

[62] M. Kühne, F. Paolucci, J. Popovic, P. M. Ostrovsky, J. Maier, J. H. Smet, Ultrafast lithium diffusion in bilayer graphene, Nature Nanotechnology 12 (9) (2017) 895–900. doi:10.1038/nnano.2017.108.

[63] L. H. Li, T. Xing, Y. Chen, R. Jones, Boron Nitride Nanosheets for Metal Protection, Advanced Materials Interfaces 1 (8) (2014) 1300132. doi:10.1002/admi.201300132.

[64] J. C. Meyer, F. Eder, S. Kurasch, V. Skakalova, J. Kotakoski, H. J. Park, S. Roth, A. Chuvilin, S. Eyhusen, G. Benner, A. V. Krasheninnikov, U. Kaiser, Accurate Measurement of Electron Beam Induced Displacement Cross Sections for Single-Layer Graphene, Physical Review Letters 108 (19) (2012) 196102. doi:10.1103/PhysRevLett.108.196102.

[65] T. Susi, C. Hofer, G. Argentero, G. T. Leuthner, T. J. Pennycook, C. Mangler, J. C. Meyer, J. Kotakoski, Isotope analysis in the transmission electron microscope, Nature Communications 7 (1) (2016) 13040. doi:10.1038/ncomms13040.

[66] X. Ye, M. R. Jones, L. B. Frechette, Q. Chen, A. S. Powers, P. Ercius, G. Dunn, G. M. Rotskoff, S. C. Nguyen, V. P. Adiga, A. Zettl, E. Rabani, P. L. Geissler, A. P. Alivisatos, Single-particle mapping of nonequilibrium nanocrystal transformations, Science 354 (6314) (2016) 874–877. doi:10.1126/science.aah4434.

[67] J. M. Yuk, J. Park, P. Ercius, K. Kim, D. J. Hellebusch, M. F. Crommie, J. Y. Lee, A. Zettl, A. P. Alivisatos, High-Resolution EM of Colloidal Nanocrystal Growth Using Graphene Liquid Cells, Science 336 (6077) (2012) 61–64. doi:10.1126/science.1217654.

[68] R. S. Pantelic, J. C. Meyer, U. Kaiser, H. Stahlberg, The application of graphene as a sample support in transmission electron microscopy, Solid State Communications 152 (15) (2012) 1375–1382. doi:10.1016/j.ssc.2012.04.038.

[69] M. Längle, K. Mizohata, E. H. Åhlgren, A. Trentino, K. Mustonen, J. Kotakoski, 2D Noble Gas Crystals Encapsulated in Few-layer Graphene, Microscopy and Microanalysis 26 (S2) (2020) 1086–1089. doi:10.1017/S1431927620016918.

[70] J. Kotakoski, C. Jin, O. Lehtinen, K. Suenaga, A. Krasheninnikov, Electron knock-on damage in hexagonal boron nitride monolayers, Physical Review B 82 (11) (2010) 113404. doi:10.1103/PhysRevB.82.113404.

[71] A. H. Castro Neto, F. Guinea, N. M. R. Peres, K. S. Novoselov, A. K. Geim, The electronic properties of graphene, Reviews of Modern Physics 81 (1) (2009) 109–162. doi:10.1103/RevModPhys.81.109.

[72] K. Bolotin, K. Sikes, Z. Jiang, M. Klima, G. Fudenberg, J. Hone, P. Kim, H. Stormer, Ultrahigh electron mobility in suspended graphene, Solid State Communications 146 (9-10) (2008) 351–355. doi:10.1016/j.ssc.2008.02.024.

[73] K. S. Novoselov, A. K. Geim, S. V. Morozov, D. Jiang, M. I. Katsnelson, I. V. Grigorieva, S. V. Dubonos, A. A. Firsov, Two-dimensional gas of massless Dirac fermions in graphene, Nature 438 (7065) (2005) 197–200. doi:10.1038/nature04233.

[74] R. R. Nair, P. Blake, A. N. Grigorenko, K. S. Novoselov, T. J. Booth, T. Stauber, N. M. R. Peres, A. K. Geim, Fine Structure Constant Defines Visual Transparency of Graphene, Science 320 (5881) (2008) 1308–1308. doi:10.1126/science.1156965.

[75] K. Watanabe, T. Taniguchi, H. Kanda, Direct-bandgap properties and evidence for ultraviolet lasing of hexagonal boron nitride single crystal, Nature Materials 3 (6) (2004) 404–409. doi:10.1038/nmat1134.

[76] E. Doni, G. P. Parravicini, Energy bands and optical properties of hexagonal boron nitride and graphite, Il Nuovo Cimento B Series 10 64 (1) (1969) 117–144. doi:10.1007/BF02710286.

[77] M. Kianinia, B. Regan, S. A. Tawfik, T. T. Tran, M. J. Ford, I. Aharonovich, M. Toth, Robust Solid-State Quantum System Operating at 800 K, ACS Photonics 4 (4) (2017) 768–773. doi:10.1021/acsphotonics.7b00086.

[78] T. T. Tran, K. Bray, M. J. Ford, M. Toth, I. Aharonovich, Quantum emission from hexagonal boron nitride monolayers, Nature Nanotechnology 11 (1) (2016) 37–41. doi:10.1038/nnano.2015.242.

[79] T. T. Tran, C. Elbadawi, D. Totonjian, C. J. Lobo, G. Grosso, H. Moon, D. R. Englund, M. J. Ford, I. Aharonovich, M. Toth, Robust Multicolor Single Photon Emission from Point Defects in Hexagonal Boron Nitride, ACS Nano 10 (8) (2016) 7331–7338. doi:10.1021/acsnano.6b03602.

[80] R. Bourrellier, S. Meuret, A. Tararan, O. Stéphan, M. Kociak, L. H. G. Tizei, A. Zobelli, Bright UV Single Photon Emission at Point Defects in h-BN, Nano Letters 16 (7) (2016) 4317–4321. doi:10.1021/acs.nanolett.6b01368.

[81] A. Gottscholl, M. Kianinia, V. Soltamov, S. Orlinskii, G. Mamin, C. Bradac, C. Kasper, K. Krambrock, A. Sperlich, M. Toth, I. Aharonovich, V. Dyakonov, Initialization and readout of intrinsic spin defects in a van der Waals crystal at room temperature, Nature Materials 19 (5) (2020) 540–545. doi:10.1038/s41563-020-0619-6.

[82] M. Hoese, P. Reddy, A. Dietrich, M. K. Koch, K. G. Fehler, M. W. Doherty, A. Kubanek, Mechanical decoupling of quantum emitters in hexagonal boron nitride from low-energy phonon modes, Science Advances 6 (40) (2020) eaba6038. doi:10.1126/sciadv.aba6038.

[83] A. Dietrich, M. W. Doherty, I. Aharonovich, A. Kubanek, Solid-state single photon source with Fourier transform limited lines at room temperature, Physical Review B 101 (8) (2020) 081401. doi:10.1103/PhysRevB.101.081401.

[84] N. P. De Leon, K. M. Itoh, D. Kim, K. K. Mehta, T. E. Northup, H. Paik, B. S. Palmer, N. Samarth, S. Sangtawesin, D. W. Steuerman, Materials challenges and opportunities for quantum computing hardware, Science 372 (6539) (2021) eabb2823. doi:10.1126/science.abb2823.

[85] D. Wong, J. Velasco, L. Ju, J. Lee, S. Kahn, H.-Z. Tsai, C. Germany, T. Taniguchi, K. Watanabe, A. Zettl, F. Wang, M. F. Crommie, Characterization and manipulation of individual defects in insulating hexagonal boron nitride using scanning tunnelling microscopy, Nature Nanotechnology 10 (11) (2015) 949–953. doi:10.1038/nnano.2015.188.

[86] M. Abdi, J.-P. Chou, A. Gali, M. B. Plenio, Color Centers in Hexagonal Boron Nitride Monolayers: A Group Theory and Ab Initio Analysis, ACS Photonics 5 (5) (2018) 1967–1976. doi:10.1021/acsphotonics.7b01442.

[87] Y. Huang, E. Sutter, N. N. Shi, J. Zheng, T. Yang, D. Englund, H.-J. Gao, P. Sutter, Reliable Exfoliation of Large-Area High-Quality Flakes of Graphene and Other Two-Dimensional Materials, ACS Nano 9 (11) (2015) 10612–10620. doi:10.1021/acsnano.5b04258.

[88] P. Blake, E. W. Hill, A. H. Castro Neto, K. S. Novoselov, D. Jiang, R. Yang, T. J. Booth, A. K. Geim, Making graphene visible, Applied Physics Letters 91 (6) (2007) 063124. doi:10.1063/1.2768624.

[89] R. Muñoz, C. Gómez-Aleixandre, Review of CVD Synthesis of Graphene, Chemical Vapor Deposition 19 (10-11-12) (2013) 297–322. doi:10.1002/cvde.201300051.

[90] K. K. Kim, A. Hsu, X. Jia, S. M. Kim, Y. Shi, M. Hofmann, D. Nezich, J. F. Rodriguez-Nieva, M. Dresselhaus, T. Palacios, J. Kong, Synthesis of Monolayer Hexagonal Boron Nitride on Cu Foil Using Chemical Vapor Deposition, Nano Letters 12 (1) (2012) 161–166. doi:10.1021/nl203249a.

[91] M. R. Ahmadpour Monazam, U. Ludacka, H.-P. Komsa, J. Kotakoski, Substitutional Si impurities in monolayer hexagonal boron nitride, Applied Physics Letters 115 (7) (2019) 071604. doi:10.1063/1.5112375.

[92] J. C. Meyer, C. O. Girit, M. F. Crommie, A. Zettl, Hydrocarbon lithography on graphene membranes, Applied Physics Letters 92 (12) (2008) 123110. doi:10.1063/1.2901147.

[93] C. E. Mortimer, U. Müller, Chemie: das Basiswissen der Chemie ; 520 Formelbilder, 125 Tabellen, 8th Edition, Thieme, Stuttgart, 2003.

[94] K. Schubert, Ein Modell für die Kristallstrukturen der chemischen Elemente, Acta Crystallographica Section B Structural Crystallography and Crystal Chemistry 30 (1) (1974) 193–204. doi:10.1107/S0567740874002469.

[95] David A. Young, Phase Diagrams of the Elements, University of California Press, Berkeley, 1991.

[96] P. M. Horn, R. J. Birgeneau, P. Heiney, E. M. Hammonds, Melting of Submonolayer Krypton Films on Graphite, Physical Review Letters 41 (14) (1978) 961–964. doi:10.1103/PhysRevLett.41.961.

[97] R. Gangwar, R. M. Suter, Thermodynamics and phase diagram of multilayer krypton on graphite, Physical Review B 42 (4) (1990) 2711–2714. doi:10.1103/PhysRevB.42.2711.

[98] E. D. Specht, M. Sutton, R. J. Birgeneau, D. E. Moncton, P. M. Horn, Phase diagram and phase transitions of krypton on graphite in the one-to-two-layer regime, Physical Review B 30 (3) (1984) 1589–1592. doi:10.1103/PhysRevB.30.1589.

[99] E. D. Specht, A. Mak, C. Peters, M. Sutton, R. J. Birgeneau, K. L. D'Amico, D. E. Moncton, S. E. Nagler, P. M. Horn, Phase diagram and phase transitions of Krypton on graphite in the extended monolayer regime, Zeitschrift für Physik B Condensed Matter 69 (2) (1987) 347–377. doi:10.1007/BF01307294.

[100] D. M. Butler, J. A. Litzinger, G. A. Stewart, Completion of the Phase Diagram for the Monolayer Regime of the Krypton-Graphite Adsorption System, Physical Review Letters 44 (7) (1980) 466–468. doi:10.1103/PhysRevLett.44.466.

[101] D. M. Butler, J. A. Litzinger, G. A. Stewart, R. B. Griffiths, Heat Capacity of Krypton Physisorbed on Graphite, Physical Review Letters 42 (19) (1979) 1289–1292. doi:10.1103/PhysRevLett.42.1289.

[102] P. Day, M. LaMadrid, M. Lysek, D. Goodstein, Multilayer krypton phase diagram, Physical Review B 47 (12) (1993) 7501–7507. doi:10.1103/PhysRevB.47.7501.

[103] P. Cohen, J. Unguris, M. Webb, Xe monolayer adsorption on Ag(111) I. Structural properties, Surface Science 58 (2) (1976) 429–456. doi:10.1016/0039-6028(76)90480-5.

[104] C. Bäuerle, N. Mori, G. Kurata, H. Fukuyama, Studies of 2D Cryocrystals by STM Techniques, Journal of Low Temperature Physics 113 (5/6) (1998) 927–932. doi:10.1023/A:1022523510598.

[105] C. Herbig, E. H. Åhlgren, U. A. Schröder, A. J. Martínez-Galera, M. A. Arman, J. Kotakoski, J. Knudsen, A. V. Krasheninnikov, T. Michely, Xe irradiation of graphene on Ir(111): From trapping to blistering, Physical Review B 92 (8) (2015) 085429. doi:10.1103/PhysRevB.92.085429.

[106] C. Herbig, E. H. Åhlgren, T. Michely, Blister-free ion beam patterning of supported graphene, Nanotechnology 28 (5) (2017) 055304. doi:10.1088/1361-6528/aa527c.

[107] H. Cun, M. Iannuzzi, A. Hemmi, S. Roth, J. Osterwalder, T. Greber, Immobilizing Individual Atoms beneath a Corrugated Single Layer of Boron Nitride, Nano Letters 13 (5) (2013) 2098–2103. doi:10.1021/nl400449y.

[108] S. Yoo, E. H. Åhlgren, J. Seo, W. Kim, S. Chiang, J.-S. Kim, Growth kinetics of Kr nano structures encapsulated by graphene, Nanotechnology 29 (38) (2018) 385601. doi:10.1088/1361-6528/aad019.

[109] R. Villarreal, P.-C. Lin, F. Faraji, N. Hassani, H. Bana, Z. Zarkua, M. N. Nair, H.-C. Tsai, M. Auge, F. Junge, H. C. Hofsaess, S. De Gendt, S. De Feyter, S. Brems, E. H. Åhlgren, E. C. Neyts, L. Covaci, F. M. Peeters, M. Neek-Amal, L. M. C. Pereira, Breakdown of Universal Scaling for Nanometer-Sized Bubbles in Graphene, Nano Letters (2021) acs.nanolett.1c02470doi:10.1021/acs.nanolett.1c02470.

[110] E. Khestanova, F. Guinea, L. Fumagalli, A. K. Geim, I. V. Grigorieva, Universal shape and pressure inside bubbles appearing in van der Waals heterostructures, Nature Communications 7 (1) (2016) 12587. doi:10.1038/ncomms12587.

[111] Z. Li, Y. Wang, A. Kozbial, G. Shenoy, F. Zhou, R. McGinley, P. Ireland, B. Morganstein, A. Kunkel, S. P. Surwade, L. Li, H. Liu, Effect of airborne contaminants on the wettability of supported graphene and graphite, Nature Materials 12 (10) (2013) 925–931. doi:10.1038/nmat3709.

[112] W. Xie, L.-T. Weng, K. M. Ng, C. K. Chan, C.-M. Chan, Clean graphene surface through high temperature annealing, Carbon 94 (2015) 740–748. doi:10.1016/j.carbon.2015.07.046.

[113] A. Pálinkás, G. Kálvin, P. Vancsó, K. Kandrai, M. Szendrő, G. Németh, M. Németh, A. Pekker, J. S. Pap, P. Petrik, K. Kamarás, L. Tapasztó, P. Nemes-Incze, The composition and structure of the ubiquitous hydrocarbon contamination on van der Waals materials, Nature Communications 13 (1) (2022) 6770. doi:10.1038/s41467-022-34641-7.

[114] W. Zhou, M. D. Kapetanakis, M. P. Prange, S. T. Pantelides, S. J. Pennycook, J.-C. Idrobo, Direct Determination of the Chemical Bonding of Individual Impurities in Graphene, Physical Review Letters 109 (20) (2012) 206803. doi:10.1103/PhysRevLett.109.206803.

[115] T. Susi, J. Kotakoski, D. Kepaptsoglou, C. Mangler, T. C. Lovejoy, O. L. Krivanek, R. Zan, U. Bangert, P. Ayala, J. C. Meyer, Q. Ramasse, Silicon–Carbon Bond Inversions Driven by 60-keV Electrons in Graphene, Physical Review Letters 113 (11) (2014) 115501. doi:10.1103/PhysRevLett.113.115501.

[116] H. Inani, K. Mustonen, A. Markevich, E.-X. Ding, M. Tripathi, A. Hussain, C. Mangler, E. I. Kauppinen, T. Susi, J. Kotakoski, Silicon Substitution in Nanotubes and Graphene via Intermittent Vacancies, The Journal of Physical Chemistry C (2019) acs.jpcc.9b01894doi:10.1021/acs.jpcc.9b01894.

[117] G. Zagler, M. Reticcioli, C. Mangler, D. Scheinecker, C. Franchini, J. Kotakoski, CuAu, a hexagonal two-dimensional metal, 2D Materials 7 (4) (2020) 045017. doi:10.1088/2053-1583/ab9c39.

[118] B. Rik (Ed.), Aberration-Corrected Analytical Transmission Electron Microscopy, 1st Edition, John Wiley & Sons, Ltd, 2011. doi:10.1002/9781119978848.

[119] B. Fickl, Atomic resolution in-situ oxidation and evaporation study of molybdenum ditelluride utilizing environmental STEM, Master's thesis, Wien (2020).

[120] O. Scherzer, Über einige Fehler von Elektronenlinsen, Zeitschrift für Physik 101 (9-10) (1936) 593–603. doi:10.1007/BF01349606.

[121] O. Scherzer, Spharische und chromatische korrektur von elktronen-linsen, Optik 2 (1947) 114–132.

[122] O. L. Krivanek, N. Dellby, A. J. Spence, R. A. Camps, L. M. Brown, Aberration correction in the STEM, Inst. Phys. Conf. Ser. 153 (Proceedings 1997 EMAG meeting) Ed. Rodenburg JM 35 (1997).

[123] O. Krivanek, N. Dellby, A. Lupini, Towards sub-Å electron beams, Ultramicroscopy 78 (1-4) (1999) 1–11. doi:10.1016/S0304-3991(99)00013-3.

[124] P. E. Batson, N. Dellby, O. L. Krivanek, Sub-ångstrom resolution using aberration corrected electron optics, Nature 418 (6898) (2002) 617–620. doi:10.1038/nature00972.

[125] https://www.nion.com/resources.html, accessed on 2024-01-10.

[126] N. Dellby, O. L. Krivanek, P. D. Nellist, P. E. Batson, A. R. Lupini, Progress in aberration-corrected scanning transmission electron microscopy, Microscopy 50 (3) (2001) 177–185. doi:10.1093/jmicro/50.3.177.

[127] A. V. Crewe, J. Wall, J. Langmore, Visibility of Single Atoms, Science 168 (3937) (1970) 1338–1340. doi:10.1126/science.168.3937.1338.

[128] A. V. Crewe, The physics of the high-resolution scanning microscope, Reports on Progress in Physics 43 (5) (1980) 621–639. doi:10.1088/0034-4885/43/5/002.

[129] S. Pennycook, D. Jesson, High-resolution Z-contrast imaging of crystals, Ultramicroscopy 37 (1-4) (1991) 14–38. doi:10.1016/0304-3991(91)90004-P.

[130] O. L. Krivanek, M. F. Chisholm, V. Nicolosi, T. J. Pennycook, G. J. Corbin, N. Dellby, M. F. Murfitt, C. S. Own, Z. S. Szilagyi, M. P. Oxley, S. T. Pantelides, S. J. Pennycook, Atom-by-atom structural and chemical analysis by annular dark-field electron microscopy., Nature 464 (7288) (2010) 571–574. doi:10.1038/nature08879.

[131] https://eels.info/, accessed on 2024-01-10.

[132] R. F. Egerton, Electron energy-loss spectroscopy in the TEM, Reports on Progress in Physics 72 (1) (2009) 016502. doi:10.1088/0034-4885/72/1/016502.

[133] C. Speckmann, J. Lang, J. Madsen, M. R. A. Monazam, G. Zagler, G. T. Leuthner, N. McEvoy, C. Mangler, T. Susi, J. Kotakoski, Combined electronic excitation and knock-on damage in monolayer MoS 2, Physical Review B 107 (9) (2023) 094112. doi:10.1103/PhysRevB.107.094112.

[134] M. Hotz, G. Corbin, N. Dellby, O. Krivanek, C. Mangier, J. Meyer, Ultra-High Vacuum Aberration-Corrected STEM for in-situ studies, Microscopy and Microanalysis 22 (S3) (2016) 34–35. doi:10.1017/S1431927616001021.

[135] J. Kotakoski, C. Mangler, J. C. Meyer, Imaging atomic-level random walk of a point defect in graphene, Nature Communications 5 (1) (2014) 3991. doi:10.1038/ncomms4991.

[136] O. L. Krivanek, G. J. Corbin, N. Dellby, B. F. Elston, R. J. Keyse, M. F. Murfitt, C. S. Own, Z. S. Szilagyi, J. W. Woodruff, An electron microscope for the aberration-corrected era, Ultramicroscopy 108 (3) (2008) 179–195. doi:10.1016/j.ultramic.2007.07.010.

[137] J. Madsen, fourier-scale-calibration, https://github.com/jacobjma/fourier-scale-calibration, accessed on : 2021-02-03 (Feb. 2022).

[138] S. van der Walt, J. L. Schönberger, J. Nunez-Iglesias, F. Boulogne, J. D. Warner, N. Yager, E. Gouillart, T. Yu, scikit-image: image processing in Python, PeerJ 2 (2014) e453. doi:10.7717/peerj.453.

[139] K. R. Paserba, A. J. Gellman, Kinetics and Energetics of Oligomer Desorption from Surfaces, Physical Review Letters 86 (19) (2001) 4338–4341. doi:10.1103/PhysRevLett.86.4338.

[140] Y.-C. Lin, C.-C. Lu, C.-H. Yeh, C. Jin, K. Suenaga, P.-W. Chiu, Graphene Annealing: How Clean Can It Be?, Nano Letters 12 (1) (2012) 414–419. doi:10.1021/nl203733r.

[141] G. Algara-Siller, O. Lehtinen, A. Turchanin, U. Kaiser, Dry-cleaning of graphene, Applied Physics Letters 104 (15) (2014) 153115. doi:10.1063/1.4871997.

[142] A. M. Goossens, V. E. Calado, A. Barreiro, K. Watanabe, T. Taniguchi, L. M. K. Vandersypen, Mechanical cleaning of graphene, Applied Physics Letters 100 (7) (2012) 073110. doi:10.1063/1.3685504.

[143] P. Schweizer, C. Dolle, D. Dasler, G. Abellán, F. Hauke, A. Hirsch, E. Spiecker, Mechanical cleaning of graphene using in situ electron microscopy, Nature Communications 11 (1) (2020) 1743. doi:10.1038/s41467-020-15255-3.

[144] M. Tripathi, A. Mittelberger, K. Mustonen, C. Mangler, J. Kotakoski, J. C. Meyer, T. Susi, Cleaning graphene: Comparing heat treatments in air and in vacuum, Physica Status Solidi (RRL) – Rapid Research Letters 11 (8) (2017) 1700124. doi:10.1002/pssr.201700124.

[145] E. Balanzat, S. Bouffard, Basic Phenomena of the Particle-Matter Interaction, Solid State Phenomena 30-31 (1992) 7–74, publisher: Trans Tech Publications Ltd. doi:10.4028/www.scientific.net/SSP.30-31.7.

[146] M. Robinson, I. Torrens, Computer simulation of atomic-displacement cascades in solids in the binary-collision approximation, Physical Review B 9 (12) (1974) 5008–5024. doi:10.1103/PhysRevB.9.5008.

[147] E. H. Åhlgren, J. Kotakoski, A. V. Krasheninnikov, Atomistic simulations of the implantation of low-energy boron and nitrogen ions into graphene, Physical Review B 83 (11) (2011) 115424. doi:10.1103/PhysRevB.83.115424.

[148] U. Bangert, W. Pierce, D. M. Kepaptsoglou, Q. Ramasse, R. Zan, M. H. Gass, J. A. Van den Berg, C. B. Boothroyd, J. Amani, H. Hofsäss, Ion Implantation of Graphene—Toward IC Compatible Technologies, Nano Letters 13 (10) (2013) 4902–4907. doi:10.1021/nl402812y.

[149] T. Susi, T. P. Hardcastle, H. Hofsäss, A. Mittelberger, T. J. Pennycook, C. Mangler, R. Drummond-Brydson, A. J. Scott, J. C. Meyer, J. Kotakoski, Single-atom spectroscopy of phosphorus dopants implanted into graphene, 2D Materials 4 (2) (2017) 021013. doi:10.1088/2053-1583/aa5e78.

[150] M. Tripathi, A. Markevich, R. Böttger, S. Facsko, E. Besley, J. Kotakoski, T. Susi, Implanting Germanium into Graphene, ACS Nano 12 (5) (2018) 4641–4647. doi:10.1021/acsnano.8b01191.

[151] P.-C. Lin, R. Villarreal, S. Achilli, H. Bana, M. N. Nair, A. Tejeda, K. Verguts, S. De Gendt, M. Auge, H. Hofsäss, S. De Feyter, G. Di Santo, L. Petaccia, S. Brems, G. Fratesi, L. M. C. Pereira, Doping Graphene with Substitutional Mn, ACS Nano 15 (3) (2021) 5449–5458. doi:10.1021/acsnano.1c00139.

[152] D. Marton, K. J. Boyd, T. Lytle, J. W. Rabalais, Near-threshold ion-induced defect production in graphite, Physical Review B 48 (10) (1993) 6757–6766. doi:10.1103/PhysRevB.48.6757.

[153] H. Conrads, M. Schmidt, Plasma generation and plasma sources, Plasma Sources Science and Technology 9 (4) (2000) 441–454. doi:10.1088/0963-0252/9/4/301.

[154] B. H. Wolf, C. R. Company (Eds.), Handbook of ion sources, CRC Press, Boca Raton, 1995.

[155] Y. Notay, Flexible Conjugate Gradients, SIAM Journal on Scientific Computing 22 (4) (2000) 1444–1460. doi:10.1137/S1064827599362314.

[156] G. Rutkai, M. Thol, R. Span, J. Vrabec, How well does the Lennard-Jones potential represent the thermodynamic properties of noble gases?, Molecular Physics 115 (9-12) (2017) 1104–1121. doi:10.1080/00268976.2016.1246760.

[157] H. A. Lorentz, Ueber die Anwendung des Satzes vom Virial in der kinetischen Theorie der Gase, Annalen der Physik 248 (1) (1881) 127–136. doi:10.1002/andp.18812480110.

[158] D. Berthelot, Sur le mélange des gaz, Comptes rendus hebdomadaires des séances de l'Académie des Sciences 126 (1898) 1703–1855.

[159] S. J. Stuart, A. B. Tutein, J. A. Harrison, A reactive potential for hydrocarbons with intermolecular interactions, The Journal of Chemical Physics 112 (14) (2000) 6472–6486. doi:10.1063/1.481208.

[160] G. Zagler, C. Mangler, J. Kotakoski, Patterned Ultra-Thin Gold Nanostructures on Graphene, Microscopy and Microanalysis 25 (S2) (2019) 1530–1531. doi:10.1017/S1431927619008389.

[161] Q. M. Ramasse, C. R. Seabourne, D.-M. Kepaptsoglou, R. Zan, U. Bangert, A. J. Scott, Probing the Bonding and Electronic Structure of Single Atom Dopants in Graphene with Electron Energy Loss Spectroscopy, Nano Letters 13 (10) (2013) 4989–4995. doi:10.1021/nl304187e.

[162] M. Ziatdinov, O. Dyck, A. Maksov, X. Li, X. Sang, K. Xiao, R. R. Unocic, R. Vasudevan, S. Jesse, S. V. Kalinin, Deep Learning of Atomically Resolved Scanning Transmission Electron Microscopy Images: Chemical Identification and Tracking Local Transformations, ACS Nano 11 (12) (2017) 12742–12752. doi:10.1021/acsnano.7b07504.

[163] J. C. Meyer, A. Chuvilin, G. Algara-Siller, J. Biskupek, U. Kaiser, Selective sputtering and atomic resolution imaging of atomically thin boron nitride membranes., Nano Lett. 9 (7) (2009) 2683–2689. doi:10.1021/nl9011497.

[164] C. Jin, F. Lin, K. Suenaga, S. Iijima, Fabrication of a Freestanding Boron Nitride Single Layer and Its Defect Assignments, Phys. Rev. Lett. 102 (19) (2009) 195505. doi:10.1103/PhysRevLett.102.195505.

[165] A. Postl, P. P. P. Hilgert, A. Markevich, J. Madsen, K. Mustonen, J. Kotakoski, T. Susi, Indirect measurement of the carbon adatom migration barrier on graphene, Carbon 196 (2022) 596–601. doi:10.1016/j.carbon.2022.05.039.

[166] A. A. Shiryaev, A. L. Trigub, E. N. Voronina, K. O. Kvashnina, V. L. Bukhovets, Behavior of implanted Xe, Kr and Ar in nanodiamonds and thin graphene stacks: experiment and modeling, Physical Chemistry Chemical Physics 23 (38) (2021) 21729–21737. doi:10.1039/D1CP02600C.

[167] O. Lehtinen, J. Kotakoski, A. V. Krasheninnikov, A. Tolvanen, K. Nordlund, J. Keinonen, Effects of ion bombardment on a two-dimensional target: Atomistic simulations of graphene irradiation, Physical Review B 81 (15) (2010) 153401. doi:10.1103/PhysRevB.81.153401.

[168] J. Kotakoski, F. R. Eder, J. C. Meyer, Atomic structure and energetics of large vacancies in graphene, Physical Review B 89 (20) (2014) 201406. doi:10.1103/PhysRevB.89.201406.

[169] M. T. Lusk, L. D. Carr, Nanoengineering Defect Structures on Graphene, Physical Review Letters 100 (17) (2008) 175503. doi:10.1103/PhysRevLett.100.175503.

[170] J. Kotakoski, J. C. Meyer, S. Kurasch, D. Santos-Cottin, U. Kaiser, A. V. Krasheninnikov, Stone-Wales-type transformations in carbon nanostructures driven by electron irradiation, Physical Review B 83 (24) (2011) 245420. doi:10.1103/PhysRevB.83.245420.

[171] O. Cretu, A. V. Krasheninnikov, J. A. Rodríguez-Manzo, L. Sun, R. M. Nieminen, F. Banhart, Migration and Localization of Metal Atoms on Strained Graphene, Physical Review Letters 105 (19) (2010) 196102. doi:10.1103/PhysRevLett.105.196102.